MULTISCALE MODELS OF INTERFACIAL MECHANICS IN LOW

DIMENSIONAL SYSTEMS

Christopher C. Price

A DISSERTATION

in

Materials Science and Engineering

Presented to the Faculties of the University of Pennsylvania

in

Partial Fulfillment of the Requirements for the

Degree of Doctor of Philosophy

2022

Supervisor of Dissertation

Vivek B. Shenoy
Eduardo D. Glandt President's Distinguished Professor, Materials Science and Engineering, University of Pennsylvania

Graduate Group Chairperson

I-Wei Chen
Skirkanich Professor of Materials Innovation, Materials Science and Engineering, University of Pennsylvania

Dissertation Committee
Eric Detsi
Assistant Professor, Materials Science and Engineering, University of Pennsylvania

Yury Gogotsi
Distinguished University and Charles T. and Ruth M. Bach Professor, Materials Science and Engineering, Drexel University

Liang Feng
Associate Professor, Materials Science and Engineering, University of Pennsylvania

MULTISCALE MODELS OF INTERFACIAL MECHANICS IN LOW DIMENSIONAL

SYSTEMS

COPYRIGHT

2022

Christopher Carr Price

To my parents and Caitlin

Acknowledgements

"What I want to talk about is the problem of manipulating and controlling things on a small scale … It is a staggeringly small world that is below."

Richard Feynman

"People think focus means saying yes to the thing you've got to focus on. But that's not what it means at all. It means saying no to the hundred other good ideas that there are. You have to pick carefully. I'm actually as proud of the things we haven't done as the things I have done. Innovation is saying no to 1,000 things."

Steve Jobs

Completing my PhD would not have been possible without the mentorship, support, and encouragement from the amazing people in my life. I am extremely grateful for the training and mentorship imparted by my advisor, Prof. Vivek Shenoy, who has shaped my development as a scientist with an unwavering focus on isolating the fundamental physics in any problem. I owe my uniquely wide-ranging PhD experience to his expertise and interests across math, physics, materials science, chemistry, and biology. I also want to especially thank my thesis committee members: Prof. Yury Gogotsi, Prof. Eric Detsi, and Prof. Liang Feng. They have been generous with their time and feedback during critical points of my PhD and my work has benefitted from their physics and materials science expertise.

Modern science is more collaborative than ever, and I have appreciated the opportunity to work with many great additional collaborators throughout my PhD: Han Ye,

opportunity I could ask for, and for teaching me to always pursue my best self. To Caitlin – your everlasting support means the world and I can't wait for the next chapter of our life together.

ABSTRACT

MULTISCALE MODELS OF INTERFACIAL MECHANICS IN LOW

DIMENSIONAL SYSTEMS

Christopher C. Price

Vivek B. Shenoy

Crucial thrusts in modern technology from electronic information processing to engineering cellular systems require manipulation and control of materials on smaller and smaller scales to succeed. A simple and successful way to break conventional material property limitations or design multifunctional devices is to interface two different materials together. At small length scales, the surface to bulk ratio of each component material increases, to the point that the interfacial physics can dominate the properties of the engineered system. Simultaneously, the combinatorial space of possible interfaces between materials and/or molecules is far too vast to explore by trial-and-error experimentation alone. Intuitive theoretical models can greatly improve our ability to navigate such large search spaces by providing insight on how two materials are likely to interact. The goal of this thesis is to develop predictive physical models which explain emergent phenomena at material interfaces across multiple length and time scales. A variety of state-of-the-art tools were applied to realize this goal, including analytical mathematics, quantum mechanical simulations, finite element methods, and deep neural networks. At the electron scale, a

continuum model parametrized by first-principles simulations was employed to develop design criteria for confined quantum states in lateral heterostructures of two-dimensional materials. At the atomic scale, a chemo-mechanical model incorporating long-range electrostatics was developed to explain synthesizability trends in composite heterostructures of inorganic perovskites and organic molecules. A machine learning graph neural network model was developed and applied to predict the impact of general surface strains on the adsorption energy of small molecule intermediates on catalyst surfaces. Finally, at the microscale, a nonlinear kinetic model was developed to explain how cells acquire and retain memory of the mechanical properties of their surroundings across multiple timescales, which can lead to irreversible adaptation and differentiation. The methods and results presented in this thesis can improve our understanding of physical phenomena arising at interfaces and provide a blueprint for future applications of multiscale computational modeling to science and engineering problems.

TABLE OF CONTENTS

xiii

List of Tables

List of Illustrations

PREFACE

Chapters 2, 3, and 5 of this thesis have appeared in the publications below; all figures, tables, and illustrations in these chapters have been reproduced or adapted from these publications with permission.

1. **Price, C. C.***, Frey, N.*, Jariwala, D. & Shenoy, V. Engineering Zero-Dimensional Quantum Confinement in Transition-Metal Dichalcogenide Heterostructures. ACS Nano 13, 8303–8311 (2019).

2. **Price, C. C.**, Blancon, J.-C., Mohite, A. & Shenoy, V. Interfacial Electromechanics Predicts Phase Behavior of 2D Hybrid Halide Perovskites. ACS Nano 14, 3353–3364.

3. **Price, C. C.***, Mathur, J.*, Boerckel, J. D., Pathak, A. & Shenoy, V. B. Dynamic Self-Reinforcement of Gene Expression Determines Acquisition of Cellular Mechanical Memory. Biophysical Journal 0, (2021).

* Denotes equal contribution.

The following publications that I co-authored during my Ph.D. are *not* presented in this thesis:

1. Gong, Z.; Wisdom, K. M.; McEvoy, E.; Chang, J.; Adebowale, K.; **Price, C. C.**; Chaudhuri, O.; Shenoy, V. B. Recursive Feedback between Matrix Dissipation and

Chemo-Mechanical Signaling Drives Oscillatory Growth of Cancer Cell Invadopodia. Cell reports 2021, 35 (4), 109047. https://doi.org/10.1016/j.celrep.2021.109047.

2. Kumar, P.; Horwath, J. P.; Foucher, A. C.; **Price, C. C.**; Acero, N.; Shenoy, V. B.; Stach, E. A.; Jariwala, D. Direct Visualization of Out-of-Equilibrium Structural Transformations in Atomically Thin Chalcogenides. npj 2D Materials and Applications 2020, 4 (1), 1–10. https://doi.org/10.1038/s41699-020-0150-2.

3. Guo, Z.; **Price, C. C.**; Shenoy, V. B.; Lowengrub, J. Modeling the Vertical Growth of van Der Waals Stacked 2D Materials Using the Diffuse Domain Method. Modelling and Simulation in Materials Science and Engineering 2020, 28 (2), 025002. https://doi.org/10.1088/1361-651X/ab5e9a.

4. Ye, H.; Zhou, J.; Er, D.; **Price, C. C.**; Yu, Z.; Liu, Y.; Lowengrub, J.; Lou, J.; Liu, Z.; Shenoy, V. B. Toward a Mechanistic Understanding of Vertical Growth of van Der Waals Stacked 2D Materials: A Multiscale Model and Experiments. ACS Nano 2017, 11 (12), 12780–12788. https://doi.org/10.1021/acsnano.7b07604.

5. Mandyam, S.; Zhao, M.-Q.; Masih Das, P.; Zhang, Q.; **Price, C. C.**; Gao, Z.; Shenoy, V.; Drndić, M.; Johnson, A. T. C. Controlled Growth of Large-Area Bilayer Tungsten Diselenides with Lateral P–N Junctions. ACS Nano 2019, 13 (9), 10490–10498. https://doi.org/10.1021/acsnano.9b04453.

6. Frey, N. C.; **Price, C. C.**; Bandyopadhyay, A.; Kumar, H.; Shenoy, V. B. Predicted Magnetic Properties of MXenes. In *2D Metal Carbides and Nitrides (MXenes)*; Springer International Publishing: Cham, 2019; pp 291–300. https://doi.org/10.1007/978-3-030-19026-2_15.

7. Johnson, L. R.; Sridhar, S.; Zhang, L.; Fredrickson, K. D.; Raman, A. S.; Jang, J.; Leach, C.; Padmanabhan, A.; **Price, C. C.**; Frey, N. C.; Raizada, A.; Rajaraman, V.; Saiprasad, S. A.; Tang, X.; Vojvodic, A. MXene Materials for the Electrochemical Nitrogen Reduction-Functionalized or Not? *ACS Catalysis* **2020**, *10* (1), 253–264. https://doi.org/10.1021/acscatal.9b01925.

Chapter 1 Introduction

1.1 Demand for Material Heterostructures
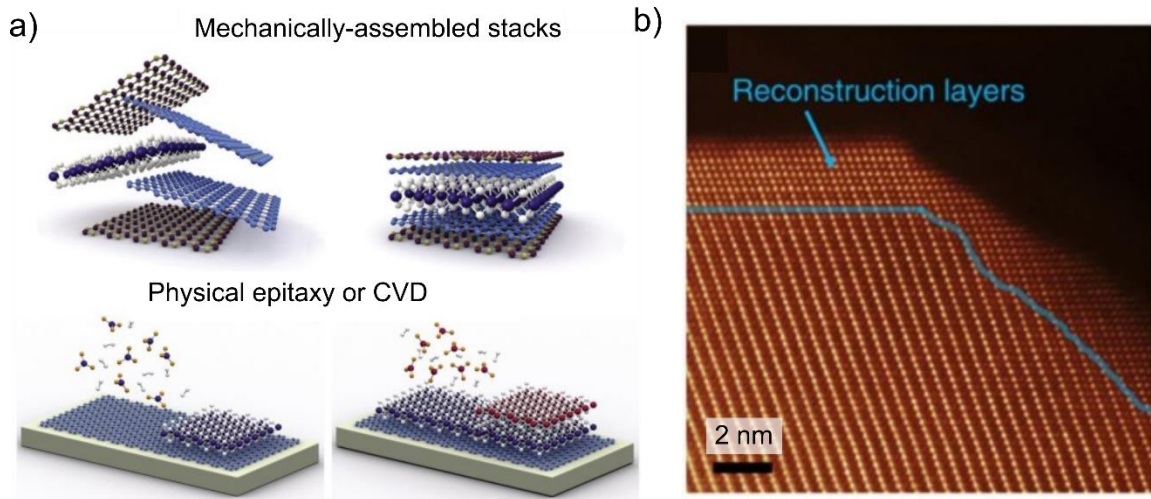
Figure 1.1 a) Examples of nanomaterial heterostructure assembly, through post-synthetic stacking (top) or targeted materials synthesis routes (bottom). Reproduced from [3]. **b)** Alterations in atomic structure due to the presence of a surface; the reconstruction depends on the angle of the surface and penetrates several atomic layers into the material. Reproduced from [294].

Major advances in technology are always underpinned by improvements in capabilities to engineer matter, from iron and bronze to steel, silicon, and the increasingly complex array of today's electronic materials. Addressing environmental, healthcare, and infrastructure challenges in the 21st century necessitates continued innovation of material platforms with outstanding physical properties. Material heterostructures created by bringing two different materials together can give rise to new functionalities from the interface, or simply combine existing functionality into smaller areas which are less

resource-intensive to produce. The combinatoric possibilities of single materials design are enormous and this only grows when considering multiple materials together (**Figure 1.1a**). Efficient tools to evaluate and predict heterostructure properties *a priori* are critical to navigating this design space. Expanding knowledge of materials heterostructures and their interactions has substantial potential impact in applications such as (but not limited to) energy storage [1], catalysis [2], optoelectronics [3], and cell culture. [4,5]

1.2 Interfaces in Low Dimensions

Heterostructures derive most of their unique properties due to changes in the chemical bonding at surfaces or interfaces (**Figure 1.1b**). This makes heterostructuring an especially powerful tool for materials engineering at nano- and micro- length scales, where the surface and interface to volume ratio is inherently large. The abrupt changes in atomic bonding at material surfaces and interfaces can change the atomic structure and lead to unpredictable properties. Broken crystal symmetry creates imbalances in charges and mechanical forces, leading to accumulated stresses and polarizations that differ from interior bulk properties (**Figure 1.2a**). Changes in electronic properties between the two materials amplify these effects and can lead to charge transfer between the two materials. Defects will migrate towards surfaces and interfaces to relax interior bulk stresses. These atomic scale effects cause changes at larger length scales by introducing new degrees of freedom and accumulation of the local strain and electric fields (**Figure 1.2b**). [6,7] Finally, interfaces are active sites for interconverting forms of potential energy; for
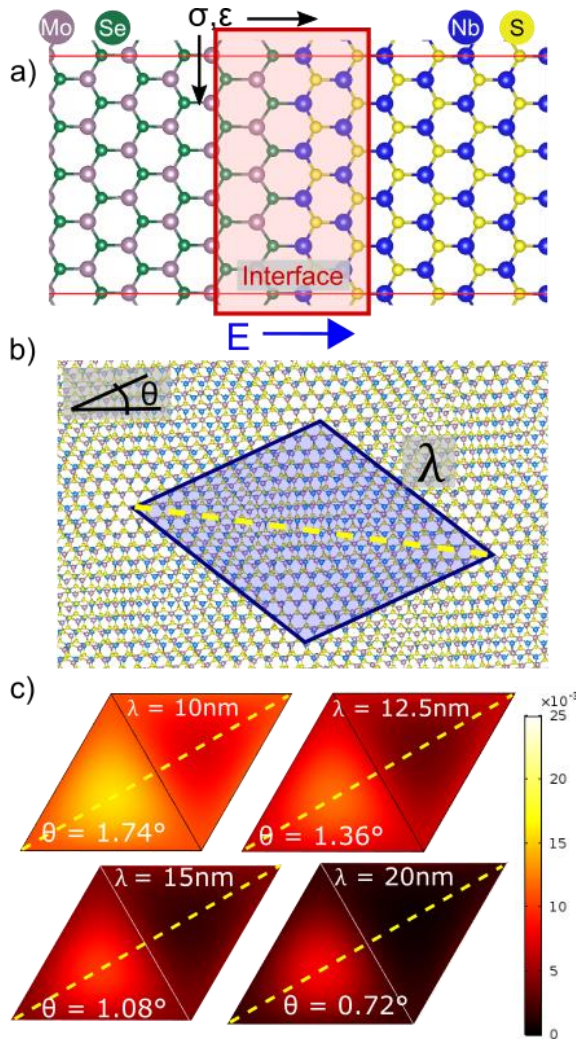
Figure 1.2 a) Interfaces between materials with similar atomic arrangements but different compositions cause symmetry breaking on the atomic scale, inducing stress σ, strain ε, and electric fields E. **b)** Over longer length scales, interfaces can create new degrees of freedom and increase the length scale of symmetry, such as in this Moiré pattern with superlattice parameter λ formed from stacking the materials in **a)** with angle θ. **c)** Effect on localization of quantum states caused by the long-range potential from different stacking angles in **b)**. Color scale is probability density of the bound state wave function.

example, converting mechanical stress into localization of a quantum state (**Figure 1.2c**). This can allow manipulation of interior nanoscale physics using external parameters which are much simpler to control at the macroscale. Due to the dominance of interfacial properties on the nanoscale, successful nanomaterials engineering relies on understanding the structure-property relationships across many different interfacial configurations.

1.3 Multiscale Modeling and Overview of Computational Methods

Physical intuition and materials optimization has long been developed through empirical observation and experimental trial-and-error. Advances in condensed matter physics over the last few centuries and rapidly increasing computational capabilities over the last few decades have enabled fundamental understanding of materials structure-property relationships through simulation, which can be conducted more quickly and cheaply than experiments. However, individual theoretical or simulation frameworks are limited by approximations and assumptions which are necessary to maintain computability in the scope of the target problem. This makes it difficult to accomplish deterministic materials design requiring concurrent control of different physical phenomena from simulations alone. [8] Multiscale modeling aims to improve realistic predictions of materials systems by combining multiple theoretical approaches together, identifying the necessary atomic scale information which can lead to emergent, collective changes at micro- or macroscopic scales. [9] This modeling strategy is particularly apt for studies of materials interfaces because interfacial properties depend on both the individual characteristics of the component materials and their specific interactions. [10] Examples of physical phenomena examined in this thesis that transit multiple length or time scales include geometric effects on electrons and holes, strain fields, electric fields, and positive reinforcement mechanisms. Here we will give a high-level overview of the different computational techniques used in this thesis; additional details on combining these

simulation frameworks into multiscale models are given in the Methods section of each chapter.

1.3.1 Density Functional Theory

Density functional theory (DFT) is the primary method we use to model the ground-state configuration of electrons in a crystalline material in a vacuum. The mathematical foundations of the theory are covered extensively in the literature, and modern implementations are based on several decades of method development. [11–18] The core goal of DFT is to approximate a solution to the many-body time independent Schrodinger equation by solving the non-interacting Schrodinger equation in an effective potential specified by the total electron density. In an iterative process, this can be combined with the Born-Oppenheimer approximation and gradient descent algorithms to simultaneously find the minimum energy configuration for both the electron density and the ionic positions. [19] From a multiscale modeling perspective, DFT is extremely useful to generate accurate, *ab initio* atomic scale structures and electronic properties which can be input to other methods, but it is also severely limited in the systems it can be applied to. Depending on the desired accuracy, DFT implementations can generally consider structures with hundreds to thousands of atoms, corresponding to 10-100 Angstroms in unit cell dimensions. They rely heavily on taking advantage of structural symmetries for efficiency, and therefore low symmetry structures such as surfaces or interfaces are additionally computationally demanding. We primarily use the Vienna *ab initio* simulation

package (VASP) implementation of DFT [20,21] to calculate fundamental electronic properties, electron distributions, formation energies, and the responses of these quantities to structural perturbations. We also use the atomic simulation environment and pymatgen open-source packages to help manage high-throughput calculations of many atomistic structures. [22,23]

1.3.2 Supervised Machine Learning

Supervised machine learning encompasses a set of methods which attempt to approximate a function that maps the relationship between input data and a pre-determined label or value for each datapoint. Applied to materials property prediction, the input data is typically structural and compositional data and the output is a target property that is expensive to calculate or measure experimentally. [24] The labels 'supervise' the training process, which proceeds by gradient descent of the model weights through a fitness landscape constructed by calculation of the error between the model predictions and the ground truth labels. Successfully trained models can be used to make predictions on denser samplings of the training space, which is especially important for materials and molecular systems with many degrees of freedom that are difficult to explore using direct simulation alone. The success of model training and performance depends on many factors including dataset size, dataset representation, model selection and architecture, training procedure, and task definition, and ideal strategies for each are chosen using common heuristics or empirical trial and error. [25] In this thesis, we use machine learning models as a

component of the multiscale modeling toolbox, combining them with high throughput DFT-generated datasets to evaluate structures at scales that would be computationally intractable using atomistic simulations alone. We focus on graph neural networks, which are designed to operate directly on atomic structures [26]; graph representations of atomistic materials structures are generated using the NetworkX package [27] and implement our model training in PyTorch. [28]

1.3.3 Finite Element Analysis and Continuum Models

The last primary computational technique in our multiscale methods toolbox is finite element analysis (FEA). This is a general numerical method for solving systems partial differential equations in several dimensions over complex geometries by subdividing the geometry into small local components that are solved under constraints. [29] The accuracy and usefulness of the results depends entirely on the system of equations and the parameterization, but they offer a unique way to study unique and perturbed geometries. We use FEA in this thesis to implement physically derived continuum models, which can be solved to an arbitrary degree of precision using denser numerical discretizations of the domain. By parametrizing the differential equations with data from DFT calculations, the accuracy of DFT is translated to a new length scale. FEA and continuum simulations are implemented using the COMSOL Multiphysics ® software package and open-source custom software written in Python.

1.4 Goals of this Thesis

This thesis' primary goal is to develop new models of physical phenomena occurring at the interface between two different materials or material phases. To achieve this, different theoretical frameworks are applied and considered together to cover multiple relevant length and time scales, with the aim of identifying the important physical information created at the interface that changes the expected material properties. Developing these multiscale physical models is necessary to bridge the gap between current computational representations and experimentally synthesized materials, since all materials are affected by their interfaces during synthesis, characterization, and device assembly. We aim to minimize model complexity while retaining the necessary interactions to make new predictions within the scope of the problem, and we verify these predictions with experimental data or first-principles calculations wherever possible. This thesis is divided into four major sections, arranged in order from smallest to largest physical scale for the interfaces involved.

1.4.1 Interfacing Finite-Size 2D Materials to Engineer Quantum Confinement of Charge Carriers

In Chapter 2, we present a continuum quantum mechanics framework to predict the emergence of localized quantum states in 2D materials. Achieving these states is desirable for optoelectronics and quantum information yet challenging due to the difficulties in confining Dirac fermions. These challenges arise due to the fundamental

differences in the electronic structure of 2D hexagonal materials as compared to conventional semiconductor quantum dots. Our integrated multiscale approach translates first-principles electronic structure to higher length scales, where we apply a continuum model to consider arbitrary 2D quantum dot geometries and sizes. Focusing on a common and synthesizable model system of a finite MoS_2 triangular region embedded in a WS_2 matrix (MoS_2/WS_2), we find discrete bound states for region sizes up to 20 nm. We propose figures of merit that can be used to engineer maximally isolated bound states at room temperature. These design principles apply to the entire family of semiconducting TMD materials, which has seen immense recent progress in control of experimental synthesis and characterization.

1.4.2 Interfacial Phenomena in Synthesis of Layered Materials

In **Chapter 3**, we develop a thermodynamic framework to generate the phase diagrams of quasi-2D hybrid halide perovskites ($A'_2A_{N-1}M_NX_{3N+1}$; A' = large organic molecule with cationic group, A = [Cs^+, $CH_3NH_3^+$, $HC(NH_2)_2^+$], M = [Pb, Sn, Ge], X = [I^-, Br^-, Cl^-]), which consist of large organic molecules interspersing an inorganic perovskite lattice and can form ordered, layered phases with desirable semiconducting properties. We incorporate the mechanics and electrostatics of the interface between the large organic cations and the metal halide octahedral network. We find that the apparent difficulty in synthesizing phase-pure samples with a stoichiometric index N > 5 can be attributed to the energetic competition between repulsion of opposing interfacial dipole layers and

9

mechanical relaxation induced by interfacial stress. Our model shows quantitative agreement with experimental observations of the maximum phase-pure stoichiometric index and explains the non-monotonic evolution of the lattice parameters with changing stoichiometry. This model is generalizable to the entire family of quasi-2D perovskites and can guide the design of new composite materials.

1.4.3 Predicting Surface Strain Effects on Adsorption Energy with Graph Neural Networks

In **Chapter 4**, we expand our study of the mechanics occurring at the interface between crystalline materials and molecules and develop a high-throughput DFT and machine learning framework to predict the impact of surface strain on adsorption energy. Surface strain can increase or decrease the adsorption energy depending on the surface composition, adsorbate composition, surface facet, and adsorbate site, breaking traditional scaling relationships which inhibit energy barrier alteration in conventional catalyst design. We aim to generate a model that maps the adsorption energy response to a given input strain for strained copper binary alloy catalyst + adsorbate complexes from the Open Catalyst Project. [16] After developing a custom first-principles dataset, we train a graph neural network that successfully predicts the class of the adsorption energy response for 85% of surface strains and outperforms simpler model baselines. Our model identifies Cu-S alloy catalysts as promising candidates for strain engineering since the majority of surface strain patterns raise the adsorption energy of the *NH intermediate, which is

10

important in ammonia synthesis. Our presented machine learning approach can be used to identify target strain patterns that can reduce energy barriers in heterogeneous catalysis.

1.4.4 Dynamics of Interfacial Mechanics Leads to Continuously Variable Cellular Memory

In **Chapter 5**, we shift to studying how the mechanical properties of an interface can dynamically affect gene expression in cells, giving rise to memory that the cell retains about the mechanics of the interface. This long-term mechanical memory occurs when cells cultured on stiff substrates for sufficient time (priming phase) maintain altered phenotype compared to unprimed control groups after switching back to soft substrates (dissipation phase). The timescale of memory acquisition and retention is orders of magnitude larger than the timescale of mechanosensitive cellular signaling, and memory retention time changes continuously with priming time. We develop a model that captures these features by accounting for positive reinforcement in mechanical signaling. The sensitivity of reinforcement represents the dynamic transcriptional state of the cell composed of protein lifetimes and 3D chromatin organization. Our model provides a single framework connecting microenvironment mechanical history to cellular outcomes ranging from no memory to terminal differentiation. Predicting cellular memory of environmental changes can help engineer cellular dynamics through changes in culture environments, which has important implications for designing and testing cell-based therapeutics.

11

Chapter 2 Interfacing Finite-Size 2D Materials to Engineer Quantum Confinement of Charge Carriers

Reprinted (adapted) with permission from

* Denotes equal contribution.

2.1 Background

Initialization and manipulation of individual quantum states is a critical requirement to achieving high performance optoelectronic devices and quantum information platforms. Thus far, engineering these states has primarily relied on generating deep level color centers/defects as quantum cavities in bulk materials [31] or physically reducing the semiconductor in all three dimensions to make nanocrystals. [32] The energetic tunability of these 3D cavity states is well documented, [33] yet precise electrical or optical control of single quantum states remains elusive. [34,35] Two-dimensional (2D) materials are an attractive platform for quantum confinement due to their electronically

stable surfaces and atomic-scale thickness, which provides perfect confinement in the out-of-plane dimension. [36] Graphene, the most extensively studied 2D material, hosts massless Dirac fermions, which cannot be localized because of carrier transmission regardless of the height or width of the potential barrier (Klein tunneling). [37–40] Several theoretical works have studied forced quantum confinement arising in idealized, isolated graphene disks and triangles with infinite mass gradients at the edges, which have not been experimentally realized. [41–43] Inducing quasi-confinement of relativistic Dirac fermions in graphene can be achieved by introducing a spatially varying bandgap *via* substrate effects (doping or spin-orbit coupling), strong magnetic or electric fields, or adding a second graphene layer. [39,44–47] However, this type of confinement is not a robust intrinsic property of the graphene system, the induced gaps are small (~0.1 eV), and the extreme conditions required to accomplish quasi-confinement are impractical for technological applications. [48]

Continued expansion of the 2D materials library has led to materials with properties distinct from graphene. The family of transition metal dichalcogenide (TMD) monolayers contains many direct bandgap semiconductors with variable composition and tunable bandgaps which have been characterized using density functional theory (DFT) and tight-binding models. [49–53] In stark contrast to graphene, these systems host charge carriers that behave as massive Dirac fermions because the bandgap gives rise to an effective carrier mass that reduces the probability of Klein tunneling. Because these systems are

isostructural with small variations in lattice constant, we can envision structurally coherent in-plane quantum confinement engineered *via* van der Waals (vdW) heterostructuring [54] or lateral epitaxy. [55–57] The band offsets between different TMDs in a heterostructure can be exploited to construct a confining potential step due to the sharp change in the absolute band energies at a clean interface between the two materials. These Dirac carriers are physically distinct from the Schrodinger fermions encountered in epitaxial bulk semiconductor quantum dots [58] due to the symmetric degeneracies of the honeycomb lattice and the occurrence of the direct band gap at non-zero momentum (*K*-point). [59]

2.2 Objective

In this chapter, we develop a multiscale workflow to study the existence and evolution of the bound state spectra of planar quantum dots engineered from TMD heterostructures as a function of their shape and size. The band structures are characterized by first-principles calculations, while tight binding and continuum models are used to describe realistic nanoscale device geometries that are inaccessible to DFT calculations. We explicitly show the bound state energy scaling behavior for massive Dirac fermions in *finite potential wells* corresponding to an experimentally realizable vdW heterostructure. We find that the critical well size and well depth needed to support robust, isolated bound states are achievable in an MoS_2/WS_2 (quantum dot/matrix) heterostructure. Based on these results, we provide simple design rules for atomically thin TMD heterostructure quantum dots to achieve ideal quantum confinement.

14

2.3 Methods

The computational workflow used to model quantum confinement in TMD heterostructures is represented schematically in **Figure 2.1a**. For any two TMDs, MX_2 and $M'X_2$, with direct band gaps at the high symmetry K point, the band structures are calculated *via* DFT. The chalcogen X atom is chosen to be the same in both TMDs to minimize lattice mismatch and ensure that the band gaps remain direct. [60,61] The valence and conduction bands are fit around the K point to obtain the parameters (**Table 2.1**) for a

Table 2.1 Absolute band energy parameters for MoS_2 and WS_2 at the PBE level from Ref. [49], $\boldsymbol{k} \cdot \boldsymbol{p}$ parameters from band structure fitting of MoS_2 in Ref. [62], and computed $\boldsymbol{k} \cdot \boldsymbol{p}$ parameters for WS_2 from band structure fitting around the K high symmetry point. PBE values are used for simplicity because the PBE underestimation tends to correspond to the exciton binding energy for monolayer TMDs. [63]

Model Parameter	MoS_2 Value	WS_2 Value
$\boldsymbol{\Delta}$ (Band gap, eV)	1.59	1.54
a (lattice constant, Å)	3.19	3.19
t (hopping parameter, eV)	1.059	1.075
E_v (valence band max, eV)	-5.86	-5.50
E_c (conduction band min, eV)	-4.27	-3.93
$\boldsymbol{\gamma_1}$ (eV)	0.055	-0.288
$\boldsymbol{\gamma_2}$ (eV)	0.196	-0.639
$\boldsymbol{\gamma_3}$ (eV)	-0.123	0.105

two-band $\boldsymbol{k} \cdot \boldsymbol{p}$ model, which captures the relevant physics of the conduction and valence bands in the K valley. [62]

Figure 2.1b shows an atomistic model of the physical realization of a laterally confined TMD quantum dot system. A TMD with the formula unit MX_2 forms a nanoscale regular triangle or hexagon [64] within an $M'X_2$ matrix. The spatial extent of a quantum dot is defined by $R_\blacktriangle$ and $R_\bullet$, which gives the corner-to-corner distance of the minority material region. The band offsets between the two TMDs create the quantum confinement
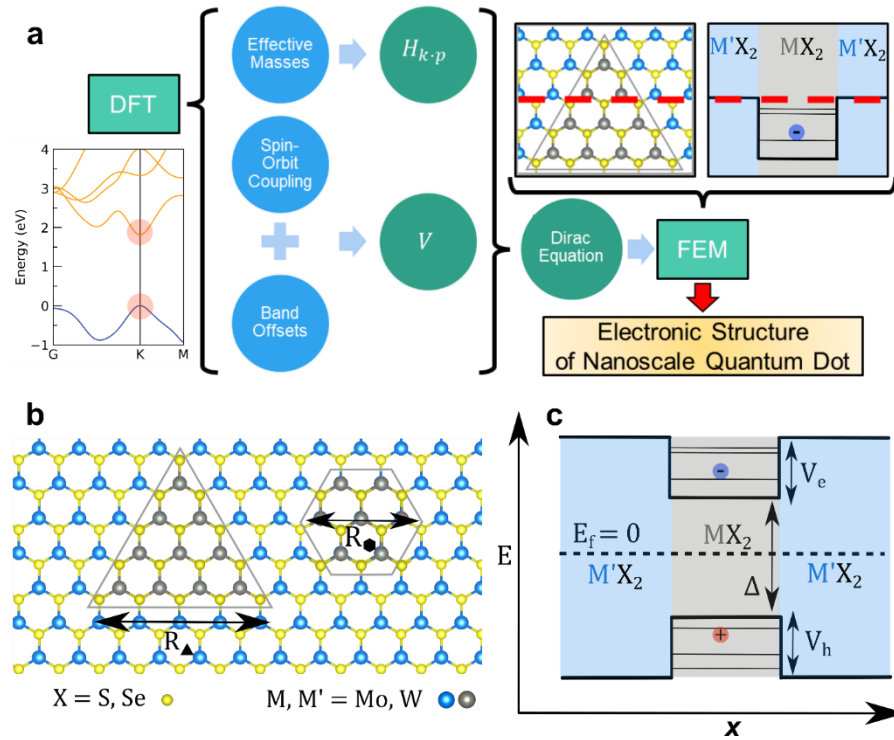
Figure 2.1 Schematic of the continuum approach to describing planar quantum dot electronic structure. **a)** Parameters from density functional theory are used as inputs to a $\boldsymbol{k} \cdot \boldsymbol{p}$ model that is solved for device geometries with the finite element method. **b)** Triangular and hexagonal regions of MX_2 in an $M'X_2$ matrix form 2D quantum dots. **c)** The band offsets between MX_2 and $M'X_2$ create quantum wells for confining electrons and holes.

depicted in **Figure 2.1c**. To describe the spatially dependent band gap variation, we introduce an external finite potential term $V(x)$ given by

$$V(x) = \begin{bmatrix} V_e(x) & 0 \\ 0 & V_h(x) \end{bmatrix} \tag{2.1}$$

where V_e is the conduction band offset and V_h is the valence band offset. $V(x)$ is zero inside the quantum dot and nonzero in the M'X$_2$ matrix. The magnitudes $|V_e|$ and $|V_h|$ control the strength of the confining potentials. If V_e is positive, there is a confining electron potential well in the quantum dot. Likewise, if V_h is negative, there is a confining hole potential well in the dot.

The two-band $\boldsymbol{k} \cdot \boldsymbol{p}$ model to first order in $\boldsymbol{k}$ corresponds to a massive Dirac Hamiltonian, H, which captures the salient structure of the K valley in MoS$_2$, [51] while the second order contribution describes the anisotropic dispersion and electron-hole asymmetry, and including the third order contribution completely recovers the DFT band structure. [53,62,65] We ignore the spin degree of freedom (reducing H to a 2 x 2 matrix) and spin-orbit coupling and include contributions up to second order in $\boldsymbol{k}$, such that the model is given by [62]:

$$H_{kp}^1(\boldsymbol{k}) = \begin{bmatrix} \dfrac{\Delta}{2} & at(k_x - ik_y) \\ at(k_x + ik_y) & -\dfrac{\Delta}{2} \end{bmatrix} \tag{2.2}$$

$$H_{kp}^2(\boldsymbol{k}) = a^2 \begin{bmatrix} \gamma_1 k^2 & \gamma_3(k_x + ik_y)^2 \\ \gamma_3(k_x - ik_y)^2 & \gamma_2 k^2 \end{bmatrix} \tag{2.3}$$

17

where Δ is the direct band gap, a is the lattice constant, t is the hopping parameter, $\gamma_1 - \gamma_3$ are energy parameters, and $k^2 = k_x^2 + k_y^2$. With the Fermi level in the middle of the gap set to zero, the valence band maximum and conduction band minimum of MX_2 are $-\Delta/2$ and $\Delta/2$, respectively, where the band gap of the MX_2 quantum dot is Δ. The top (or bottom) of the potential well is then $\Delta/2 + V_e$ or $-\Delta/2 - V_h$ for electrons or holes, respectively.

We consider two model systems for lateral quantum confinement: an MoS_2 dot in a WS_2 matrix (MoS_2/WS_2), and a WS_2 dot in an MoS_2 matrix (WS_2/MoS_2). The band offsets between these TMDs result in type II band alignment; [66] for MoS_2/WS_2, $V_e = 0.31$ eV, and for WS_2/MoS_2, $V_h = -0.36$ eV. [49] Thus, the first configuration yields an electron potential well, while the second forms a hole potential well. The model $H_{kp}(\boldsymbol{k}, \boldsymbol{x}) = H_{kp}^1(\boldsymbol{k}) + H_{kp}^2(\boldsymbol{k}) + V(\boldsymbol{x})$ can then be numerically solved in the COMSOL MULTIPHYSICS ® package for any device geometry or material combination, given the appropriate parameters. [41] The computed eigenvalues and eigenvectors correspond to the bound state energies and wavefunctions of the quantum dot system.

Finally, a tight-binding model was constructed by considering nearest-neighbor hopping between Mo d_z^2, d_{xy}, and $d_{x^2-y^2}$ orbitals to compare with the results of the $\boldsymbol{k} \cdot \boldsymbol{p}$ model. [62] The tight-binding Hamiltonian for the finite triangular quantum dot includes diagonal submatrices that account for the on-site energies, spin-orbit coupling, and an external scalar potential $V(\boldsymbol{x})$, and off-diagonal submatrices that describe the directional

18

hopping between Mo d orbitals. [67] The external potential was adjusted on the outermost edge of atoms to model the band offset between Mo and W.

2.4 Results

2.4.1 Toy Model: 2D Massive Dirac Hamiltonian in a Radial Finite Potential Well

Our investigation into the existence of bound states in the MoS$_2$/WS$_2$ heterostructure begins with a simple toy model that emphasizes the unusual behavior of the massive Dirac fermions. It is well known that for a particle in a finite potential well described by the Schrodinger equation, the ground state is bound for any arbitrarily shallow or narrow well in one or two dimensions. [68] On the contrary, due to particle-antiparticle conversion, bound state existence is not guaranteed for Dirac fermions and depends explicitly on the form of the potential and the effective fermion mass. There is evidence that the existence of a bound ground state in 2D is uncertain even for simple radially symmetric potential wells. [69,70]

We construct a toy model of the MoS$_2$/WS$_2$ system by approximating the MoS$_2$ quantum dot as a circular region in a radially symmetric finite potential. Following DiVincenzo and Mele, [71] we solve the massive Dirac Hamiltonian for a finite potential to develop straightforward existence criteria for bound states in the MoS$_2$/WS$_2$ quantum disk system. For simplicity, we consider the simplified Hamiltonian $H(\boldsymbol{k}, \boldsymbol{r}) = H^1_{kp}(\boldsymbol{k}) +$

19

(r) and set the finite band offset $V_e = V_h = V_0$, such that $V(r < r_0) = 0$ and $V(r > r_0) = V_0$, where r_0 is the radius of the MoS$_2$ dot and r is the radial coordinate. Since we are interested in potential well dimensions that support at least one bound state, we restrict the solution space to the ground state, where the angular quantum number $m = 0$. We apply continuity boundary conditions to the wavefunction at the well edge $r = r_0$ and look for bound state solutions with energy E in the range $\frac{\Delta}{2} < E < \frac{\Delta}{2} + V_0$. To exclude quasi-bound states, we only allow terms in the wavefunction which exponentially decay as $r \to \infty$. [47] This leads to a transcendental equation for the bound state which must satisfy:

$$\frac{Re[Y_0(-r_0\alpha_V)]}{J_0(r_0\alpha_W)} = \frac{i\alpha_V}{\alpha_W}\frac{E + \frac{\Delta}{2}}{V_0 - E - \frac{\Delta}{2}}\frac{Im[Y_1(-r_0\alpha_V)]}{J_1(r_0\alpha_W)} \tag{2.4}$$

where

$$\alpha_W = \frac{\sqrt{E^2 - \left(\frac{\Delta}{2}\right)^2}}{at}, \alpha_V = \frac{\sqrt{E^2 - \left(\frac{\Delta}{2}\right)^2 - 2EV_0 + V_0^2}}{at}.$$

Here J_n and Y_n are the Bessel functions of the first and second kind, and Δ, a, and t are material parameters corresponding to the bandgap, lattice constant, and hopping energy taken from $H_{kp}^1(\boldsymbol{k})$. The limiting behavior and details of obtaining Eq. 2.4 are discussed in the Appendix S2.1. We numerically solve for the roots of Eq. 2.4 and plot (**Figure 2.2a**) the lowest bound state energy as a function of the dimensionless quantities $\frac{V_0}{\Delta}$ and $\frac{at}{\Delta r_0}$. The phase map provides a completely general estimate of the ground state energy for any

material parameters, with darker contours representing ground states closer to the bottom of the potential well and lighter contours approaching the top of the well.
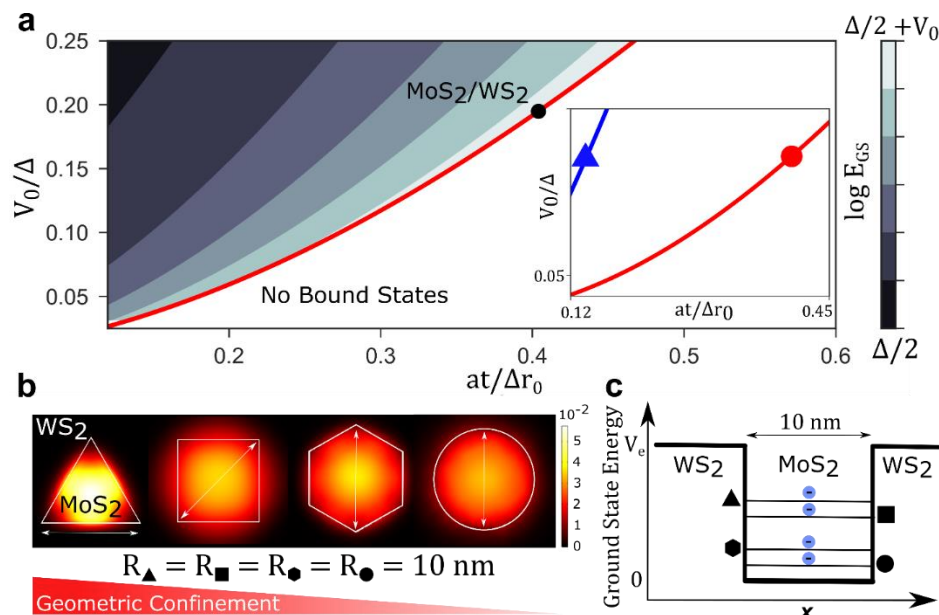
Figure 2.2 a) Phase diagram for bound state existence as a function of heterostructure parameters Δ (band gap), V_0 (confining potential magnitude), a (lattice constant), t (**k.p** hopping energy), and r_0 (dot radius), for the toy model circular finite well. The inset shows comparison with bound state existence boundary taken from numerical solutions for triangular wells. **b)** Evolution of the ground state probability density showing decreasing localization with increased number of vertices for dots with equivalent corner-to-corner length. **c)** Ground state energy relative to the continuum band edge corresponding to the dot geometries in **b)**.

In our model system of an MoS$_2$ dot in a WS$_2$ matrix, we find that minimum values of r_0 and V_0 define a phase boundary beyond which no bound states are supported. This behavior is particular to massive Dirac fermions in 2D. In contrast with a 2D Schrodinger quantum dot where confinement effectively disappears beyond some maximum diameter, in the Dirac quantum disk there is additionally a minimum critical size beyond which there is no confinement due to the Klein effect. This condition can also be achieved by taking Δ to 0 at finite V_0 and fixed size r_0, which recovers the massless graphene case. For the toy model MoS$_2$/WS$_2$ system with a conduction band offset $V_0 = V_e = 0.31$ eV, we find that the circular well has a critical radius of 2.6 Å, which is less than one unit cell. However, for more realistic quantum dot geometries that are not radially symmetric, the critical radius will be larger. In the limit of small r_0, breaking the radial symmetry of the quantum disk and introducing a three-fold rotational symmetry shifts the critical bound state phase boundary in a non-trivial way, increasing the minimum critical size for the MoS$_2$/WS$_2$ system from 0.5 nm to 1.5 nm (**Figure 2.2a**, inset). These critical sizes are highly dependent on the band offset, and the criteria are more restrictive for confining wells with smaller band offsets. Having shown the existence of bound states for massive fermions in TMD heterostructures, we next turn to exploring the effects of realistic quantum dot geometries on confinement.

2.4.2 Bound State Spectra in Triangular and Hexagonal Dots – Continuum Approach

Several different quantum dot geometries are accessible based on the crystal symmetry of the component TMD materials and synthesis conditions. [64] We compute the ground state using the continuum method for a circular quantum dot, finding quantitative agreement with the toy model results ($E_{analytic} - E_{continuum} = 0.5$ meV, which equals the $E(H_{kp}^2)$ correction absent from the toy model), and then repeat the process for hexagonal, square, and triangular geometries. **Figure 2.2b** shows the evolution of the ground state wavefunction as the number of vertices in the dot geometry increases from three (triangle) to infinity (circle), with the vertex-vertex distance fixed at 10 nm (significantly above the bound state existence boundary). At this size, at least one bound state is present for the MoS$_2$/WS$_2$ system in all geometries, but as shown in **Figure 2.2c**, the energy of this state relative to the band offset varies considerably. This is primarily explained by the fact that the dot area is minimized for a given vertex-vertex length in the triangle, and this reduction in area manifests as an effective geometric confinement. The sensitivity of the ground state energy to this geometrical effect is an important consideration for device design, as the transition from a hexagonal dot to a triangular dot (two common geometries in TMD flake systems) [58,59] in the model system increases the ground state energy by a factor of almost three (30 meV vs 80 meV). Therefore, the triangular system is better for engineering confinement at larger dot sizes, which may be advantageous for experimental observations.

Since triangular and hexagonal shapes are frequently observed for TMD monolayers due to the hexagonal unit cell, we focus on these geometries to investigate the evolution of the electron and hole ground states with system size. To engineer quantum confinement, we determine the maximum and optimal dot sizes for hosting bound states. We systematically vary $R_{\blacktriangle}$ and $R_{\bullet}$ and compute the ground state energies for each geometry. The electron (**Figure 2.3a**) and hole (**Figure 2.3b**) ground state energies are plotted *versus* inverse side length for triangular (green points) and hexagonal (blue points) geometries to show the characteristic scaling. The corresponding $R_{\blacktriangle}$ and $R_{\bullet}$ values are given on the upper x-axis for convenience. Rescaling the energies such that $\frac{\Delta}{2}$ (the bottom of the well) corresponds to 0, we see a monotonic decrease in the electron ground state with increasing dot size. For small dots ($R_{\blacktriangle} < 5$ nm), the ground state energy is close to the top of the electron well. The quantum confinement persists for large dots ($R_{\blacktriangle} > 20$ nm), as the ground state approaches the bottom of the potential well. This confinement predicted for large nanoscale geometries is a consequence of the ideal confinement in the out-of-plane direction in these

24
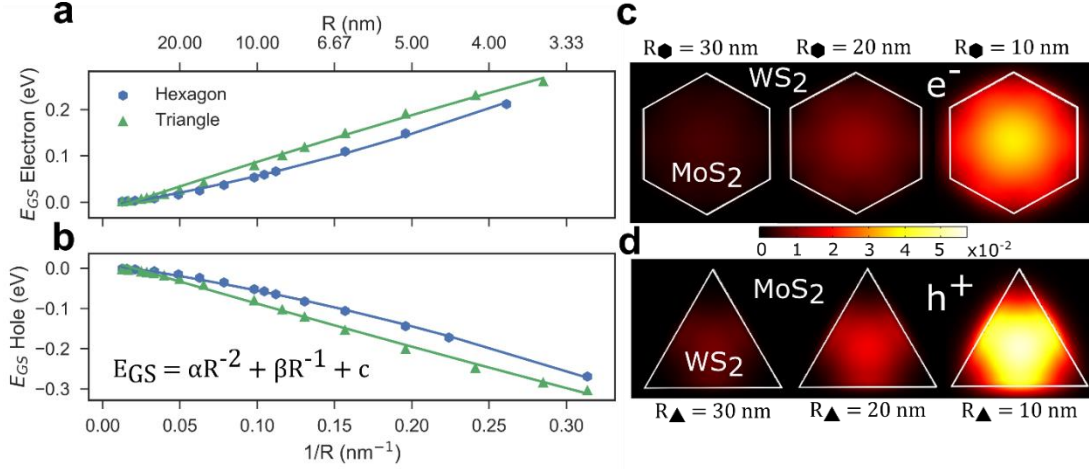
Figure 2.3 Scaling of the electron and hole ground states with inverse side length. **a)** Electron and **b)** hole ground state energies for triangular (green) and hexagonal (blue) quantum dots show a characteristic dependence on quantum dot size. **c)** Electron and **d)** hole ground state wavefunctions delocalize with increasing quantum dot size.

2D structures, despite the finite nature of the potential barrier and relativistic properties of the carriers.

The ground state energy dependence on quantum dot size follows the simple relation

$$E_{gs}(R) = \alpha R^{-2} + \beta R^{-1} + c \tag{2.5}$$

where R is length, α and β are materials-dependent constants, and c is a constant specified to set the bottom of the potential well equal to zero. This scaling with inverse length and inverse length squared follows immediately from the expansion in $\boldsymbol{k}$ (which has units of inverse length) in the $\boldsymbol{k} \cdot \boldsymbol{p}$ model. The ground state energy for any geometry is then totally

specified by the α and β coefficients for a given MX$_2$/M'X$_2$ pair. The same characteristic scaling behavior is seen for holes in WS$_2$/MoS$_2$ (**Figure 2.3b**).

Visualizing the ground state wavefunctions provides a qualitative picture of the extent of quantum confinement. **Figure 2.3c** shows the electron ground state wavefunction in hexagonal MoS$_2$ quantum dots with $R_\bullet$ = 10, 20, and 30 nm. At $R_\bullet$ = 10 nm, the wavefunction is strongly localized. The amplitude is large at the center of the dot and radially decays, as expected. As the area of the hexagon increases, the wavefunction becomes increasingly delocalized until confinement is no longer apparent. At this point, the ground state of the system is indistinguishable from the infinite periodic band structure, and the finite dot region is no longer discretely quantized. The same wavefunction delocalization is observed for hole ground states in triangular WS$_2$ dots with increasing area (**Figure 2.3d**). Finally, to verify the validity (and limitations) of the continuum approach, we repeat the analysis at small dot sizes using both a three-band tight-bonding model [62] and a higher-order $\boldsymbol{k} \cdot \boldsymbol{p}$ model shown in Appendix S2.2.

Having considered the ground state energy-size scaling for electrons and holes, we reduce the model MoS$_2$/WS$_2$ system to just triangular dots and consider the complete bound state spectrum as a function of dot size. To compute all the bound states, we iteratively solve the eigenvalue problem over the entire range of energies in the potential well and extract the smooth eigenstates. **Figure 2.4a** shows some representative bound state spectra with energies referenced to the bottom of the well (M'X$_2$ band edge). At 5 nm side length (**Figure 2.4a**, top), the MoS$_2$ well effectively supports only one bound state, with an

additional bound state appearing at the very top of the potential well. As the MoS_2 well region is enlarged, the number of bound states increases, and the energy of the ground state reduces towards the energy of the pristine monolayer band edge. **Figure 2.4**a also shows
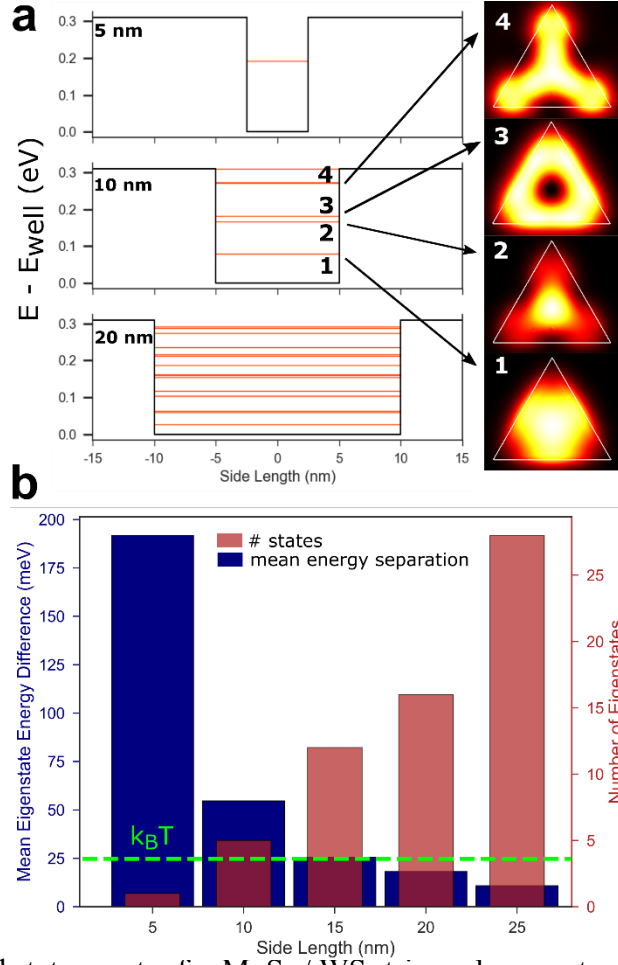
Figure 2.4 a) Bound state spectra for MoS$_2$ / WS$_2$ triangular quantum dots as a function of dot size. A sample of wavefunctions is shown for the 10nm well; wavefunctions possess 3-fold rotational symmetry of the confining geometry. **b)** Bound state energy spacing and effective density of states vs. size of the dots in **a)**. The average state spacing rapidly drops below $k_B T$ @ 300 K as the confinement decreases.

the probability density of the electron wavefunctions, $|\Psi_e|^2$, corresponding to the first 4 eigenstates of the confined system. The closely spaced states visible near eigenstate 2 and

3 are due to differing contributions from the valence band wavefunction with different angular momentum quantum numbers; this occurs at all higher energy eigenstates, but the energy splitting is small. Due to the inclusion of $H_{kp}^2(\boldsymbol{k})$, we avoid the common fermion doubling problem that arises in discretizing Dirac Hamiltonians by introducing an effective Wilson mass. [74] As expected, the symmetry of the excited eigenstates matches the confining geometry of the finite potential well. Examples for hole wavefunctions in hexagonal confined WS$_2$ dots are given in the Supporting Information. At 20 nm (**Figure 2.4a**, bottom), the eigenstates are collapsing into a continuum description. At this size, the high area to depth ratio of the well means that the potential step at the well edges is no longer impacting the wavefunction in the center of the well.

Figure 2.4b gives a quantitative description of the bound state spectrum evolution with increasing dot size from 5 to 25 nm. The blue columns show the average energy spacing between eigenstates for a particular dot size, including the energy separation between the ground state and the well bottom. For a fixed well depth, the average energy spacing between states decreases rapidly with increasing side length, crossing $k_B T \cong 25$ meV at 15 nm, which means that the average state is no longer thermally isolated at room temperature. The red columns give the number of bound states in the well as the side length increases up to 25 nm, when the ground state is within $k_B T$ of the continuum band edge and effectively merges with the continuum. In the design and synthesis of solid-state quantum dots for optoelectronic applications, this threshold should be kept in mind as a heuristic to minimize thermally induced decoherence due to increasing density of states

29

near the desired excitation. Akin to the determination of the critical maximum size for confinement, this threshold arising from neighboring excited bound states places a restrictive practical constraint on feasible quantum dot configurations.

2.4.3 Design Rules for Optimized Realization of Quantum States

Synthesizing the results presented above, we outline a general design scheme in **Figure 2.5** to optimize quantum confinement in 2D semiconductor heterostructures. For any combination of layered TMD semiconductors, absolute band energies and $\mathbf{k} \cdot \mathbf{p}$ parameters can be obtained from first principles calculations on pristine periodic systems (**Figure 2.5a**). From these parameters, finite size effects can be explored at length scales that are experimentally accessible but beyond the scope of DFT calculations or tight-binding models. From the phase diagram in **Figure 2.2**, bound state existence can be determined based on the DFT parameters for the pristine monolayers. If bound states exist, we can assess the robustness of the planar quantum dot confinement using two basic figures of merit: $F_1 = \left| \frac{\Delta E_{GS}}{V_{well}} - 0.5 \right|$, the percent deviation of the ground state from the center of the well, and $F_2 = \Delta E_{ES-GS}$, the energy spacing between the ground state and the first excited state (**Figure 2.5b**). These metrics characterize the degree of isolation for a quantum state that is energetically centered between the band edges of the component materials. An optimal, isolated state has the best chance of withstanding perturbations caused by edge states or atomic defects, without knowing *a priori* where the dominant defect levels exist for a given semiconductor heterostructure. To achieve such a state, we

30

need to simultaneously minimize F_1 and maximize F_2. **Figure 2.5c** and **Figure 2.5d** plot F_1 and F_2 as a function of the dimensionless scaling variables $at/\Delta r_0$ and V/Δ, where V is the band offset in the confining well, along with examples of TMD heterostructures based on their band structure parameters. Since the band offsets are not identical for TMD heterostructures as they were in our toy model (**Figure 2.2**), and there is some mixing

between the two bands, this parametrization lacks a dependence on the difference between
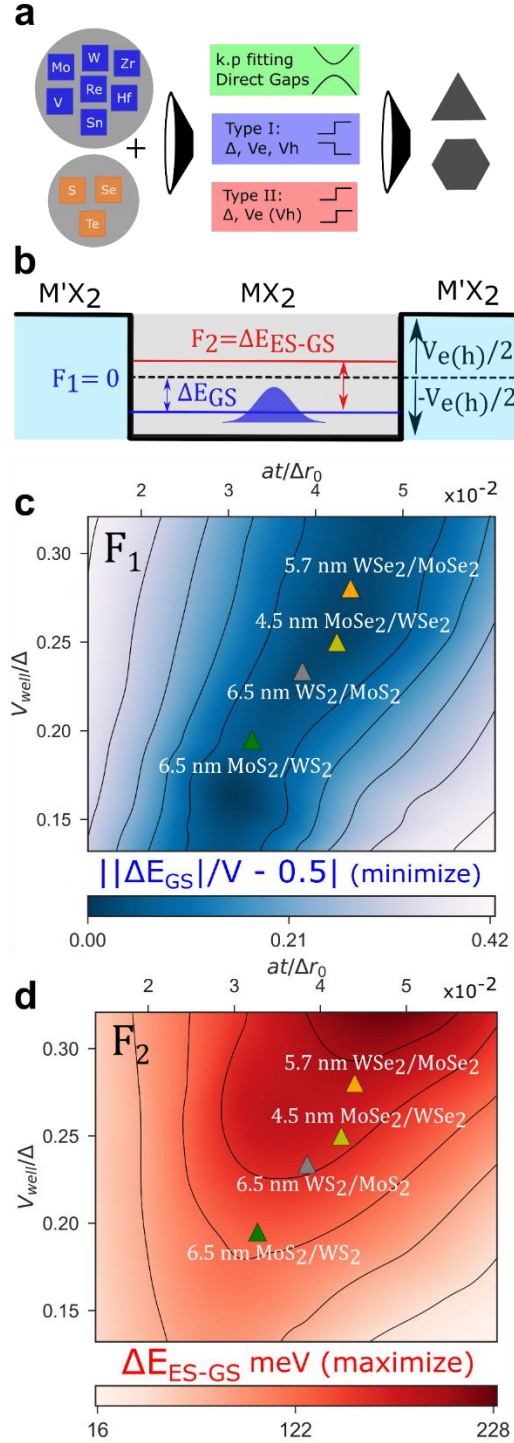
Figure 2.5 a) Design workflow for forming confining TMD heterostructures. **b)** Figures of merit for evaluating the performance of an MX_2 quantum dot in isolating a single quantum state. $\frac{\Delta E_{GS}}{V} - 0.5$ measures the percent deviation from the center of the well, and ΔE_{ES-GS} gives the energy separation between the ground state and the first excited state. **c, d)** Design optimization diagrams for the figures of merit in **b)**, with results for different TMD heterostructures in several dot configurations overlaid.

V_h and V_e. We take $V_0 \approx V_{e(h)}$ for confined electrons (holes) to preserve simplicity, because the $V_e - V_h$ coupling correction to the ground state energy is small.

For type II band alignment, the optimization shows that deeper wells (corresponding to a larger band misalignment between the two semiconductors) lead to greater energy separation between the ground and first excited state at a fixed dot area. The same is true for the ground state energy spacing from the well bottom. In the MoS_2/WS_2 system, there is an optimum triangular side length of ~6.5 nm that corresponds to the maximally centered ground state in the middle of the well, whereas for $MoSe_2/WSe_2$, this optimum size is closer to 4.5nm. TMD monolayer flakes with spatial extent < 10 nm have been synthesized, making these systems both practical and ideal for nanoscale quantum confinement. [75–80] Recently, both bottom-up [55,81] and top-down [82,83] approaches have demonstrated high control over 2D heterostructure features on this length scale, within the bounds of the kT threshold identified in **Figure 2.4b**.

The optimal size asymmetry between confined electrons and holes in the selenide system arises from a change in the hopping energy between the molybdenum and tungsten compounds. In the sulfide system, a similar hopping energy difference is counterbalanced by a change in the band gap which does not occur in the selenide system. In smaller dots at constant band offset, the ground state approaches the top of the well, eventually leading to the phase boundary for bound state existence seen in **Figure 2.2**. Furthermore, increasing the lattice constant or hopping energy at a fixed offset also increases the confinement for a

fixed geometry. For shallow wells, larger dot sizes are preferable to realize bound states far from the background band edges, which may have relevance for Moiré superlattice engineering. Overall, these findings lead to the surprising and important conclusion that, rather than naively minimizing the dot area, optimal confinement is achieved by tuning the quantum dot spatial extent to a precise value that depends sensitively on the material parameters.

2.5 Conclusion

In this chapter we have presented and analyzed a lateral TMD heterostructure architecture for ideal quantum confinement. In doing so, we demonstrated a multiscale computational approach for optimizing realistic material and device parameters to achieve robust, coherent single quantum states in ambient conditions. By considering a toy model of a 2D quantum well, we established the criteria for supporting bound states in a TMD heterostructure and clearly emphasized the advantage of intrinsic confinement of massive Dirac fermions, compared to graphene which supports only quasi-bound states under applied fields. With a continuum method for solving a two-band $\boldsymbol{k} \cdot \boldsymbol{p}$ model, geometric effects were shown to play an important role in engineering robust confinement, with triangular 2D quantum dots exhibiting maximal geometric confinement. The ground state energies scale with the system size as $\alpha R^{-2} + \beta R^{-1}$, such that the lowest bound state energy can be predicted for any size and shape of quantum dot simply by computing the material dependent coefficients α and β *via* fitting to continuum results. Performance

metrics for confinement were proposed in terms of the energetic isolation of the ground state from both bulk band edges and neighboring excited states. Optimizing for these metrics in an MoS_2 triangular quantum dot in a WS_2 matrix results in a prediction of ~6.5 nm side length for optimal confinement. Moreover, we predict optimal geometries for arbitrary heterostructures of TMDs, and our formalism can easily be applied to any 2D semiconductor heterostructure. Our findings establish straightforward design principles for engineering optimal 2D quantum confinement at room temperature that should be of immediate use in the experimental realization of coherent quantum states.

Chapter 3 Interfacial Phenomena in Synthesis of Layered Materials

Reprinted (adapted) with permission from

3.1 Background

Hybrid organic-inorganic lead halide perovskites (AMX_3; A = small organic or large alkali cation, M = Pb, Sn, Ge, X = I, Br, Cl) have been extensively studied as ideal solution-processable semiconductors with excellent visible-range optical properties, but they have been crippled by their thermodynamic instability to water erosion in ambient conditions. [84–88] Replacing a portion of the A cations with hydrophobic large organic molecules (A') can lead to layered perovskite structures where the intercalated large molecules interrupt the MX_3 octahedral network, resulting in a self-assembled organic – inorganic lamellar composite material which resists moisture degradation. [89–93] Synthetic advances such as hot-casting have led to increased control over the growth orientation and stoichiometric ratio of these $A'_2A_{N-1}M_NX_{3N+1}$ compounds (A' = large organic molecule), where the stoichiometric index N corresponds to the ratio of hydrophobic cations to perovskite semiconductor. [91,94–99] In single-phase materials, manipulation of the chemical composition (N) controls the thickness of the perovskite layer and thus the magnitude of quantum and dielectric confinement effects on the electronic and

optical properties. [100–106] This makes these materials an ideal optoelectronics platform

even beyond their enhanced stability. [107]

The compositional phase space of these materials is vast due to the chemical

degrees of freedom at each site in the structure, particularly at the organic A and A' sites.

Most studies have focused on the A' = n-butylammonium (BA; $CH_3(CH_2)_3NH_3^+$), A =

methylammonium (MA; $CH_3NH_3^+$), M = Pb, X = I system; this was one of the first 2D

perovskites synthesized [90] and its 3D analogue $MAPbI_3$ is the most widely studied

member of the 3D hybrid perovskites. In pure phases, this material has been frequently

reported and studied in the low-N phases (N < 5), [89,91,95,96,99,108–115] and reported

only twice for N > 5. [116,117] In these recent studies, Soe $et.$ $al.$ found it more difficult

to isolate single crystals of the higher N phases, finding impurity phases in the XRD spectra

at stoichiometric ratios corresponding to N = 6, 7, and 9 with the amount of multi-phase

mixing increasing with N. Mao $et.$ $al.$ reported similar results for their Ruddlesden-Popper

N = 7 synthesis and suggested that the growth environment is kinetically constrained.

Recently expanding synthetic efforts have focused primarily on varying the A' cation;

examples include guanidinium (GA), [118] phenylethylammonium (PEA), [119–122]

fluoro-PEA (f-PEA), [123] N,N-dimethylphenylene-p-diammonium (DPDA), [124] n-

propylammonium (PrA), [125] n-pentylammonium (PA), [126] n-hexylammonium

(HA), [126] and 3(4)-(aminomethyl)piperidinium (3-(4-)AMP) [117,127] (full chemical

formulae can be found in Table S1 of [128]). These compounds have all been synthesized

exclusively in the low-N phase regime (N < 5) except for PEA and 4-AMP. PEA has been reported as synthesized with an average stoichiometry <N> = (10, 20, 40, 60) phases consisting of a mix of competing phases, and 4-AMP has been synthesized in the N = 7 pure phase. [98,117] The gap in the single-phase behavior at the critical N value of 5 for BA and other linear-chain A' cations is surprising since both the low N < 5 and very high N = ∞ (bulk) phases are readily synthesized. Single phase intermediate N compounds would improve carrier transport by reducing exciton binding energies while retaining the highly ordered layered structure and creating opportunities for favorable band alignment in heterostructures. However, it is difficult to draw general physical insights about this phase behavior from the synthetic efforts discussed above due to the multitude of thermodynamic and kinetic factors varying between studies.

3.2 Objective

In this chapter, we develop a continuum thermodynamic model parametrized by atomistic first-principles density functional theory (DFT) calculations to map the phase space and study the critical phase behavior of the quasi-2D layered perovskites (q-2DPKs). Focusing on the A' = BA system as a representative example, we find that the critical N value of 5 arises from electromechanical competition between the interfacial stress of the MX_3 octahedral network and the interfacial dipole interactions across the inorganic layer. We show that this competition also drives non-monotonic evolution of the lattice parameters with N, which is relevant to the electronic properties of each phase. We find

that the N critical value can be tuned through the interfacial dipole moment, which can be constructed as a sum of the surface dipole moment of the bulk perovskite and the intrinsic dipole moment of the A' cation. This means that the choice of A' cation can have an equal or greater impact on the structural phase space than the choice of the specific perovskite network. These results will enable engineering of phase pure q-2DPKs in intermediate composition ranges with long term thermodynamic stability for enhanced electronic and optical properties.

3.3 Methods

3.3.1 Atomistic Overview and Model Approach

We first map the family of q-2DPK to a two-component mixture of A' cations and bulk 3D perovskite (PK) that forms a composite system of layers (**Figure 3.1a**, **Figure 3.1c**), focusing on the system where A' = BA and PK = MAPbI$_3$. At 300 K, MAPbI$_3$ forms in a tetragonal phase with nearly isotropic rotational disorder of the MA cations. [129] The Pb^{2+} and MA^{+} cations are caged in an electron accepting iodine network which forms corner-sharing octahedra around the lead ions. To replicate this, we fix the lattice parameters in the tetragonal configuration and use green spheres to represent the MA^{+} cations; the orientation of the MA cations has been shown to negligibly impact the electronic properties. [94,130] Further details can be found in the Methods and Supporting Information. The BA A' cation is comprised of a four-carbon backbone with an NH$_3^+$ ammonium group at one end. When substituted for MA in the bulk perovskite, the long

carbon chains interrupt the halide network, leading to alternating layers of A' cation

$(BA_2)^{2+}$ and perovskite $(A_{N-1}Pb_NI_{3N+1})^{2-}$ with a thickness corresponding to the A/A'

stoichiometric ratio. The quasi-unit cells of these structures are shown in **Figure 3.1c**. The

full unit cell includes two A' cation layers and two perovskite layers due to the Ruddlesden-

Popper stacking, with experimentally characterized space groups of C2cb for odd-N phases

and Cc2m for even-N phases. [89,116,131]. With such a large number of atoms in the unit

cell for $N > 1$ structures, it is practically impossible to perform wide-ranging *ab initio*

calculations on the family of q-2DPKs, and the few existing modelling reports are based

on semi-empirical approaches. [94,105] This greatly emphasizes the need for a continuum

model to describe the thermodynamics of these materials. The layered structures undergo

a small $(< 2\%)$ orthorhombic distortion from the tetragonal $MAPbI_3$ parent phase at 300 K,

which we ignore in the model for simplicity. [94]
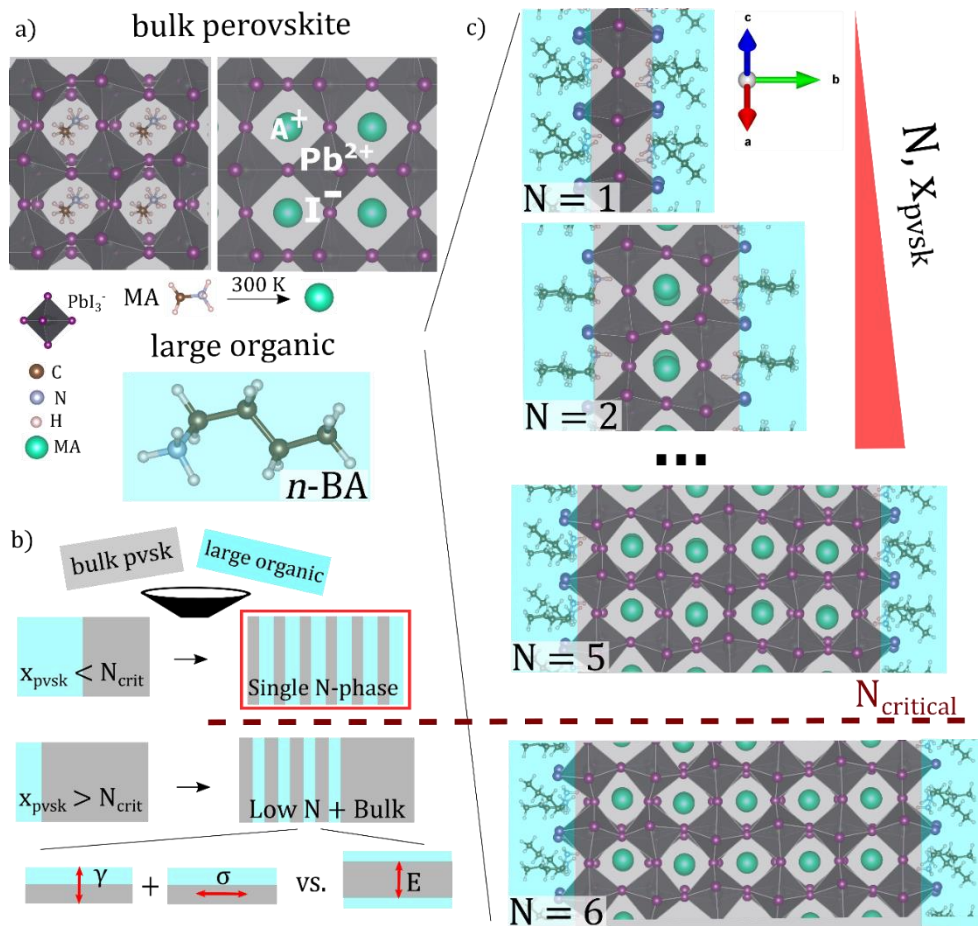
Figure 3.1 a) Atomistic overview of the parent perovskite phase (MAPbI$_3$) in low and room temperature structures; replacing some MA with an A' cation (*n*-butylammonium) leads to the layered structures in **b)**. **b)** Quasi- unit cells of the 2D layered perovskites. N counts the number of PbI$_3$ octahedra between large organic layers; phases with N > 5 (N$_{crit}$) are not synthesized in phase pure form. **c)** Macroscopic thermodynamic outcomes of the two component A' (cyan) + bulk (gray) perovskite composite material. For uniform electronic properties, a single N-phase (red box) morphology is ideal.

The stoichiometric index N corresponds to the amount of BA cation incorporated into the structure and can be visualized as the number of PbI_3 octahedra spanning the inorganic layer in the **b** lattice direction. We also define the perovskite atom fraction x_{pvsk} as the fraction of atoms in the sample which do not belong to the BA cation. **Figure 3.1b** outlines how x_{pvsk}, N, and the critical N value (N_{crit}) are related; for a composition x_{pvsk} of bulk perovskite and BA cations corresponding to a single phase N value <= N_{crit}, single phase crystals are observed. For x_{pvsk} compositions corresponding to N > N_{crit}, two-phase or multi-phase mixtures of low-N (N < N_{crit}) phases and bulk perovskite ($N = \infty$) are observed. The homogeneous morphologies highlighted in red are desirable for well-defined optical and electronic properties. Recent results have indicated that N_{crit} is dependent on the A' cation chosen in the system, [117] and different choices of A and A' cations may prevent layered composite formation altogether. In our model, we propose that N_{crit} is not a spurious kinetic effect but emerges as a result of thermodynamic competition between the mechanics of the composite interface and the electrostatic repulsion of adjacent interfaces across the perovskite layer.

3.3.2 Computational Details

First-principles DFT simulations were carried out using the Vienna *ab initio* simulation package (VASP). [20,21] Projector-augmented wave pseudopotentials [132] are used with a cutoff energy of 520 eV for plane-wave expansions. [16] The exchange-correlation is treated using the Perdew-Burke-Ernzerhof (PBE) generalized gradient

approximations. The atomistic structures of isolated, symmetric perovskite slabs were relaxed using Γ-centered *k*-point meshes of 7x1x7, while fully periodic structures were sampled at 7x3x7. Bulk structures are relaxed using similar meshes of 7x5x7. For structural relaxations, the atomic positions of all unit and supercells are optimized until the force components on each atom are less than 0.005 eV/ Å, and the electronic energy is converged within 10^{-8} eV. Tight convergence criteria are required due to the shallow nature of the perovskite potential energy surface. A vacuum spacing of 20 Å was added to slab calculations to prevent interactions between periodic images, as well as dipole corrections to the energy and potential in the case of isolated molecules or asymmetric slabs. Long range van der Waals dispersion interactions between organic and inorganic components were treated using the DFT-D3 method developed by Grimme *et. al.* [133,134] Following previous studies, [94] the lattice parameters were fixed in a tetragonal configuration for atomic relaxations to simulate the room temperature phase of $MAPbI_3$, and Cs atoms were used instead of MA cations to increase the rotational symmetry of the A cation site and reduce computational cost (**Figure 3.1a**). All calculated properties were verified to be minimally affected by the cation switch.

3.4 Results

3.4.1 Strain-Dependent Free Energy of the Composite A' / Perovskite System

To develop general insights about the composite layered organic-inorganic system, we map the atomistic structure into a continuum model of interacting slabs with two BA-

43

adsorbed interfaces, as shown by the black dashed box in **Figure 3.2a**. As in **Figure 3.1**, we color-code the 'bulk' perovskite regions gray and the all-organic BA regions cyan and identify the critical chemical and mechanical variables contributing to the thermodynamics of the mixture. The overall chemical reaction forming the layered structure is:

$$2BAI_{(s)} + PbI_{2\,(s)} + (N-1)MAPbI_{3\,(s)} \rightarrow BA_2MA_{N-1}Pb_NI_{3N+1\,(s)} \qquad (3.1)$$
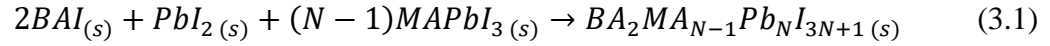
We begin by writing the total free energy of the system as $G_{tot} = G_0 + \Delta G_{mix}$, where $G_0 = x_{BAI}G_0^{BAI} + x_{MAPbI_3}G_0^{MAPbI_3} + x_{PbI_2}G_0^{PbI_2}$ gives the composition-weighted free energy of formation of the q-2DPK components and ΔG_{mix} captures the free energy of mixing the constituents. $G_0^{PbI_2}$ is necessary to describe the N = 1 compound where the A' cation has replaced all of the A cation, but since this is the lower limit of the stoichiometric range we are interested in, it can be added into $G_0^{MAPbI_3}$ as a constant, which is done from here on. Since the layered phases are all highly ordered and the entropy of crystallization for BAI is small, [135] we take $S_0 \approx 0$ and $\Delta S_{mix} \approx 0$. With these simplifications, we can use the
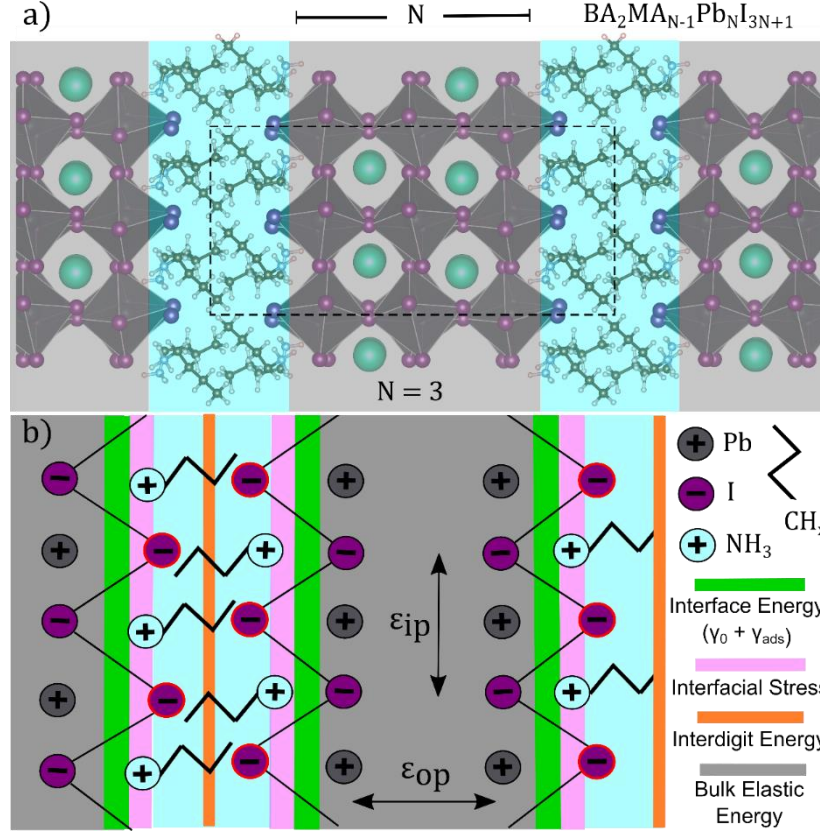
Figure 3.2. a) Zoomed view of the periodic layered perovskite structure. The dashed line shows the slab unit cell used to parametrize the continuum model. **b)** Schematic for the basis of the continuum model. The interfaces are denoted by the undercoordinated iodine atoms (red outline) where the BA cation has broken the Pb-I bond. The key interactions are shown in green (interfacial energy: surface energy + adsorption energy), pink (interfacial stress of the perovskite), orange (interdigitation energy of the BA molecules), and gray (perovskite layer with bulk elastic energy). The elastic degrees of freedom are the in-plane strain ε_{ip} and out-of-plane strain ε_{op}.

composition fraction x_{pvsk} introduced earlier so that $G_0 = (1 - x_{pvsk})H_0^{BAI} + x_{pvsk}H_0^{MAPbI_3}$ and $\Delta G_{mix} = \Delta H_{mix}$. As an atom fraction, $x_{pvsk} = \frac{n_{pvsk}}{n_{tot}}$, where n_{pvsk} is the number of atoms belonging to the perovskite layer and n_{tot} is the total number of atoms in

45

one formula unit of $BA_2MA_{N-1}Pb_NI_{3N+1}$. Based on the atom counts in each component, x_{pvsk} and N are related through $N = \frac{27+7x_{pvsk}}{12(1-x_{pvsk})}$. The formation energies of the bulk components are calculated from atomic reference states using DFT according to the following reactions:

$$H_0^{BAI} = \Delta H_f: \ 4C_{(s)} + \frac{1}{2}N_2 + \frac{1}{2}I_2 + 6H_2 \ \rightarrow CH_3(CH_2)_3NH_3I \tag{3.2}$$
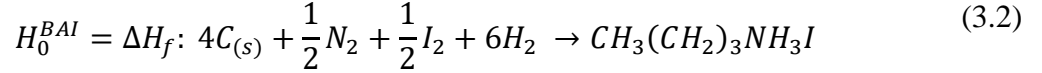
$$H_0^{MAPbI_3} \tag{3.3}$$

$$= \Delta H_f: \begin{cases} Pb_{(s)} + I_2 \rightarrow PbI_2 & N = 1 \\ 2Pb_{(s)} + \frac{5}{2}I_2 + \frac{1}{2}N_2 + C_{(s)} + 3H_2 \rightarrow MAPbI_3 + PbI_2 & N > 1 \end{cases}$$

where $MA = CH_3NH_3$.

Next, we develop the mixing enthalpy ΔH_{mix} of the BA cations and bulk perovskite, which describes the 2D interfaces formed on each side of the perovskite slab (**Figure 3.2b**). The interfacial energy (green) is a combination of the energy cost of cleaving the perovskite by breaking the Pb-I bonds γ_0, and the adsorption energy γ_{ads} of the large organic cations onto the cleaved perovskite surface. The sum of γ_0 and γ_{ads} gives the mechanically uncoupled interfacial energy; these and other material parameters described below are calculated using DFT, as detailed in Ref. [128]. Based on experimental evidence, [89,116] the lattice parameters of the layered structure evolve with N, so we introduce two elastic degrees of freedom within the gray perovskite domain only:

the in-plane strain parallel to the interface ε_{ip} and the out-of-plane strain perpendicular to the interface ε_{op}, which are taken relative to the PK experimental lattice constants at room temperature measured by Whitfield *et al*. [129] These strain degrees of freedom contribute through the interfacial stress $f_{ss} = \frac{\partial \gamma_0}{\partial \varepsilon_{ip}} \varepsilon_{ip}$ (**Figure 3.2b**, pink) and the bulk elastic energy for a tetragonal unit cell $E_B = \frac{1}{2}(2C_{11}\varepsilon_{ip}^2 + C_{22}\varepsilon_{op}^2 + 4C_{12}\varepsilon_{op}\varepsilon_{ip} + 2C_{13}\varepsilon_{ip}^2)$, where C_{ij} are the elastic stiffness constants in Voigt notation. These two terms compete due to the different bonding environments at the organic-inorganic interface and the interior of the perovskite slab. [136,137] f_{ss} is parametrized by calculating the linear change of the free perovskite surface energy γ_0 with in-plane strain ε_{ip}, while E_B is calculated using the elastic constants of bulk MAPbI$_3$. [138,139] The corresponding elastic energy of the soft organic layer and organic contributions to f_{ss} are verified to be small in comparison and ignored, but the van der Waals (vdW) interactions between the BA molecules belonging to adjacent interfaces are captured by $U_{interdigit}$ (**Figure 3.2b**, orange). This is calculated as the energetic difference between isolated symmetric BA-adsorbed perovskite slabs and the fully periodic layered structure. [128] Normalized to energy per atom, the strain-dependent energy of forming the individual A' / perovskite interfaces is:

$$E_{interface} = \frac{A_0}{n_{tot}}(\gamma_0 + \gamma_{ads} + U_{interdigit} + \frac{\partial \gamma_0}{\partial \varepsilon_{ip}} \varepsilon_{ip}) \qquad (3.4)$$

$$+ V_0 x_{pvsk} E_B(\varepsilon_{ip}, \varepsilon_{op})$$

where A_0 is the unstrained surface area, V_0 is the unstrained volume of the bulk perovskite unit cell, and n_{tot} is the total number of atoms in one composite formula unit. After parametrization by DFT calculations, we find that the interface formation governed by the above expression is thermodynamically favorable ($E_{interface} < 0$) at all reasonable strain and compositions due to the strongly negative γ_{ads}. This is not surprising since the low-N layered compounds with high interfacial area are readily synthesized, but it does not explain the critical N behavior.

3.4.2 Electrostatic Interactions of Adjacent Interfacial Dipole Layers

Since we are interested in the relative energies between phases with varying perovskite thickness N, this picture of the enthalpy of mixing is incomplete. Along with the overall composition and frequency of interfaces, the main structural feature that varies with N is the distance between two interfaces across the perovskite layer. The formation of surface dipole layers has been studied extensively in ionic perovskites, but less so in hybrid halide perovskites due to the mixed ionic/covalent nature of the bonds and variable stoichiometry at free surfaces. [140–143] Due to the broken Pb-I bonds and the change in the organic cation at the interface, interfacial dipole layers can form and provide a mechanism for the interfaces to interact electrostatically across the perovskite slab. **Figure 3.3a** gives a schematic view of how the combination of the NH_3^+ cation and the undercoordinated I atoms at the organic-inorganic interface can be mapped to a 2D lattice of effective interfacial dipoles with the in-plane periodicity of the BA cations. **Figure 3.3b**

shows the bonding charge density, defined as the difference between the electronic density of the interface and the isolated neutral component atoms, projected along the (001) direction. Red regions indicating localization of electronic density (negative charge) and
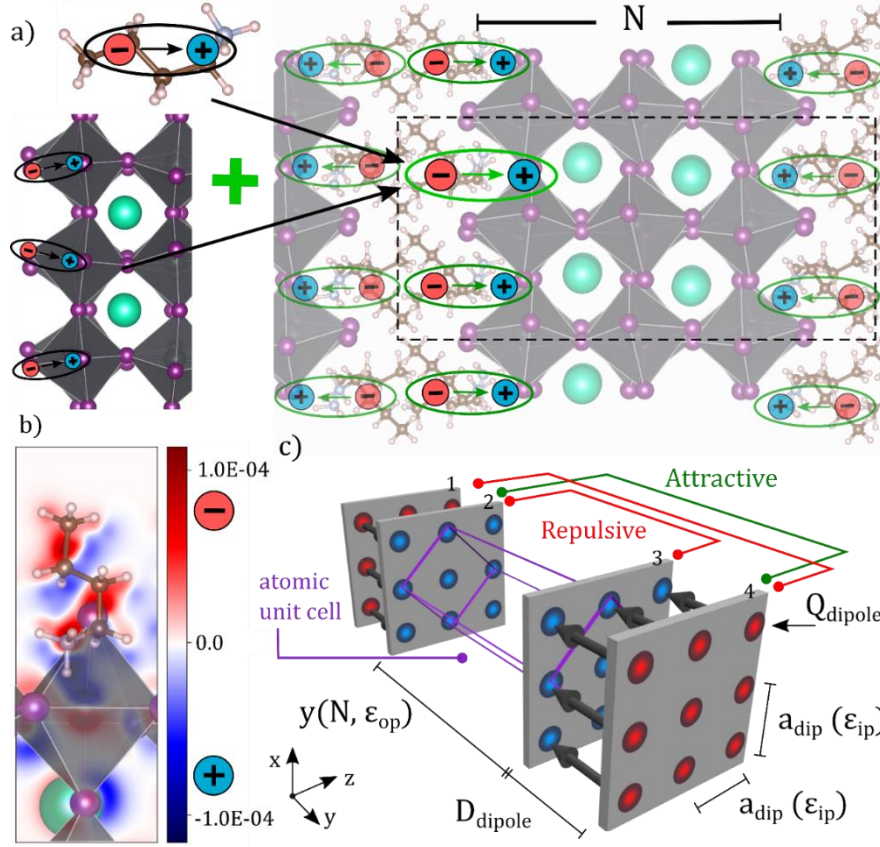
Figure 3.3 a) Atomistic schematic for the formation and alignment of interfacial dipoles. The dipole moment of the BA cation aligns with the I-terminated surface dipole of the perovskite surface (left), which we sum to an effective interfacial dipole (green) perpendicular to the interface. **b)** Bonding electronic charge density of the BA-perovskite adsorbed surface projected along the (001) direction showing significant out-of-plane polarization; units in e/Å^3. **c)** Schematic of the dipole lattice model and the N-dependent electrostatic interaction. The cross-interface distance and the dipole planar lattice constant are coupled to ε_{op} and ε_{ip}, respectively.

blue regions indicating absence of electron density relative to isolated neutral atoms provide a first-principles justification of the out-of-plane polarization localized around the BA molecule. We focus on the interfacial interaction across the perovskite layer since this

distance is N-dependent; while adjacent interfaces are closer together across the organic layer, this interaction length is essentially invariant with N. Furthermore, this interfacial interaction across the organic layer is already incorporated into the vdW interaction energy $U_{interdigit}$ discussed above.

While the electric potential between equally and uniformly charged sheets is zero by superposition, inhomogeneities in the charge density due to the ionic nature of the BA cation groups and the I⁻ atoms leads to corrugations in the potential and a finite contribution to the electrostatic energy. [144,145] To capture the point charge lattice physics, we construct two opposing dipole arrays consisting of 2D square lattices of charged gaussian disks (**Figure 3.3c**) and map the relevant parameters (N, ε_{ip}, ε_{op}) from the A' cation / perovskite mixture model in **Figure 3.2**. We also introduce two parameters, Q_{dipole} and D_{dipole}, which represent the magnitude and distance of the charge separation for each dipole in the lattice; the dipole moment is equal to $Q_{dipole} * D_{dipole}$. The electrostatic energy U_E of a stack of 2D point charge lattices with equal periodicity and overall charge neutrality is given by:

$$U_E = \frac{A}{2\varepsilon_r} \sum_{k_{xz} \neq 0} \sum_{i<j} \frac{\tilde{\sigma}_i(k_x, k_z)^* \tilde{\sigma}_j(k_x, k_z)}{|\vec{k}|} \exp\left(-\left|y_i - y_j\right| |\vec{k}|\right) \qquad (3.5)$$

where the area of each 2D unit cell A and the in-plane reciprocal lattice vectors $\vec{k}$ depend on ε_{ip} and the perpendicular distance between sheets $|y_i - y_j|$ depends on ε_{op} (relationship

51

shown in **Figure 3.3c**; parameter values and details of the derivation in Appendix S3.1).

ε_r is the static permittivity of the medium, [104,146] $\tilde{\sigma}$ are the Fourier coefficients of the real-space charge distribution, and i, j are the integer indexes of the sheets in the stack (Figure S3.1). The static dielectric constant ε_r in MAPbI$_3$ is difficult to measure or calculate but depends on the presence of surfaces and the slab thickness; for simplicity, we choose a global average value of 12 between N = 1 and bulk and ignore any thickness (y) dependence. [146] Explicitly, for the 3 interactions we consider between the dipole sheets $i, j \in \{1,2,3,4\}$:

$$|y_1 - y_3| = Nb_0(1 + \varepsilon_{op}) + D_{dipole}$$

$$|y_2 - y_3| = Nb_0(1 + \varepsilon_{op})$$

$$|y_1 - y_4| = Nb_0(1 + \varepsilon_{op}) + 2D_{dipole}$$

where b_0 is the unstrained lattice constant of the bulk perovskite perpendicular to the (010) surface. Eq. 3.5 shows that the electrostatic energy decays exponentially with the distance between the charge sheets with a characteristic length that depends on the in-plane lattice constant through the reciprocal vector k. The asymptotic behavior interpolates between the limiting cases of uniformly charged sheets ($U_E = 0$) and a single dipole-dipole interaction at long range ($U_E \sim 1/r^3$), consistent with the construction of an infinite series of screened dipole-dipole interactions. The appearance of ε_{ip} and ε_{op} in the exponential couples the energy of electrostatic interfacial interactions with the energy of mechanical interface

relaxation described in **Figure 3.2b**. The relative strain dependence of the electrostatic energy is shown in **Figure 3.4a** over several different reference $|y_i - y_j|$ corresponding to different N-phases from N = 1 to N = 5. A crucial point that emerges is that the direction of the strain dependence opposes that of the interfacial stress relaxation f_{ss}; while the electrostatic cross-interface interaction energy U_E is minimized with compressive in-plane strain and tensile out-of-plane strain, the individual interfacial energy $E_{interface}$ is lowered through tensile in-plane strain and an elastically induced compressive out-of-plane strain.
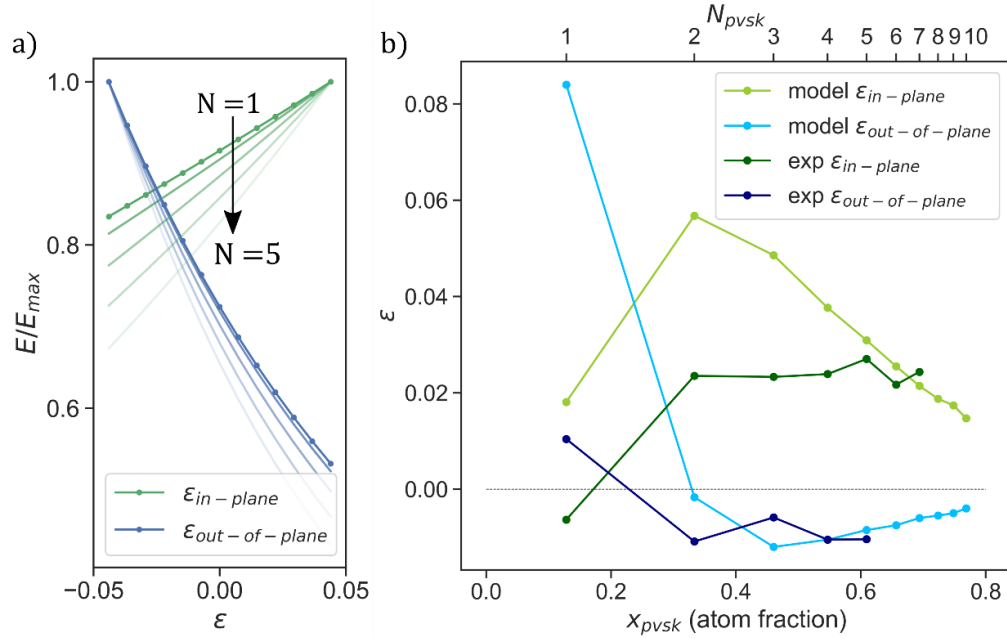
Figure 3.4 a) Strain dependence of the electrostatic dipole energy as a function of N, normalized in terms of the max dipole energy value over the strain window. A 10% strain window corresponds to a ~20% energy change at N = 1 and a ~35% change at N = 5. **b)** Experimental *versus* model strain as a function of N. The model qualitatively captures the non-monotonic behavior of the strain and the switch from N = 1 to 2 from out-of-plane positive (in-plane negative) to out-of-plane negative (in-plane positive) strain.

3.4.3 Minimization of the Free Energy and Determination of N$_{crit}$

The value and strain dependence of the electrostatic term suggests that it will compete with the interfacial mechanical relaxation but quantifying this competition requires minimizing the free energy. Combining all the energetic contributions to the formation of 2D perovskites listed above, we can write down the complete expression for ΔH_{mix} and the total free energy (using the atom fraction conversion $N = \frac{27+7x_{pvsk}}{12(1-x_{pvsk})}$):

$$G_{tot}\left(x_{pvsk}, \varepsilon_{ip}, \varepsilon_{op}\right) \tag{3.6}$$

$$= x_{pvsk}H_0^{MAPbI_3} + (1 - x_{pvsk})H_0^{BAI} + \Delta H_{mix}(x_{pvsk}, \varepsilon_{ip}, \varepsilon_{op})$$

$$\Delta H_{mix} = \frac{A_0}{n_{tot}}(\gamma_0 + \gamma_{ads} + U_{interdigit} + \frac{\partial \gamma_0}{\partial \varepsilon_{ip}}\varepsilon_{ip}) + V_0 x_{pvsk}E_B\left(\varepsilon_{ip}, \varepsilon_{op}\right) \tag{3.7}$$

$$+ \frac{U_E\left(\varepsilon_{ip}, \varepsilon_{op}, N\right)}{n_{tot}}$$

At each composition x_{pvsk}, G_{tot} can be minimized with respect to the internal degrees of freedom ε_{ip} and ε_{op} to find the minimum free energy at each composition $G_{min}(N)$ and construct the phase diagram. Due to the discrete sums in U_E, we minimize this expression numerically, but we note that the primary scaling of the free energy at the minimum strain occurs with composition, as each term of ΔH_{mix} in Eq. (3.7) scales as $\frac{1}{N}$, x_{pvsk}, and $\frac{\exp(-N)}{N}$, respectively. In **Figure 3.4b**, we use the strain values which minimize the free energy at each composition to compare the equilibrium structures predicted by our model with

experimental lattice constants measured at room temperature. [89,90,116,147] Both the experimental and model strains are calculated as deviations from the bulk tetragonal MAPbI$_3$ structure determined by Whitfield *et al*. [129] We find that the model semi-quantitatively captures the non-monotonic trend of the lattice parameters from N = 1 to N = 5. The in-plane strain is determined as the change in area of the (010) plane of the layered structure from the equivalent (101) plane in the bulk reference structure. At N = 1, the interfacial electrostatic interaction dominates the single-interface mechanics and the perovskite lattice experiences in-plane compression and out-of-plane tension. Increasing to N = 2 reverses this effect and the increased distance between the interfaces allows the interfacial mechanics to dictate the structure. The disagreement in the magnitude of the structural distortion for the N = 1 phase stems from an increase of the elastic moduli of the perovskite layer (nanoscale hardening) at N = 1 and a breakdown of the continuum approximation that the single octahedral layer of the N = 1 structure can be accurately modeled by two independent interfaces. This raises the point that while the leading order contributions of the interface elastic energy are captured by $\frac{\partial \gamma_0}{\partial \varepsilon_{ip}}$, a higher order strain term of the form $\frac{1}{2} A E_S \varepsilon^2$ could also be included, where A is the area, E_S are the surface elastic constants, and ε is the strain tensor. [148] This term is second order in strain and therefore small relative to the energy differences between ordered phases at small N, we have dropped this term from the model to simplify the parameter space. Despite this, the dielectric approximation, and the tetragonal symmetry approximation, the salient features

of the structural evolution are captured. This has important effects on the trends of band

gap evolution in these materials. [149]
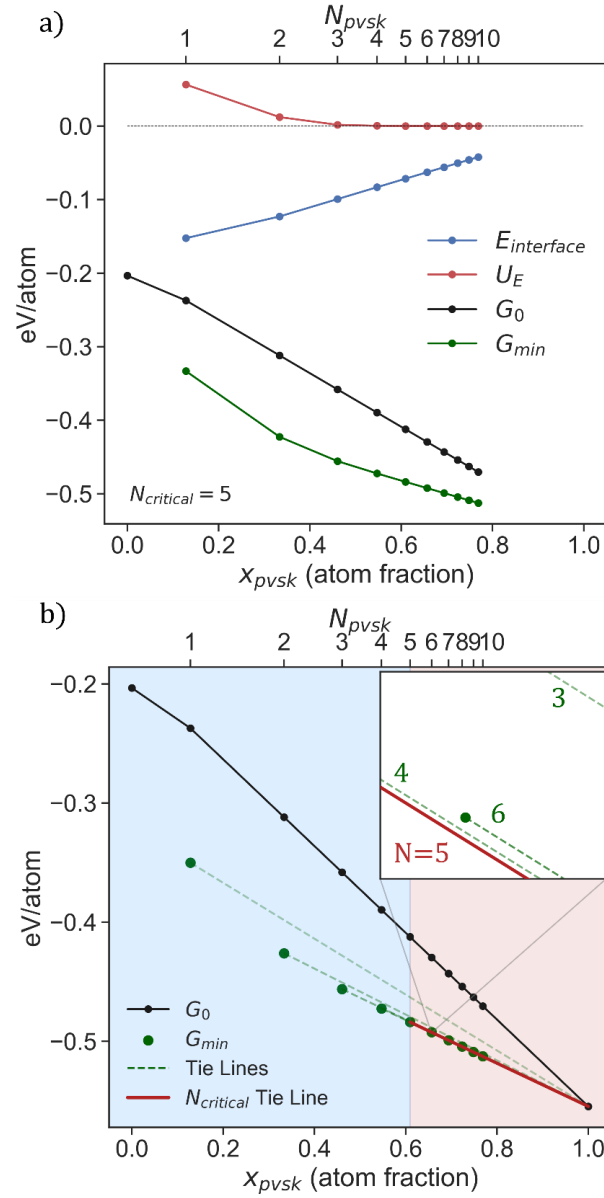
Figure 3.5 a) Component curves for the free energy minimized with respect to strain. The

independent bulk formation energy G_0 (black), interfacial energy $E_{interface}$ (blue), and

electrostatic energy U_E (red) combined to give the minimized energy of the ordered phases G_{min} (green). **b)** Determination of Ncrit using tie lines with the bulk formation energy. Blue region indicates compositions where single ordered phases (green dots) are stable with respect to phase mixing, red region indicates compositions where two-phase separation is thermodynamically preferred.

Having benchmarked the mechanical results of the model with experiment, we now plot the minimum free energy curve as a function of composition to examine the thermodynamic competition between ordered phases at different compositions. Figure 3.5**a** shows how the different components of G_{min} (green) scale with composition x_{pvsk} and N, up to N = 10. Immediately, we see that the repulsive electrostatic energy (red) between the interfaces competes with the energetically favorable surface relaxation (blue) of low-N structures. The nature of this competition is determined by the magnitude of the surface energy and interfacial stress, the elasticity of the octahedral network, and the magnitude of the interfacial dipoles. At low N compositions, the proximity of the interfaces increases the energy of the system, while at high N compositions, the electrostatic interaction decays to zero and the reduction of the interfacial energy through mechanical relaxation takes over. Without the electrostatic terms, the two-phase mixture of highly strained thin (N = 1) phase and non-strained excess bulk (N = ∞) is preferred at all compositions (Figure S3.2) since this two-phase configuration maximizes the number of thermodynamically favorable interfaces while reducing the total bulk elastic energy of the perovskite. The electrostatic repulsion of the interfaces incurs an energy penalty at low N and leads to an inflection point

in G_{min} that corresponds to N$_{crit}$. The strain coupling of these competing mechanisms is necessary to accurately locate this inflection point, which is quite sensitive to the relative magnitudes of the two effects. In **Figure 3.5b**, we zoom in on the total energy curve (green) to extract N$_{crit}$, which is the ordered phase nearest the inflection point of ΔH_{mix}. Specifically, the N$_{crit}$ point is the minimum N composition corresponding to an ordered N phase which is not thermodynamically stable with respect to a two-phase mixture satisfying the composition constraint:

$$G_{min}(N_{crit} + 1) > X_1 G_{min}(N < N_{crit}) + X_2 G_{min}(N > N_{crit}); \; x_{tot} \tag{8}$$

$$= x_{pvsk}^{N_{crit}}$$

where X_1 and X_2 are phase fractions which satisfy the total composition constraint x_{tot}. Graphically, this is visualized by drawing tie lines between different phases on the minimum free energy composition curve; the highest single-phase composition which is not superseded by a tie line between other phases corresponds to N$_{crit}$. This superseding tie line is drawn in red and originates at N = 5 in **Figure 3.5b**, indicating that the model predicts an N$_{crit}$ of 5 in BA$_2$MA$_{N-1}$Pb$_N$I$_{3N+1}$ in agreement with general experimental observations (see Table S2 of Ref. [128]). While the energy differences are small between the different ordered phases on a per-atom basis, over several formula units the thermodynamic driving force becomes significant. The shallow curvature of G_{min} in the region of the inflection point means that the N = 4 and N = 6 phases are close in energy over a range of compositions. This is supported by the synthesis trend in the literature, as observing N = 5

58

and $N > 5$ phases is less frequent and less phase pure over $N = 4$ compounds (see Table S2 of Ref. [128]). This indicates that kinetic freedom (such as hot-casting) during synthesis also plays a significant role in differentiating these compounds. [147]

3.4.4 Interfacial Dipoles Enable Synthetic Control of N_{crit}

The energetic competition between interface formation and cross-interface interaction can lead to critical phase behavior, but we seek to develop a deeper connection between the schematic dipole lattice in **Figure 3.3**, which is constructed of equal and opposite point charges and parametrized by Q_{dipole} and D_{dipole}, and the continuous charge distribution of the atomistic interface. Dipole moments of continuous charge distributions are only well-defined in the presence of a finite surface. [150] The dipole moment of a charge distribution perpendicular to an (010) surface can be calculated as $P_{010} = \int_{y_0}^{b_0}(y - y_0) \cdot \rho(y - y_0)\, dy$, where y_0 is a coordinate reference point inside the charge distribution and b_0 is the length of the supercell perpendicular to the surface. [151] **Figure 3.6a** plots this surface dipole value as a function of the reference point y_0 for the bulk perovskite surface that corresponds crystallographically to the interface that forms in the q-2DPK compounds. The local maxima correspond to the points where y_0 divides $\rho(y)$ into two charge neutral halves, so that the dipole value at these reference points is both physically meaningful and far enough from the surface that it is converged. From this analysis, we find that the surface dipole moment for the perovskite is 1.0 eÅ. Since the BA cation is an overall neutral single molecule with a finite charge distribution in all

dimensions, the dipole moment can be easily found by $P = \int \vec{r} \cdot \rho(\vec{r}) d\vec{r}$, which we calculate to be 0.75 eÅ.

The wide array of possible A' cationic molecules indicates that an ideal strategy to tune the phase behavior of the q-2DPK is through the induced interfacial dipole moment as opposed to the perovskite elasticity. **Figure 3.6b** shows the evolution of N_{crit} as a function of the electrostatic lattice parameters Q_{dipole} and D_{dipole} (**Figure 3.3c**), with the iso-moment contours $P = Q_{dipole} * D_{dipole}$ shown in black. All other model parameters, such as the interfacial energy and interfacial stress, are held constant. First, we find that N_{crit} evolves along the iso-moment contours over independent variations of Q_{dipole} and D_{dipole}, which presents a qualitative affirmation that the dipolar interactions can modify the critical phase behavior. Second, we note that by taking the interfacial dipole moment as a sum of the perovskite surface dipole and the dipole moment of an isolated n-BA cation, we match the dipole moment of ~1.75 eÅ required in the model to observe $N_{crit} = 5$. This simple relation allows for prediction of the N_{crit} value based on the properties of the individual A' cation molecules, which is otherwise difficult to calculate using first-principles calculations due to the numerous degrees of freedom and the difficulty of describing long-range electrostatic interactions using pseudo-potential DFT. The ability to obtain the interfacial dipole as a sum of the independent components can be attributed to the hydrogenic bonding between the organic cations and the lead halide network; if the A' molecule forms covalent bonds with the iodine-rich perovskite surface and significant

60

charge transfer occurs at the interface, this simple design rule may not hold. However, since the interfacial dipole moment is notoriously difficult to calculate or measure directly, this decomposition into readily calculable dipole moments has significant predictive power.
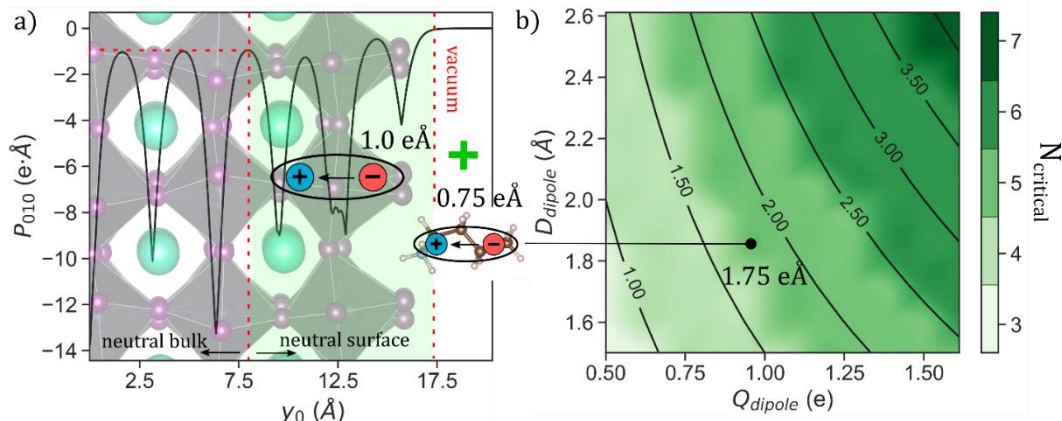
Figure 3.6 a) Determination of the surface dipole moment of MAPbI$_3$ and BA. The local maxima in the dipole moment indicates that the symmetric slab is divided into charge neutral portions, leading to a physically meaningful dipole value. We take the converged value from the interior of the slab. **b)** N$_{crit}$ (green) mapped over the interfacial dipole lattice parameters Q_{dipole} and D_{dipole}, all other parameters held equal. The sum of the surface moment and cation moment fall in the N$_{crit}$ = 5 range for BA$_2$MA$_{N-1}$Pb$_N$I$_{3N+1}$. The N$_{crit}$ changes follow the iso-moment Q*D contours in black, and sensitive changes in the moment induce changes in the N$_{crit}$ value.

The sensitivity of the N$_{crit}$ value to the interfacial dipole moment shows that tuning the interfacial composition can have a substantial impact on the thermodynamically accessible synthesis space of quasi-2D hybrid perovskites. Recently, successful synthesis of an N = 7 q-2DPK with greater phase purity than BA was achieved using 4-AMP (see Table S1 of Ref. [128]) as the A' cation, an organic molecule with two different cationic

groups on each end. [117] Returning to the derivation of U_E, we note that the non-lattice average charge density contributions to the interior electric field from each interface caused a cancellation in the contributions of the electric field scaling as $\frac{1}{y_0}$ with interfacial separation. As characterized, the 4-AMP compound aligns with its neighbors to maximize conjugate ring interactions, breaking the symmetry between the perovskite interfaces and introducing another contribution to the interior electric field. Since our model predicts that increasing the electrostatic energy will shift the critical point to higher N, these molecules with asymmetric cationic groups are highly promising for tunably expanding the q-2DPK into the quasi-bulk, non-excitonic regime. Altering the small A cation may also enable engineering of the critical phase boundary. For example, formamidinium (FA) in place of MA increases the lattice constant of the lead iodide octahedra, [152] increasing the dipole lattice spacing and the internal electrostatic energy. Competing changes may occur to other parameters such as the dielectric constant, so a complete parameter study using our model is warranted to predict the outcome of these chemical substitutions.

3.5 Conclusion

Surveying the synthetic efforts in the fast-growing field of 2D and quasi-2D organic-inorganic halide perovskites, we set out to identify the governing thermodynamic mechanisms of the compositional phase space by considering the free energy of formation of the composite structures. We found that thermodynamically favorable adsorption of large organic molecules onto the I-terminated perovskite surface and interfacial mechanical

62

relaxation drive the formation of internal interfaces to maximize the interfacial area while minimizing the elastic energy penalty. This effect competes with the unfavorable electrostatic interaction between the two opposing perovskite interfacial dipole lattices associated with the adsorbed large organic molecules. The interfacial mechanical relaxation and the electrostatic energy are coupled through the in-plane and out-of-plane strain, which is found to evolve non-monotonically from low-N to high-N phases matching experimental trends. Together, these effects lead to a finite N_{crit}, which corresponds to the minimum loading of A' cations in the $A'_2A_{N-1}M_NX_{3N+1}$ compositional formula to obtain thermodynamically stable single-phases. At $N > N_{crit}$, the system will preferentially phase separate into a mixture of bulk perovskite ($N = \infty$) and $N <= N_{crit}$. We find that N_{crit} can be tuned by reasonable modifications of the interfacial dipole value, and that this complicated quantity can be sufficiently approximated by the sum of the perovskite surface dipole and the dipole moment of the isolated A' cation. Our multiscale, first-principles informed continuum model provides mechanistic understanding and synthetic guidance in the large compositional phase space of quasi-2D perovskites.

Chapter 4 Predicting Surface Strain Effects on Adsorption Energy with Graph Neural Networks

4.1 Background

Structure-property relationships form the core of materials science and rational materials design; understanding how changes in atomic structure change the emergent material properties is a primary goal of computational materials modeling. [153,154] The symmetric elastic strain tensor ε quantifies the change of the material's periodic unit cell of a material from the initial reference state - the bulk ground state crystal structure which minimizes the free energy of formation at zero stress. At a material surface, the disruption of the bulk bonding changes the electron distribution at the surface and induces surface stress, which can be alleviated through shifts in the atomic positions corresponding to a surface strain. [136,137,155] These concepts extend to the rearrangement of surface atoms under a general mechanical force. Surface structural changes can dominate the overall structure-property relationships at the nanoscale, where a significant portion of the atoms in a material are located at or near the surface, and mechanical force can originate from epitaxial mismatch, bending, or other mechanically coupled effects such as piezoelectricity. [156,157] Of the six dimensions used to specify bulk strain (using Voigt notation, ε_{1-6}), surface strains are described by the three deformations in the periodic plane of the surface, but the surface atoms will also relax in the out-of-plane direction where periodicity is broken. Analysis of this continuous 3D surface strain space is typically

limited to single-element structures with low-index surfaces in high-symmetry deformation directions (uniaxial or biaxial) because the search space is vast and low-index surfaces typically form spontaneously under bulk cleavage or epitaxial growth. [158–162]

In small molecule reactions such as ammonia synthesis, carbon dioxide reduction, or nitrogen dioxide reduction, an effective heterogeneous catalyst reduces the energy of transition states in bond-breaking or bond-building reactions, lowering the activation energy barrier and increasing the likelihood that the reaction proceeds in the desired direction. [163] While these energy barriers are often difficult to characterize or predict, the adsorption energy of a molecular structure on a surface describes the interaction strength and has been successfully used as a proxy to describe catalyst activity and assist in catalyst design. [164] Linear scaling relationships identified for adsorption energies of different molecules and across different surfaces reflect the similar bonding configurations of many small molecules on valence *d*-band materials. [165,166] However, these relationships imply that it is difficult to meaningfully improve catalytic activity by simply changing the catalyst material since the relative adsorption energies of molecular intermediates will not change. [167,168] Strain has been suggested as a promising strategy to break these scaling relationships by changing the surface bonding environment, [169,170] and there have been multiple experimental observations indicating that strain can effectively manipulate catalyst-adsorbate interactions and modify catalyst activity across different reactions. [159,161,171–176] This is especially promising given

recent advances in core-shell nanoparticle synthesis and nano-heterostructure synthesis through deposition, allowing for strain control to be achieved in high surface area materials systems which are ideal for catalytic applications. [177–180] By breaking these scaling relations, including strain as a degree of freedom in catalyst design significantly increases the complexity of an already high dimensional space that intrinsically already covers the catalyst structure and composition, the surface facet, the adsorption site, and the adsorbate composition. Nanoparticles frequently contain high-index surfaces which hold significant activity potential but are relatively under-studied compared to conventional metal epitaxial surfaces. [181]

Supervised machine learning (ML) models can learn nonlinear functions in high-dimensional spaces from a relatively small subset of representative training data. The success of ML approaches significantly depends on the combination of the selected model and the featurization of the data, which is the process of preparing and filtering data before it passes into the model. Recently, neural networks using strain tensors as inputs were applied to predict the strain response of the electronic structures of diamond and silicon using a training set of density functional theory (DFT) calculations; equivalent results using DFT alone would have required over 100 million additional calculations, which is several orders of magnitude more than what is achievable with current computational capability. [182,183] These models enable deep elastic strain engineering by learning the relationship between the target property (either band gap or full band structure) and the

strain tensor from a small amount of randomly dispersed training data, covering a region far outside the conventional small-strain linear elastic approximation. However, since the training data concerns only one material, extending these predictions to a new material requires additional training data and a new model. Generating large, accurate, and statistically representative training datasets is a significant bottleneck in applying ML to crystalline materials; [184] recently, the Open Catalyst Project (OCP) released a dataset of over 1.2 million DFT-relaxed catalyst-adsorbate complex structures to model training for adsorption energy prediction with the goal of catalyst discovery and optimization. [30] The dataset spans the critical contributing factors to adsorption energy of bulk composition and structure, surface facet, adsorbate site, and adsorbate composition. Modeling the adsorption energy requires ingesting fine-grained featurizations which contain information about the specific atomic relaxations around the coordination site in an ML model. Graph neural networks (GNNs) are a candidate model class for this problem since they operate on atomic structures-as-graphs, which preserve distance and neighbor information for all the atoms in a structure. Several GNN architectures have been developed and applied to predict molecular and crystalline properties, including the adsorption energy of a handful of molecules on bulk structure bimetallic alloy surfaces. [185–190] While using these models in the physical sciences remains an active research area, the possibility of generalizing over composition and structure degrees of freedom is promising for materials applications.

4.2 Objective

In this work, we synthesize these approaches to investigate the effect of general surface strain engineering on adsorption energies of 27 important small molecule adsorbates over a range of Cu-binary alloy surfaces taken from the OCP dataset. Cu alloys have generated recent broad interest in catalysis due to recent success in identifying high activity Cu-based catalysts for carbon dioxide reduction using a combination of machine-learning and experiments. [191] High-throughput DFT calculations generate a strained training set by randomly applying strains to Cu-alloy catalyst-adsorbate complexes. We find that a DimeNet++ GNN architecture combined with an additional neural network to include strain information succeeds on classification and regression tasks to determine the adsorption energy response to strain. Extrapolating the model to predict the strain response of brand-new surface and adsorbate combinations is more difficult, but our results enable surface strain to be efficiently considered as a continuous engineering parameter in catalyst design.

4.3 Methods

4.3.1 High throughput DFT calculations

First-principles DFT simulations were carried out using the Vienna *ab initio* simulation package (VASP). [20,21] Projector-augmented wave pseudopotentials [132] are used with a cutoff energy of 400 eV for plane-wave expansions. [16] The exchange-correlation is treated using the Perdew-Burke-Ernzerhof (PBE) generalized gradient

approximations. The atomistic structures of catalyst and catalyst + adsorbate slabs were relaxed using Γ-centered k-point meshes of $40/a$ x $40/b$ x 1 rounded to the nearest integer, where a and b are the lattice constants of the slab supercell. For structural relaxations, the atomic positions of all unit and supercells are optimized until the force components on each atom are less than 0.03 eV/ Å, and the electronic energy is converged within 10^{-4} eV. A vacuum spacing of 20 Å was added to slab calculations to prevent interactions between periodic images. Following the Open Catalyst Project dataset generation, atoms further than 2 Å from the surface are fixed in their relaxed bulk positions during slab relaxation to simulate the bulk lattice structure, while surface and adsorbate atoms are free to relax. [30] Long range van der Waals dispersion interactions were treated using the DFT-D3 method developed by Grimme *et. al.* [133,134]; these corrections are not part of the original Open Catalyst calculation parameters but we found that including them changed the distribution of adsorption energies. Individual molecules are relaxed in a 12 Å cubic unit cell using the same calculation parameters.

4.3.2 Dataset Preparation and Curation

Zero-strain structures are converted to graphs for model input using the same graph generation procedure as the Open Catalyst Project. Atoms are nodes, edges are labeled with the distance between two atoms, and the neighbor distances are calculated taking periodic boundary conditions into account. The number of neighbors for each atom is capped at 60 and the cutoff radius for a neighbor interaction is 7Å. [30] Subsurface, surface, and

adsorbate atom tags are included in the dataset to be used for node-level regularization. For data normalization, the input strain tensors and all energies are normalized to zero-mean, unit standard deviation before model training; the normalization parameters are calculated independently for ε_1, ε_2, ε_6, and ΔE_{ads}.

4.3.3 Model Training and Hyperparameter Optimization

Schnet, CGCNN, and DimeNet++ architectures were all tested for the classification and regression tasks; DimeNet++ significantly outperformed the other model architectures. All models are implemented using the PyTorch framework. Hyperparameter optimization was performed for all model parameters and training procedures on the classification task using an Async Successive Halving Algorithm (ASHA) implemented in the Ray software package. The final model hyperparameters are included in Table S4.4. To prevent overfitting, the model size was reduced until the training loss and the validation loss were similar. Train, validation, and test splits were randomly generated using 80%, 10%, and 10% of the total dataset. All model training and dataset generation code is publicly available here.

4.4 Results

4.4.1 Dataset Generation and Machine Learning Workflow

For a particular catalyst-adsorbate complex structure (**Figure 4.1a** Cat + Ads), we will specify the compositions of the catalyst and the adsorbate as well as the surface face

with the shorthand $X(hkl)$: $^*Y$, where X is the surface composition, hkl are the Miller indices of the surface facet, and $^*Y$ is the adsorbate with $*$ specifying the initial adsorbing atom. $X(hkl)_\varepsilon$ will be used to denote a strained catalyst. The adsorption energy E_{ads} is defined as the difference between the energy of the catalyst-adsorbate complex and the individual, separated catalyst (Cat) and adsorbate (Ads, **Figure 4.1a**). In a vacuum, E_{ads} depends on the structure and composition of the surface, the structure and composition of the molecule, and the coordination site (location on the surface where the molecule interacts). The strained adsorption energy E_{ads}^ε is similarly defined as the difference between the adsorbate-strained surface complex $X(hkl)_\varepsilon$: $^*Y$ and the individual strained surface $X(hkl)_\varepsilon$ and adsorbate. We seek to predict the change in adsorption energy $\Delta E_{ads}(\varepsilon) = E_{ads}^\varepsilon - E_{ads}$ of an adsorbate on a surface due to a rotation-free applied strain in the plane of the surface described by the strain tensor ε, with uniaxial components ε_{11} (ε_1) and ε_{22} (ε_2) and shear component ε_{12} (ε_6). The sign and magnitude of ΔE_{ads} has been
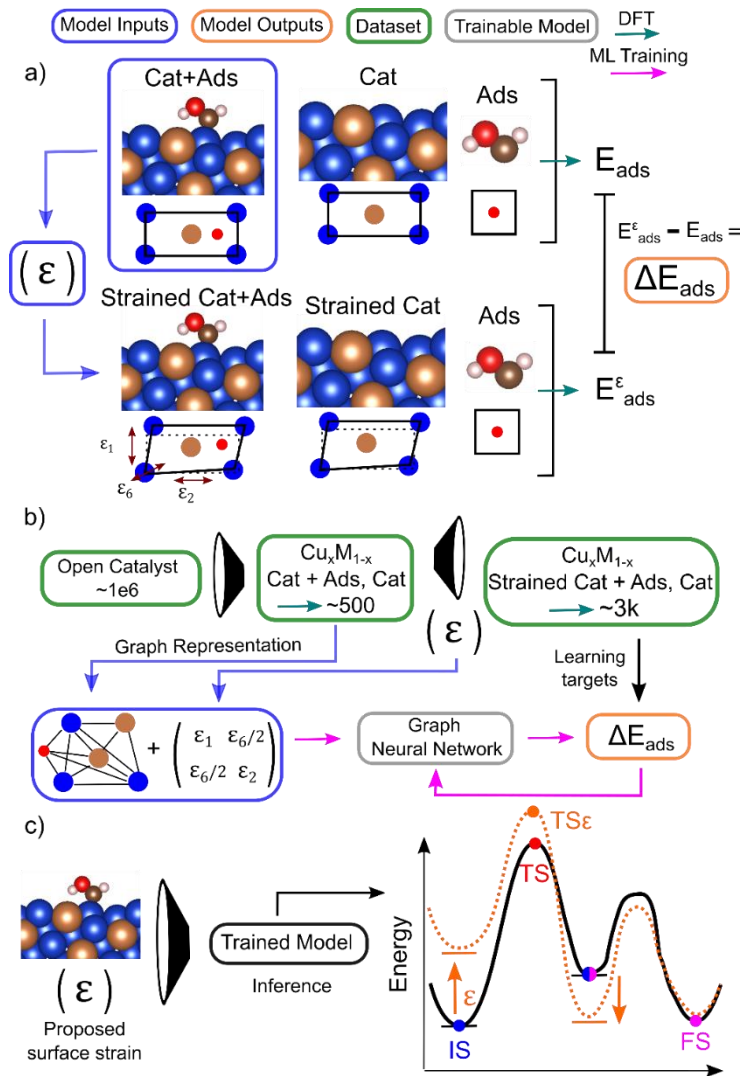
Figure 4.1 a) Atomistic overview of the structures used to calculate the change in adsorption energy with surface strain. **b)** Workflow for dataset curation, assembly, and model training. Random strains are generated for each alloy catalyst and ΔE_{ads} is calculated to form the targets for the training set. **c)** After successful model training, inference is performed over strain space and surface-adsorbate combinations. The adsorption energy of initial states (IS), transition states (TS), and final states (FS) can shift in opposite directions, fundamentally changing reaction energy barriers.

shown to depend on the surface composition, facet, molecule, and nature of the

deformation even in relatively simple systems such as $Pt(111)_\varepsilon : N$. [169,192]

The dataset development and model training workflow are summarized in **Figure 4.1b**. To develop a model to approximate $\Delta E_{ads}(\varepsilon)$, we assemble a training dataset of strained Cat + Ads complexes using first-principles density functional theory (DFT) calculations, using the public OCP dataset as a starting point (**Figure 4.1b**). [30] Recently, a number of copper alloy surfaces were identified to be high activity catalysts in CO_2 reduction based on their combined adsorption energies for *H and *CO. [191,193] Building on these results, we extract a compositional subset of the OCP dataset consisting of binary copper alloy catalysts (Cu_xM_{1-x}, where M is an alloying element) and 27 adsorbates to be the sandbox for our strain investigation. A list of catalyst alloy elements and adsorbates in the training dataset is given in Table S4.1 in Appendix S4.1. For each Cat + Ads complex in the filtered dataset, 6 strain tensors were generated by selecting uniform random values for ε_1, ε_2, and $2\varepsilon_6$ between -3% and 3%. The bulk lattice structure (no strain applied) was also included for each Cat + Ads complex to provide E_{ads}. Each random strain tensor was applied to both the Cat structure and the Cat + Ads complex, generating a pair of structures which were relaxed to enable calculation of E_{ads}^ε. Taking the difference between E_{ads}^ε and E_{ads} gives the final training labels ΔE_{ads}. The original OCP catalyst-adsorbate supercells are large enough to minimize multi-adsorbate interactions across the periodic boundary conditions of the unit cell. [30] 6 strains were chosen to keep the energy calculations computationally tractable while including a diverse

73

set of surfaces and molecules; random sampling was selected to generate a uniform distribution of strain orientations relative to the randomly distributed orientations of the adsorbate coordinate environments. The inputs to the machine learning model training are the relaxed zero-strain Cat + Ads structure represented as a graph and the strain tensor, and the output is the change in adsorption energy after strain and relaxation. Therefore, only one Cat + Ads structure relaxed at the bulk lattice parameters is required to make predictions about the adsorption energy response across three-dimensional surface strain space. Further discussion of the model architecture choices is presented in Section 4.4.3. With a successfully trained model, this strain space can be efficiently explored across different catalyst-adsorbate systems to engineer reaction energy diagrams (**Figure 4.1c**). For comparison, evaluating the adsorption energy with 0.5% resolution in the 3D strain space of -3% to 3% over ε_1, ε_2, and ε_6 would require 2200 grid points in strain space for each catalyst-adsorbate complex and over 6.5 million total structures. Using our calculation cost for training data generation of ~18 hours per pair of Cat and Cat + Ads structures, this effort would consume 72,000 cpu-years of DFT calculations vs. 120 combined cpu/gpu-hours required to train our model.

4.4.2 Distribution of Adsorption Strain Response over Composition

After the high-throughput DFT dataset generation, we inspect the resulting distribution of ΔE_{ads} to evaluate whether machine learning is required. The distribution of $|\Delta E_{ads}|$ values in the training set, excluding the zero-strain state, is plotted against several

74

degrees of freedom in **Figure 4.2**. **Figure 4.2a** plots the magnitude of ΔE_{ads} as a function of total areal strain magnitude $\frac{A-A_0}{A_0}$ and the ratio of the shear to uniaxial components $\frac{2|\varepsilon_6|}{|\varepsilon_1+\varepsilon_2|}$ (color scale). **Figure 4.2b** plots the magnitude of ΔE_{ads} as a function of the directional strain anisotropy $\frac{|\varepsilon_1+\varepsilon_6|}{|\varepsilon_2+\varepsilon_6|}$ and the Cu-content of the catalyst composition (color scale). The red line on each plot illustrates the energy of kT at 300K (25 meV) for reference on the log scale. Just over half of the applied strains result in essentially no change to the adsorption energy, falling below 25 meV. However, the rest of the applied strains cause an appreciable change in the adsorption energy, including a significant band between 20 and 150 meV. Across the dataset, there is no discernible trend for ΔE_{ads} over the strain magnitude, strain character, or catalyst alloy composition. **Figure 4.2c** and **Figure 4.2d** zoom into the compositional representation in the dataset, plotting the value of ΔE_{ads} against the alloying element in **Figure 4.2c** and the adsorbate in **Figure 4.2d**. The color scale indicates the relative representation of each composition in the dataset; for example, Cu-Al is the most common composition in the dataset, and NH is the most common molecule. The composition imbalances are a function of the random distribution of surfaces and molecules in the original OCP dataset used as the starting point for generating the strained dataset. When plotting ΔE_{ads} at this finer compositional resolution, there are no standout compositions or adsorbates which are especially sensitive to strain over the others.

75

Altogether, the distribution of the training dataset supports the hypothesis that machine learning could be useful since there is no obvious trend in ΔE_{ads} generally across several
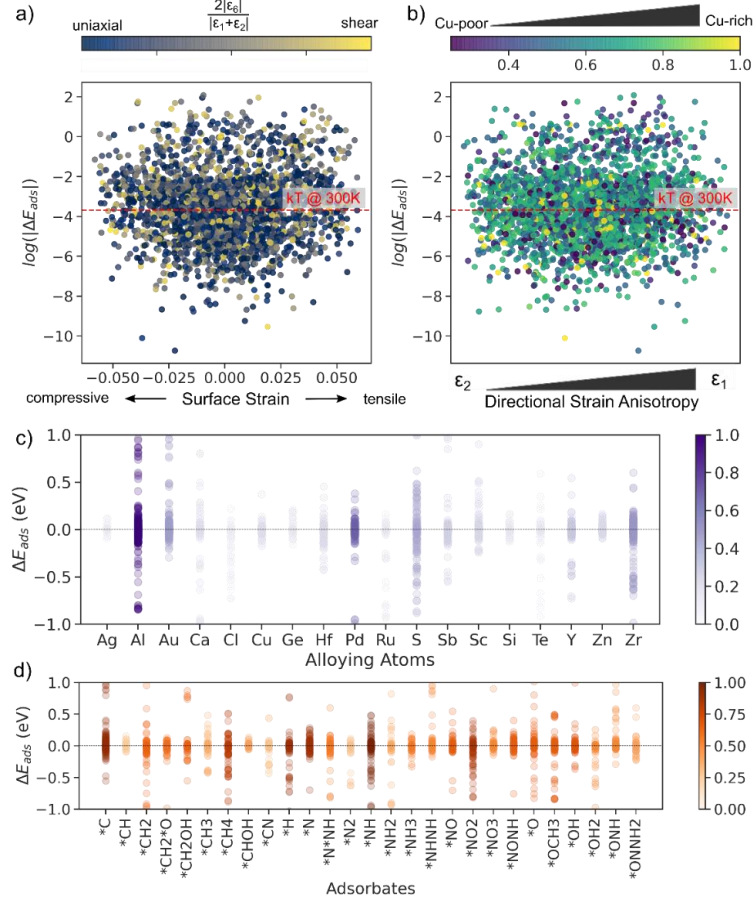
Figure 4.2 a) Log magnitude of adsorption energy change ($\log|\Delta E_{ads}|$) as a function of the total areal strain (x-axis) and the shear magnitude / uniaxial magnitude ratio (color scale). **b)** $\log|\Delta E_{ads}|$ as a function of directional strain anisotropy $|\varepsilon_1 + \varepsilon_6|/|\varepsilon_2 + \varepsilon_6|$ (x-axis) and the Cu content of the catalyst (color scale). **c)** ΔE_{ads} grouped by non-Cu catalyst alloy element (Cu indicates pure Cu catalyst). Darker points indicate greater relative representation; Cu_xAl_{1-x} is the most represented catalyst alloy while Cu_xAg_{1-x} is the least. **d)** ΔE_{ads} grouped by adsorbate; * indicates initial adsorbing atoms. Darker points indicate greater relative representation; *NH is the most represented while *CH is least represented. catalyst and adsorbate degrees of freedom that a simpler physics-based model can capture.

Next, we evaluate the data distribution to construct classification and regression tasks for our model. The target ΔE_{ads} distribution first shown in **Figure 4.2** is plotted altogether as a histogram in **Figure 4.3a** and **Figure 4.3b**, where **Figure 4.3b** zooms into the central histogram bar in **Figure 4.3a**. Overall, the data distribution contains two long tails on both the positive and negative side which span several orders of magnitude, and there is a high concentration of values near zero corresponding to essentially no strain effect. For catalyst design by strain engineering, we are primarily interested in determining if a strain will significantly increase, decrease, or have no effect on the adsorption energy of a particular adsorbate. Therefore, we bin the dataset into 3 categories: $\Delta E_{ads} < -25$ meV (class $-\Delta$, blue), $|\Delta E_{ads}| < 25$ meV (class Z, gray), and $\Delta E_{ads} > 25$ meV (class $+\Delta$, pink) to define a classification task for our model; 25 meV ($k_B T$ evaluated at T = 300K) is chosen as the threshold to classify a significant strain response, and class Z is short for *zero effect*. We verify that each of these classes contains a representative distribution of the different Cat + Ads structures; **Figure 4.3c** shows the histogram of the fraction of member training examples which originate from a particular Cat + Ads complex in each class. For example, consider the Cu$_3$Sb (210):*CHOH complex shown in **Figure 4.1a**. If we apply four random surface strains (**Figure 4.3d**) to this structure, and two of them result in $\Delta E_{ads} < -25$ meV (**Figure 4.3e**), they will contribute to the 0.4 bar of the $-\Delta$ histogram in Figure 3c. Likewise, strains with $\Delta E_{ads} > 25$ meV contribute to the $+\Delta$ histogram, and $|\Delta E_{ads}| < 25$ meV strains (including all ground state structures and identity matrix strains by definition) contribute to Z. From these histograms, we conclude that most Cat + Ads

77

complexes appear in multiple classes; therefore, accurate classification cannot be achieved on structural or compositional information alone. Only Z contains some complexes with 100% membership, and this is reasonable since we expect that certain Cat + Ads complexes will be relatively immune to surface strain. The total class splits in the training set are given in Table S4.2. The class distribution analysis confirms that classifying the strain response into broad buckets still requires both the structure and the specific strain pattern to successfully predict. For the regression task, we simply normalize the target ΔE_{ads} distribution to zero mean and unit standard deviation and calculate the mean absolute error (MAE) of the predicted values against the true values.

To establish a performance baseline and further justify additional model complexity, we test an ensemble linear baseline model by fitting a separate linear regression to each unique group of catalyst alloy-element and adsorbate in the training data (80% of the dataset) and used to predict the class of any matching alloy-element + adsorbate structures in the test data (10% withheld). We ask the baseline model to do some generalization over the specific catalyst composition structure since this is potential feature of the GNN which can add significant predictive capability. **Figure 4.3e** gives the normalized confusion matrix for this baseline classifier, which shows the fraction of true samples predicted to fall in each class by the model; each row sums to 1 and the correct model predictions appear along the matrix diagonal. This model performs better than random guessing but still misidentifies the class of ~45% of the test data, with an F1 score
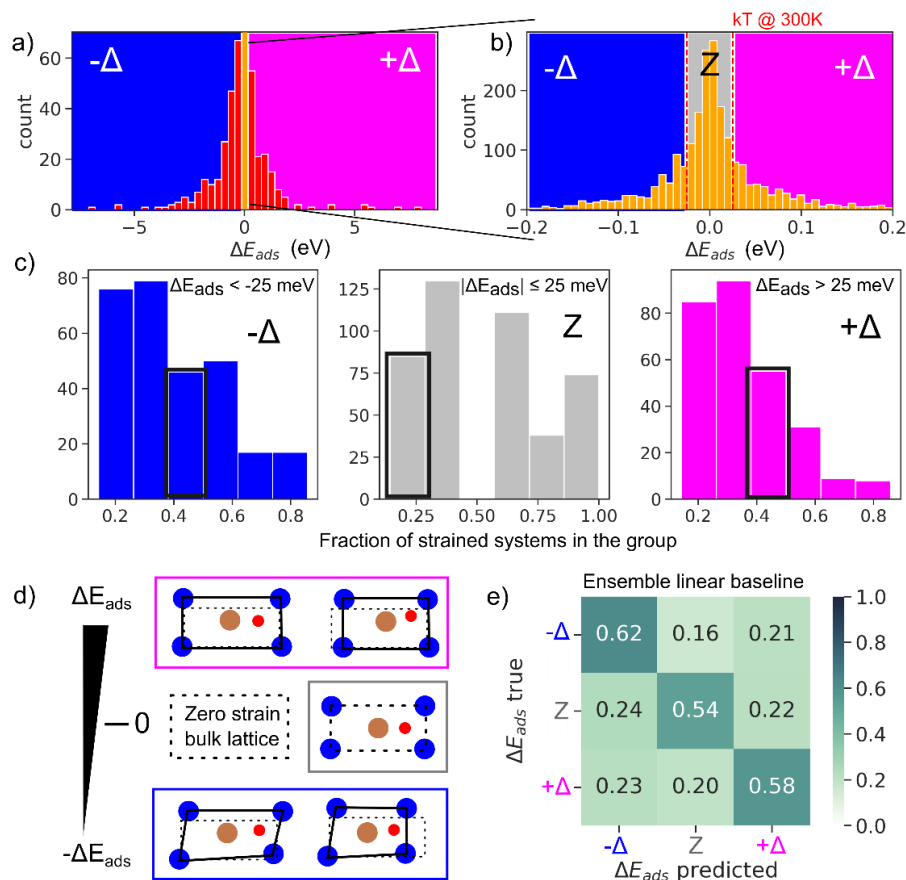
Figure 4.3 a) Total histogram and **b)** zoomed histogram of ΔE_{ads} in the training dataset and assigned classes. Class $-\Delta$ (ΔE_{ads} < -25 meV) is blue, class Z ($|\Delta E_{ads}|$ < 25 meV) is gray, class $+\Delta$ (ΔE_{ads} > 25 meV) is pink. **c)** Histograms of fractional class membership grouped by Cat + Ads structure show even distribution of Cat + Ads structures across the three assigned classes. **d)** Example of histogram generation; of 5 hypothetical strains for Cu₃Sb:*CHOH, 2 fall in $-\Delta$, 1 falls in Z, and 2 fall in $+\Delta$ (highlighted histogram bars in **c**). **e)** Confusion matrix for the ensemble linear regression baseline model on test data.

of 0.58 for the classification task. The average MAE across each ensemble linear model

for the regression task is 0.17 eV, above the typical threshold in catalysis of 0.1 eV.

Additional classification and regression metrics for the ensemble linear baseline are given

in Table S4.3. Since neither the classification nor regression performance from the baseline is sufficient to be practically useful, we proceed to training and testing graph neural network hypothesis.

4.4.3 Model Architecture, Training, and Performance

From the training set analysis, we recognize that we need a model which can generalize over both structural and compositional degrees of freedom. GNNs are a promising candidate for this application since differentiating the strain response across different surfaces and molecules requires incorporating detailed structural information into the input. We adapted and modified the DimeNet++ model architecture, first introduced by Klicpera et. al and used in the Open Catalyst challenge to predict adsorption energies from initial structure. [30,187,188] The model architecture is shown in **Figure 4.4a**. The graph represents atoms as nodes and the interactions between atomic pairs as edges within a cutoff radius, chosen to be 7 Å with a maximum of 60 nearest neighbors (based on original hyperparameters in the Open Catalyst Dataset). [30] The network embeds each node (atom) of the graph as a set of directional pair-wise interactions, and the edges are embedded using a set of spherical basis functions which incorporate bond angle information. The basis set choice and embedding strategy provides rotational invariance to the model; more details are available in Refs. [187,188]. After the graph representation of the Cat + Ads complex is passed through the standard DimeNet++ model, we pad the node

level output with zeros to the size of the largest structure in the dataset and append the normalized strain tensor, injecting the second component of the input data. This combination of the DimeNet++ output and the strain tensor is finally passed through a small fully connected neural network before the output is summed to give the final prediction.

The strain architecture design is physically motivated by a perturbation approach; first, the graph model develops an internal representation of the relaxed Cat + Ads structure at the bulk lattice parameters across compositional and structural degrees of freedom. This output is then passed through a perturbation filter (StrainBlock) which ingests the strain tensor and aims to update the Cat + Ads structure output to match the target ΔE_{ads} corresponding to the Strained Cat + Ads structure (**Figure 4.1a**). The perturbation approach builds prior physical knowledge into the machine learning model and helps circumvent several practical constraints. First, we enforce that the graph weights only operate on information originating from the bulk lattice Cat + Ads structure with zero strain, which incorporates our assumption that the surface and adsorbate composition and structure are dominant variables in determining ΔE_{ads}. This makes the network more physically interpretable since the intermediate output of the GNN before the StrainBlock will be identical for any particular Strained Cat + Ads complex. Second, physical intuition indicates that a significant portion of the nonlinear ΔE_{ads} response is due to structural change within the adsorbate. We expect that the overall strained surface structure is

relatively similar before and after straining. Had we instead used the strained, unrelaxed structure as the inputs to DimeNet++, we would be introducing large amounts of variance in regions of the input data which we don't anticipate being physically significant, while the adsorbate structure would be largely unaffected by an applied strain without relaxation. In addition, a strained but unrelaxed graph would introduce significant variation to portions of the bulk graph far from the adsorbate, which is unlikely to affect the target adsorption energy change since it is mirrored in the strained Cat-only structure; when ΔE_{ads} is calculated, these bulk contributions to the adsorption energy are subtracted out.

Despite these hypothesized benefits, using the strain tensor directly introduce some complications around the choice of coordinate system. Rotation and inversion invariance of DimeNet++ is a key feature in its successful property prediction for atomistic systems. [187,188] The model is periodicity aware by the graph construction, which considers atoms in neighboring periodic unit cells as neighbors, but the graph does not contain any information about the unit cell itself. Meanwhile, the strain tensor is in the lattice coordinate system, so appending the strain data to the DimeNet++ output and passing it through the StrainBlock assumes a particular choice about the unit cell. For example, the same deformation leading to a particular ΔE_{ads} will be represented as a different strain tensor in a hexagonal coordinate system and an orthorhombic coordinate system, but the graph structures in DimeNet++ will only differ by the size of the graph / # of atoms in the unit cell. Given that our Cat + Ads complexes are large supercells which

contain very few symmetries, we think it is unlikely that alternate supercells coordinates with different symmetries would be practically used, but we standardize our structure dataset by ensuring that the primitive supercell is used and the c-axis is concurrent with the normal to the periodic a-b surface plane. To recover coordinate symmetry and remove bias for a particular choice of coordination system, we pursue a data augmentation strategy and duplicate each entry in the dataset by swapping the a- and b-coordinates in both the structure and the strain tensor. This removes any bias in the model for a left-handed or right-handed coordinate system, effectively embedding additional physical knowledge into the model and doubling the size of the training set. This method was simpler to implement
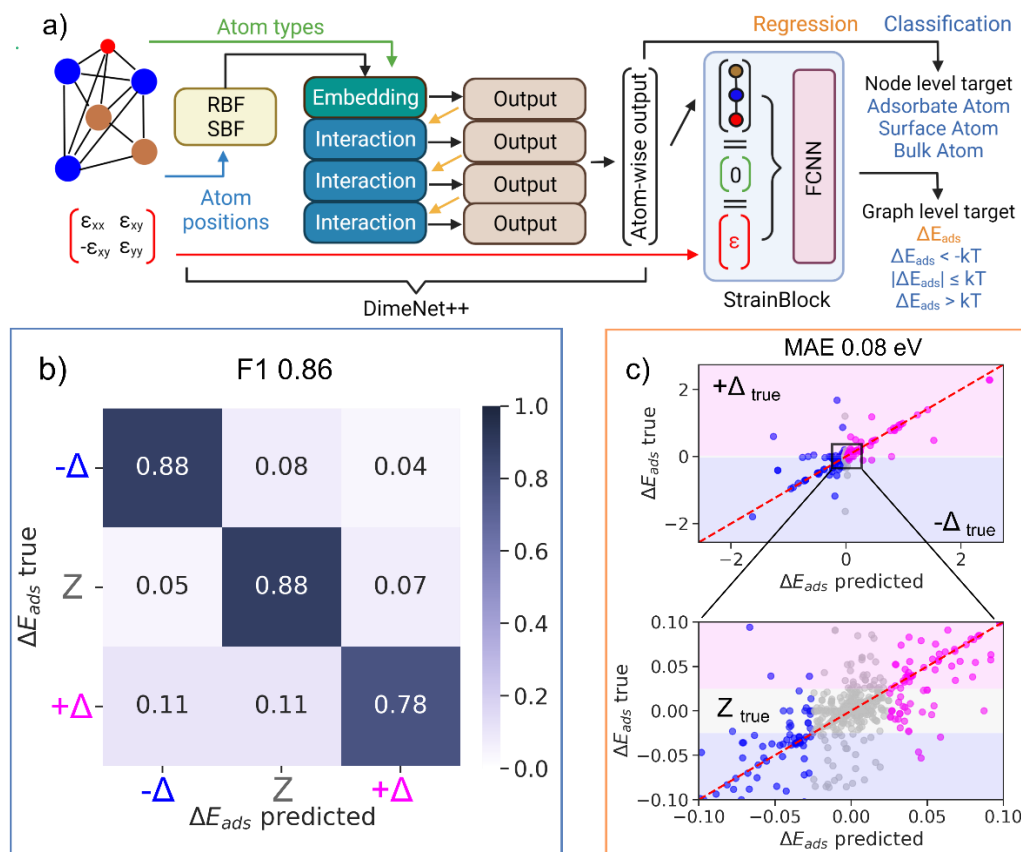
Figure 4.4 a) Model architecture used for classification and regression tasks. The relaxed zero-strain Cat + Ads structure is input to DimeNet++. The strain tensor is appended to the padded DimeNet++ output and passed through a fully connected neural network (StrainBlock). Regularization is performed on node-level output by classifying nodes as adsorbate, surface, or bulk. ΔE_{ads} classification and regression are graph-level tasks. **b)** Normalized confusion matrix for the GNN + strain model on test data. Significant improvement is observed across all categories compared to the linear baseline in **Figure 4.3**. **c)** Results from the GNN regression task, zoomed in bottom. Graph background colors give the true class while point colors give the predicted class based on the regression.

than constraining the model weights in the first layer of the StrainBlock to respect the coordinate symmetry and/or transforming the strain tensor into an equivariant representation; furthermore, data augmentation has been shown to be a highly effective strategy for improving classification accuracy in other deep learning contexts. [194] Development of a unique deformation basis for graph structures, or incorporating explicit periodic boundary conditions into graph representations to embed information about the coordinate system, is reserved for future work.

Choosing how to incorporate the strain input data into the model highlights a challenge of working with low symmetry catalyst-adsorbate or defect structures in machine learning. While the graph representation affords a general capability to represent structural information that cannot be achieved in discrete featurization, it becomes difficult to capture effects in local regions of the graph such as strain fields caused by dilute defect or adsorbate concentrations. [195] For example, an average Cat + Ads complex in the dataset contains 73 atoms. Of these, on average 20 atoms are within a few Angstroms of the surface and

allowed to relax in the DFT calculations away from the bulk structure, and only ~3 will be part of the adsorbate itself. This means that while the whole structure provides necessary information about broad physical context (composition, symmetry, surface relaxation), the region of the graph containing the perturbation (in our case, the adsorbate) that we expect to dominate the target response can be drowned out. We pursued two strategies to mitigate this challenge, which is an active area of GNN research. [195,196] The first strategy is to simply reduce the input data by cutting out bulk-like atoms from the graph representation. We found that this reduced model performance, likely due to the absence of broader contextual information about the material structure. The second strategy is to implement regularization in the loss function which incentivizes the model to differentiate between bulk, surface, and adsorbate atoms, which was implemented by introducing a node classification task to the model in addition to the primary ΔE_{ads} prediction task. This regularization allows incorporation of additional physical prior knowledge about regions of the graph in between node-level and graph-level and is conceptually similar to node-level property predictions [196], but to our knowledge has not been implemented for surface adsorbate complexes. DimeNet++ output blocks were modified to give additional outputs for node classification, and the cross-entropy loss was calculated after node classification as bulk, surface, or adsorbate. This loss was added to the primary ΔE_{ads} target loss, incentivizing the same model weights to give correct node classification and adsorption energy prediction. We found that this slightly improved model performance predicting ΔE_{ads} over non-regularized, single task training, and that the model was

extremely successful at identifying the correct atom identifications (>98%) in testing. A caveat to this result is that the filtered OCP dataset we selected happened to contain no overlap between elements in the slab and elements in the adsorbates; only oxygen appears as both a slab element and an adsorbate element. Therefore, identifying the adsorbate atoms can be achieved with the element label. The regularization still successfully separates surface atoms from bulk atoms, and we believe that this regularization strategy could provide greater benefit in a larger and more compositionally diverse datasets with elemental overlap between adsorbates and surfaces (such as oxides). Another strategy to consider would be a hierarchical ensemble model strategy, where a different GNN is trained on each subset class of atoms in the structure (full structure, surface atoms + adsorbate, adsorbate + nearest neighbor) and the outputs are considered together to form the final ΔE_{ads} prediction.

The performance metrics for the GNN classifier and the GNN regressor on withheld test data after training are summarized in **Figure 4.4b** and **Figure 4.4c**. As in **Figure 4.3e**, the normalized confusion matrix in **Figure 4.4b** gives the fraction of true samples in the test data which were predicted to fall in each class by the classifier; each row sums to 1 and the correct model predictions appear along the matrix diagonal. On the same set of training and testing data as the linear baseline, the GNN+Strain classifier outperforms the ensemble linear baseline by at least 20% in every category. Additionally, the error rate misidentifying $-\Delta$ and $+\Delta$ classes (thereby confusing a large positive (negative) ΔE_{ads}

86

with a large negative (positive) ΔE_{ads}) is on average one-third of the same linear baseline

error, and this is the costliest error to make when evaluating the impact of strain on a

reaction diagram. The regression results are shown over the full test dataset in **Figure 4.4c**

top (zoomed in **Figure 4.4c** bottom); the mean absolute error for the regression model is

0.08 eV, which is within the target range for machine learning approximators in

catalysis. [30] The points are colored according to the class predicted by the regressor, such

that any points in a shaded region of a different color indicate a misclassification by the

regression model, while matching points indicate a success. Not surprisingly, this model

has more difficulty distinguishing positive and negative ΔE_{ads} near the MAE, which is

where many of the samples lie. Overall, the regularized model architecture (detailed in

Table S4.4) performs well on both the classification and regression tasks. Supplied with a

larger training dataset, performance may further improve if these tasks are combined, for

example training a separate regressor model within each predicted class. Model

performance decreased when the test data was constructed of new Cat + Ads compositions

completely unseen in the training data; this type of extrapolation is a goal for the field of

physical GNNs but requires larger datasets than the one generated in this work.

4.4.4 Model Inference Identifies Alloy Compositions Suitable for Surface Strain Engineering

Recall that the dataset used for training and testing the model contained 6 random

strains for each Cat + Ads structure plus an additional zero-strain structure matching the

bulk lattice constants. Considering the inclusive 3D strain space between -3% to 3% at 0.5% resolution requires 13 grid points in each direction, or 2197 total DFT calculations per Cat + Ads structure), this training set covers 0.3% of the total strain space for each Cat + Ads structure. For inference, we generate 500 random strains in this 3D strain space (22% of the total space at the same grid resolution) for each Cat + Ads structure in the dataset (445,000 total strain + structure combinations) and use the trained classifier model to predict the category for ΔE_{ads} for each strain. Inference across all points in the dataset takes ~6 hours on 1 GPU; comparable DFT calculations would require over 18,000 cpu-years of computational effort.

The ammonia synthesis reaction $N_2 + 3H_2 \rightarrow 2NH_3$ is one of the most important industrial chemical reactions in the world and one of the most highly studied in catalysis. [197] The overall reaction is exergonic but on many catalysts the overall reaction pathway begins as exergonic and ends as endergonic due to the presence of stable adsorbed intermediates. [198,199] The rate determining step of the most-studied dissociative pathway in Haber-Bosch conditions can be one of several intermediate steps including dissociation of N_2 and various $H + NH_x \rightarrow NH_{x+1}$ steps depending on the catalyst and the catalytic environment. A general guiding principle towards improving ammonia synthesis catalyst performance is reducing the cumulative magnitude of the endergonic steps within the reaction pathway. [199–201] Cu-based catalysts have been a recent focus of electrocatalytic nitrogen and nitrate reduction studies, which introduces the additional

complexity of competing reactions such as hydrogen evolution. [202–204] While many features of the reaction conditions ultimately contribute to the ammonia synthesis rate, the adsorption energy describes the foundational interaction between the catalyst and relevant intermediates from which further microkinetic analysis can be conducted. We choose the intermediate reaction $^*H + {}^*N \rightarrow {}^*NH$ as an illustrative example for identifying catalyst candidates with high strain engineering potential. **Figure 4.5a** plots an average of the ground state energy of the reactants *H + *N (black lines) and product *NH (red lines) grouped by catalyst alloy composition. This gives an indication of the relative adsorption energies between surface compositions in the strain free case. All the intermediate energies are exergonic relative to the formation energies of both N_2 and NH_3, so raising the adsorption energy of these three intermediates will reduce the gross endergonic energy of the dissociative mechanism. [205]
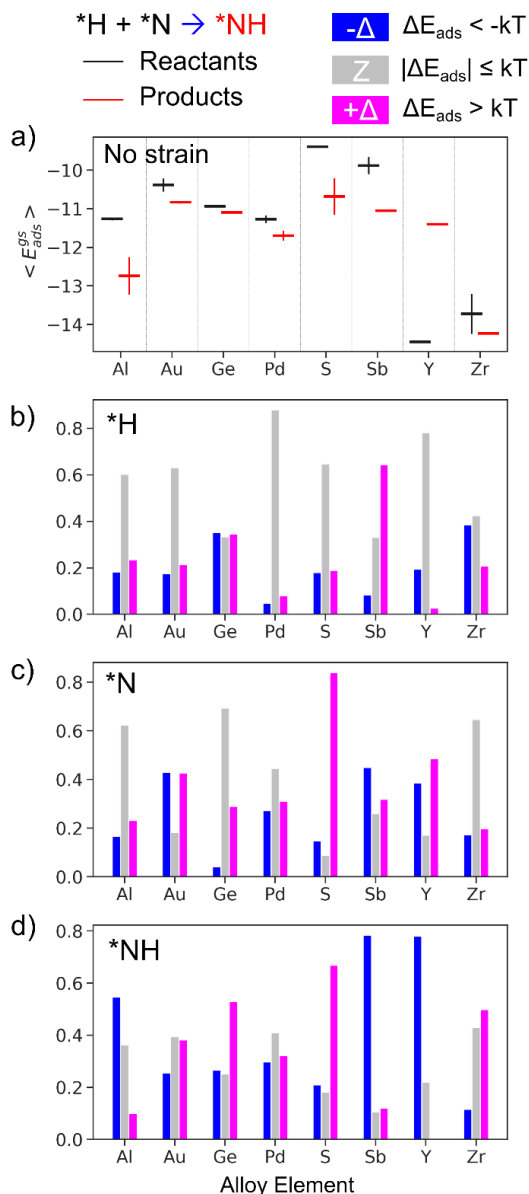
Figure 4.5 Inference results grouped across different catalysts and adsorbates identify Cu-S alloy surfaces as ideal strain engineering candidates for an ammonia synthesis intermediate step. **a)** Reaction enthalpies averaged over zero-strain Cat + Ads structures for *H + *N → *NH. Black lines represent reactant energies, red lines represent product energies; the formation energy of NH is included in the product enthalpy. **b)** Histogram of inferred strain response classes for each Cat + Ads structure containing *H, grouped by catalyst alloy element. **c)** Same as **b)** but for *N as the adsorbate; **d)** same as **b)** for *NH as the adsorbate.

Figure 4.5b-d plots summary inference results for all the Strained Cat + Ads structures containing *H (**Figure 4.5b**), *N (**Figure 4.5c**), and *NH (**Figure 4.5d**) in the inference dataset. For each adsorbate, we plot a histogram of the inference results over strain space, grouped by the alloy composition of each catalyst surface (x-axis) and the predicted class (bar color). We group by alloy element because it is practically one of the first decisions made in catalyst selection and it has a relatively high correlation coefficient

compared to other independent variables such as Cu composition and surface plane (Figure S4.1). As an example, **Figure 4.5b** indicates that the adsorption energy of *H on Cu-Pd surfaces is relatively unresponsive to strain since nearly all strains in the inference set fall in the gray class Z. On Cu-Sb surfaces, strain tends to increase the *H adsorption energy (less favorable interaction), with a strong bias towards pink class $+\Delta$ over class Z and class $-\Delta$. For *N in **Figure 4.5c** and *NH in **Figure 4.5d**, the distributions differ significantly from the *H graph, reflecting the fundamental change in the adsorbate coordination from *H to *N; for example, Cu-Sb alloys bias towards $-\Delta$ for *N and *NH, indicating that strain tends to decrease the adsorption energy (more favorable interaction). Cu-S alloys exhibit a significant number of strains that raise the adsorption energy of both *N and *NH, and **Figure 4.5a** shows that the ground state adsorption energy is also more positive for Cu-S alloys relative to the other compositions. Raising the adsorption energy of *NH with strain is particularly desirable since the average zero-strain reaction enthalpy on Cu-S surfaces is -1.29 eV. This indicates that the Cu-S alloys are suitable targets for our goal of raising the adsorption energy of the $^{*}H + {}^{*}N \rightarrow {}^{*}NH$ intermediates to reduce the magnitude of endergonic steps in the ammonia synthesis reaction.

4.4.5 Phase Diagrams of Surface Strain - Adsorption Energy Response

High-level analysis of the inference results in aggregate identified Cu-S alloys as candidates to increase the adsorption energy of *NH. Copper sulfide catalysts of varying compositions have been recently studied for ammonia synthesis *via* the electrochemical

nitrogen reduction reaction (NRR), which has been suggested to occur at least partially through a dissociative mechanism. [206,207] To further examine the nature of *NH strain response, **Figure 4.6** plots phase diagrams of the inference results as a function of strain for two different catalyst compositions and surface planes in the Cu-S family. The uniaxial norm$\sqrt{\varepsilon_1^2 + \varepsilon_2^2}$ and the shear component ε_6 are chosen as the pseudo-order parameters since they capture most of the variation within strain space while retaining convenient 2D visualization. Empirically, despite combining ε_1 and ε_2 together, we find that these quantities generally give well defined regions in strain space corresponding to one class of predictions. The color scale gives the classifier model prediction for each point in the inference dataset.
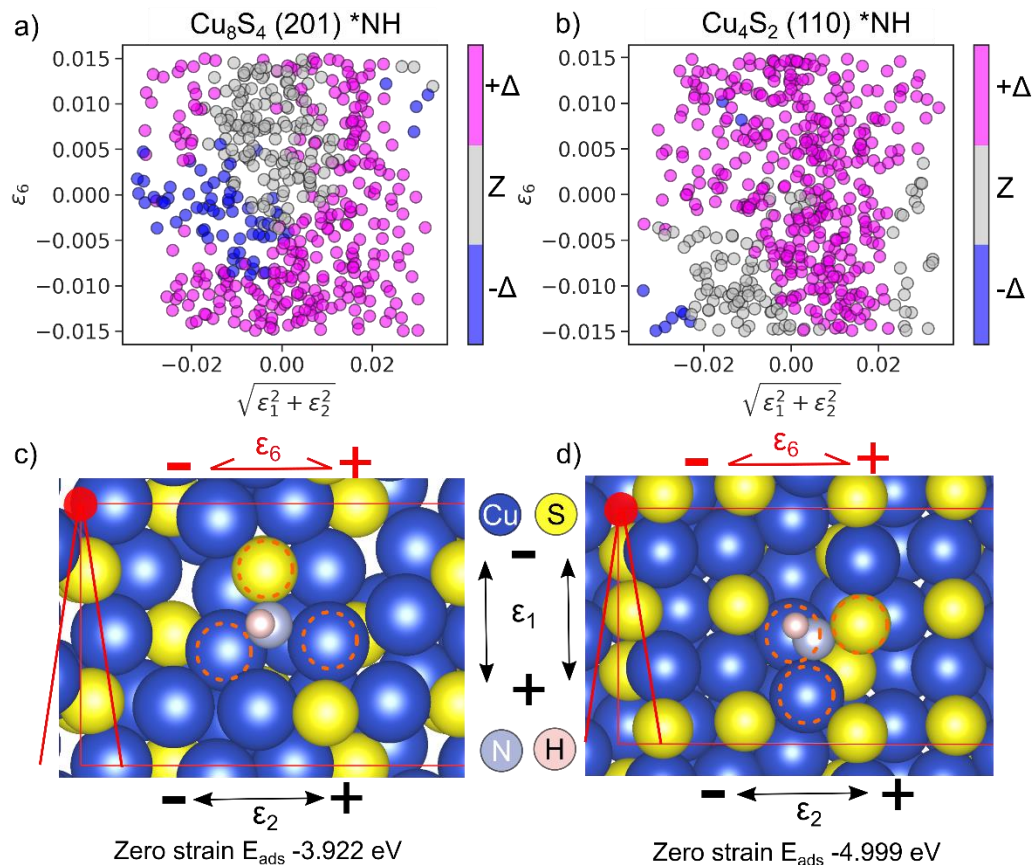
Figure 4.6 Inferred strain phase diagram reflects changes in surface structure response to strain. **a)** Surface strain phase diagram resulting from model inference for $Cu_8S_4(201)$:*NH. Color scale indicates the predicted class of adsorption energy response corresponding to the classes in **Figure 4.3**. **b)** Same as **a)** for $Cu_4S_2(110)$:*NH; there are two distinct regions of inferred strain responses, but the majority of surface strain patterns are predicted to increase the adsorption energy of *NH. **c)** The Cat + Ads zero-strain atomistic structure corresponding to **a)**; the three-fold coordination site (orange circles) includes 2 Cu atoms and 1 S atom in the plane of the surface. **d)** The Cat + Ads zero-strain atomistic structure corresponding to **b)**; the coordination site (orange circles) is similar but the surface structure is much denser than that in **a)**.

Figure 4.6a shows 500 inference points for $Cu_8S_4(201)$:*NH; as indicated by the histograms in **Figure 4.5**, most strains are labeled as class $+\Delta$ and predicted to induce a positive change in the adsorption energy greater than 25 meV. The *NH adsorbate has a 3-fold coordination site of surface atoms (orange circles) which lie nearly parallel to the surface plane consisting of 2 Cu atoms and 1 S atom (**Figure 4.6a** bottom). At low shear strains, compressive uniaxial strain is predicted to reduce the adsorption energy and tensile uniaxial strain is predicted to increase the adsorption energy. This reflects that expanding the coordination environment lengthens the bonds between the surface atoms and the adsorbate, and compressing the coordination environment reduces the bond length, favoring increased covalent interaction. At small uniaxial strains, positive shear strain is predicted to have little impact on adsorption energy, but negative shear strain is generally predicted to increase the adsorption energy. The qualitative difference in the shear predictions reflects the asymmetry of the surface structure, as different directions of strain are interpreted by the model to result in different adsorption energy changes given the same input graph of the zero-strain structure. **Figure 4.6b** shows the inferred strain phase diagram for $Cu_4S_2(110)$:*NH; this surface originates from a different bulk crystal structure with a similar calculated formation energy than that in **Figure 4.6a** but contains the same elemental composition. The coordination environment for *NH appears qualitatively similar to that in **Figure 4.6a**, a 3-fold site with 2 Cu atoms and 1 S atom which centers the adsorbing nitrogen. However, the predicted strain response is quite different; nearly all uniaxial strains increase the adsorption energy, and only a combination of compressive

94

shear and uniaxial strain leads to no effect on the adsorption energy. We attribute this to subtle differences in the ground state coordination environment which reflect the different surface structures; in **Figure 4.6b**, both the ground state coordinating Cu-N bond (2.07 Angstroms) and the N-S bond (1.68 Angstroms) are nearly identical to their bulk ground-state counterparts in Cu_2N (2.06 Angstroms) and molecular S_3N (1.6 Angstroms). Therefore, any strains which disrupt the ability of the surface to preferentially relax into this same coordinating geometry will destabilize the adsorbate relative to the ground state. Since the zero-strain structures are included in the training data, this relative bond length information from the surface can be taken up by the model during training.

4.4.6 Strain Response of the Surface Structure is Altered by Different Adsorbates

In catalysis applications, the surface is often considered as a secondary structural participant in a reaction, since the primary change of interest is bond-making or bond-breaking in the adsorbate. For single-atom adsorbates this is generally a valid assumption, but multi-atom adsorbates can interact with and significantly modify the surface structure. **Figure 4.7** plots inferred ΔE_{ads} strain response phase diagrams for the same surface $HfCu_3(100)$ with two different adsorbates, *N and *NO_2, located at the same adsorption site. The predicted strain response is nearly the exact inverse for the two complexes; for nearly all strain configurations, the adsorption energy is predicted to increase for *N and decrease for *NO_2. To investigate the origin of this difference, we select a strain profile

that falls within a region of the strain diagram exhibiting different strain response for the two adsorbates (black circle) and verify the predictions using DFT calculations. The zero-strain Cat, zero-strain Cat + Ads, and strained Cat + Ads complexes are shown from top to bottom in **Figure 4.7c** for *N and **Figure 4.7d** for *NO_2. The DFT results confirm the model inference predictions - under the same applied strain, the adsorption energy of $HfCu_3$(100):*N increases by 30 meV, while for $HfCu_3$(100):*NO_2 the adsorption energy decreases by 180 meV. At the bulk lattice constant for $HfCu_3$, the adsorption of N shifts the Hf surface atom position by a very small amount to coordinate tightly with N, increasing the Hf-Cu surface bond length by 0.02 Angstroms. The same adsorption process for NO_2 leads to a substantial surface reconstruction, increasing the Hf-Cu surface bond length by 0.61 Angstroms and nearly decomposing *NO_2 into *NO and *O. This change in both the coordination environment of the adsorbate and the surface structure leads to opposing responses to the same applied strain. When the surface is strained away from the bulk lattice constant, the adsorption becomes less favorable for *N, as the Hf-Cu bond is further stretched by 0.02 Angstroms from the equilibrium value of the zero-strain surface. *NO_2 adsorption causes relaxation to the same coordination environment as on the zero-strain surface without distorting the Hf-Cu surface bonds as much, leading to the 180 meV decrease in the adsorption energy. This illustrative example shows how under the same surface strain, different adsorbates can induce local reconstruction that raises or reduces their interaction with the surface relative to the bulk surface. The model makes predictions verifiable by first-principles calculations which enable identification of candidate catalyst-

96

adsorbate combinations exhibiting different adsorption phenomena, providing guidance for practical strain engineering of heterogeneous catalytic reactions.
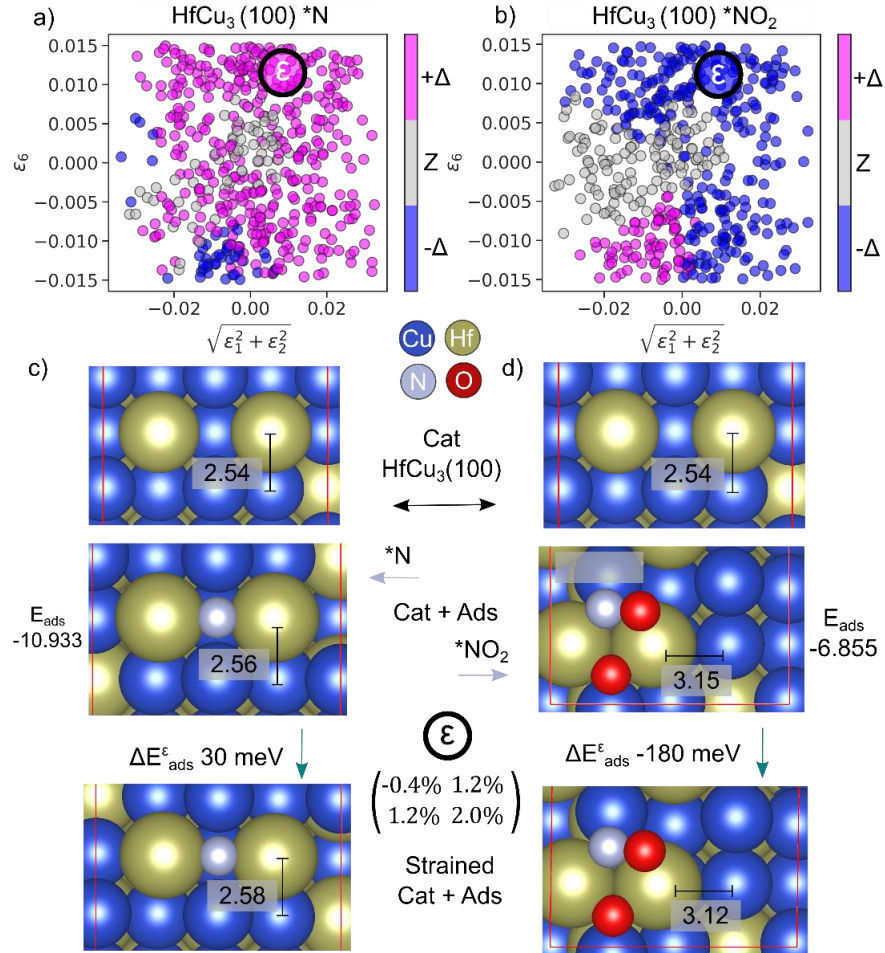
Figure 4.7 a) Strain phase diagram for HfCu$_3$(100):*N shows the majority of strains predicted to increase the adsorption energy. **b)** Strain phase diagram for HfCu$_3$(100):*NO$_2$ shows the majority of strains predicted to decrease the adsorption energy. Black circles in **a)** and **b)** correspond to the strain studied in **c). c)** Atomistic structure of (top to bottom) zero-strain Cat, zero-strain Cat + Ads, and strained Cat + Ads structures corresponding to the deformation shown. **a)**. Strain increases the Hf-Cu surface bond length from the zero-strain case, increasing the adsorption energy. **d)** Same as **c)** for HfCu$_3$(100):*NO$_2$; strain decreases the Hf-Cu bond length towards the zero-strain surface value with no adsorbate, enabling surface relaxation and making adsorption more energetically favorable.

4.5 Conclusion

A key challenge in rational catalyst design is bridging the significant gap between pristine *in silico* structures and experimentally realized structures in nanoparticles or surfaces. Nanomaterial catalysts are especially desirable due to the extremely high ratio of potentially active surface area to material volume, yet this is also where strain introduces the largest deviations in expected structure and function from the bulk. Unfortunately, accounting for so many structural degrees of freedom results in a search space that is computationally intractable with physics-based modeling alone. Machine learning models can work in tandem with conventional simulation to interpolate structure property relationships from a relatively small training set across these vast search spaces within computationally practical timescales. GNNs are early in their application to physical systems and do not yet regularly outperform simpler models such as linear baselines. However, they offer a high potential performance ceiling since they can directly ingest structural information at a high level of detail, which otherwise must be interpreted,

reduced, and converted to features manually. These GNNs have the potential to generalize more effectively across composition and structure with larger training datasets. Additionally, they may be able to generalize to defect structures much more easily than conventional machine learning models since the representation changes with dilute structural modifications. Defect sites are especially interesting for catalyst design since defects are charge active and sensitive to strain. [208]

In this work, we focused on the relationship between the strain applied to the surface and the subsequent change in the adsorbate-surface interaction since this is the primary design criteria in catalyst selection and design. To our knowledge, this is the first application of GNNs to surface strain engineering of catalyst-adsorbate complexes and synthesizes prior efforts to using machine learning for elastic strain engineering and adsorption energy prediction. We introduce a regularization scheme which incorporates prior physical knowledge across subsections of the graph. From our successful classification and regression task training, we identify Cu-S alloys as promising platforms for strain engineering of amino-type adsorption and generate phase diagrams of predicted strain response for several catalyst-adsorbate complexes. We validate several inference predictions with independent DFT calculations and identify structural surface changes corresponding to different effects of strain on adsorption energy. The model is sensitive enough to distinguish the strain response of the same adsorbate on compositionally identical but structurally different surfaces, and different adsorbates on the same exact

surface. Applying these predictions in catalyst synthesis requires further analysis of reasonably achievable strain patterns in a synthesized material or core-shell nanoparticle. Some strain patterns occur spontaneously if they reduce the penalizing surface energy term, while others would require applied stress through epitaxial engineering to be observed. [136] A natural follow-on to this work would be training a similar GNN to predict the change in the surface energy of a slab under a particular strain without the adsorbate. With the two models together, strains which optimize the adsorption energies for a particular reaction can be filtered by their predicted effect on the surface energy; strains which reduce the surface energy would be more likely to spontaneously form in a nanoparticle or ultrathin epitaxially grown surface. Improvements in the precision of epitaxial material growth and core-shell nanoparticle synthesis by bottom-up and top-down approaches has enabled finer control over material structure for a given composition. [209] Using experimentally measured structural data as can help distinguish different reaction mechanisms by enabling relative comparisons of different intermediates and reaction pathways on a particular surface using one model. We anticipate that flexible model architectures such as GNNs will improve catalyst design by bridging the gap between accurate but expensive first-principles simulations and experimentally relevant high-dimensional spaces such as strain.

Chapter 5 Dynamics of Interfacial Mechanics Leads to Continuously Variable Cellular Memory

Reprinted (adapted) with permission from

* Denotes equal contribution.

5.1 Background

Cellular mechanical memory describes how cells acquire and retain information about the mechanical properties of their microenvironment. These extracellular matrix (ECM) properties impact cellular structure, function, and identity, [210–212] and recent experiments suggest that this linkage depends on not just the present microenvironment but the accumulated mechanical history experienced by the cell. [213–219] The mechanism by which this memory is developed, maintained, and lost is not yet understood and exhibits several unusual features. First, the timescale at which the cell responds to mechanical changes through signaling (minutes to hours) is an order of magnitude faster than the timescale of memory development and dissipation (days to weeks). This implies that microenvironmental information is rapidly acquired and used by the cell but stored and released much more slowly. Second, the persistence time of the developed mechanical

memory ranges continuously from no memory all the way to permanent memory (cell differentiation), simply by varying the microenvironmental history that the cell is exposed to (**Figure 5.1a**). This strong coupling between the dynamics of memory retention and the dynamics of the stimulus being remembered is not found in common physical systems such as magnetic or shape memory materials. Understanding these unique dynamical phenomena is critical to engineering cell behavior and fate through temporal control of the cell's physical environment.

Cellular adaptation to changes in the mechanical environment occurs in both the cytoskeletal and nuclear domains. [220,221] On stiff substrates, examples of cytoskeletal phenotype changes include increased clustering of focal adhesions, actomyosin contractility, cell spreading area, and migration speed. [222–224] On soft substrates, contractility is reduced and the mechanical properties of the cell adjust to match that of the surrounding environment by depolymerization of F-actin. [225–227] In the nucleus, the population of transcriptionally active proteins changes with ECM stiffness as certain transcription factors relocate in response to mechanical signals. [228,229] The chromatin structure experiences epigenetic modifications and physical deformation of the nuclear envelope from contractile forces, leading to alterations in gene expression. [230,231] The dynamic nature of mechanical memory development and depletion indicates that information about microenvironmental mechanics is continuously consumed by the cell,

allowing stem cell differentiation to proceed from different time series of mechanical microenvironments. [210,213,215,232]

A hallmark of mathematical models of memory is bistability, which is a property of a system to have more than one steady state, and this concept forms the basis for Waddington's famous landscape of cell differentiation. Bistability alone does not contain any information about dynamics of memory development or retention, only that it can occur. [233,234] Several mechanistic models have been put forward to explain the relationship between mechanics and cell differentiation, [214,235–237] but these models do not simultaneously capture 1) the timescale disparity between mechanical signaling / cell adaptation and memory development and 2) the continuous range of memory outcomes. More generally, regulatory gene network models with different topologies can give rise to memory using network motifs such as positive and negative reinforcement. [238–243] However, explicit molecular network models for mechanotransduction are difficult to develop because there is not enough data available to determine the many model parameters or assert which components of the regulatory network are rate-limiting. This leads to rigid models which are difficult to interpret and cannot generalize across variations in priming time and priming stiffness, limiting their predictive power.

103

5.2 Objective

In this work, we propose a model to describe the dynamics of mechanotransductive memory acquisition and persistence. The model starts from a general molecular framework, incorporating both fast and slow mechanosensitive pathways. We simplify this model to two ordinary differential equations, representing cytoskeletal and nuclear dynamics, respectively. First, we show that simple positive reinforcement between signaling and transcription is sufficient for mechanical memory acquisition. Second, we show that dynamic coupling between the cellular phenotype and the sensitivity of this reinforcement leads to a continuous range of memory persistence time. Biologically, the sensitivity of positive reinforcement corresponds to the *epigenetic state* and *transcriptional environment* of the cell, which govern the steady-state balance between *synthesis* and *degradation* of proteins correlated with either a stiff-ECM or soft-ECM phenotype. The rate at which signaling induces changes in the positive reinforcement sensitivity (*transcriptional environment*) determines memory by shifting the phenotype *(protein composition)* from requiring external mechanical signal to a self-sustaining state. Simulating priming programs that match experimentally tested configurations, we observe emergent cases of no memory, temporary memory, and quasi-permanent memory (differentiation) by varying only the priming time and keeping other model parameters fixed. In designing future experiments or therapeutics, this simple but robust framework could help decouple the importance of positive reinforcement of mechanosensitive gene

expression and their sensitivity to mechanical cues, thus optimizing the role of mechanical memory in optimizing biological outcomes.

5.3 Methods

5.3.1 Model for Dynamic Mechanosensitivity in the Cytoskeleton and the Nucleus

We begin our model of mechanotransduction and mechanosensitive gene expression by introducing a variable x which represents the average functional concentration of all the stiff-activated proteins and transcription factors in the cell. Examples of cytoskeletal protein components contributing to x include F-actin (or α-SMA), vinculin, and integrins. Transcription factors contribute to x through their transcriptionally eligible concentrations, which incorporates nuclear localization as well as cell concentration. Examples of transcription factors with well-known stiff-correlated nuclear localization include YAP [244,245], MKL-1 [229,246], and RUNX2. [247,248] Finally, we include epigenetically modifying enzymes such as HDAC and HAT as contributing components to x, which influence chromatin organization and demonstrate mechanosensitive activity patterns. [217] While these contributing components to x have independent dynamics, we pursue an approximate approach since limited data is available to characterize all the individual interactions between mechanosensitive components. As an average, x measures the net mechanoactivation of the cell induced by increased ECM stiffness. The linear dynamics of x can be written as:

$$\frac{dx}{dt} = k_{x\uparrow}(m)\left(x_{ref} - x\right) - k_{x\downarrow}(m)x \tag{5.1}$$

where m is the matrix stiffness, $k_{x\uparrow}(m)$ gives the mechanosensitive rate of cytoskeletal protein synthesis and/or transcription factor nuclear import, $k_{x\downarrow}(m)$ gives the rate of the reverse processes (degradation and nuclear export), and x_{ref} is a reference level of mechanoactivation at a characteristic stiffness m_0. Processes described by $k_{x\uparrow}(m)$ are shown with blue arrows in **Figure 5.1b**, while processes described by $k_{x\downarrow}(m)$ are shown with red arrows. We choose $k_{x\uparrow}(m)$ to be a monotonically increasing but saturating function of stiffness, $k_{x\uparrow} = \tau_{x\uparrow} - \exp(-\frac{m}{m_0})$, to capture the mechanosensitivity of stiff activation, and for simplicity we choose the degradation and export rate $k_{x\downarrow}(m)$ to be a constant $\tau_{x\downarrow}$ over stiffness. [245] This is motivated by experimental evidence that nuclear import of transcription factors is more mechanosensitive than nuclear export [245] and that cellular response saturates at very high stiffness. [249] While specific functional choices are arbitrary, the results we present are general to different functional forms which maintain positive correlation of $k_{x\uparrow}$ with stiffness.
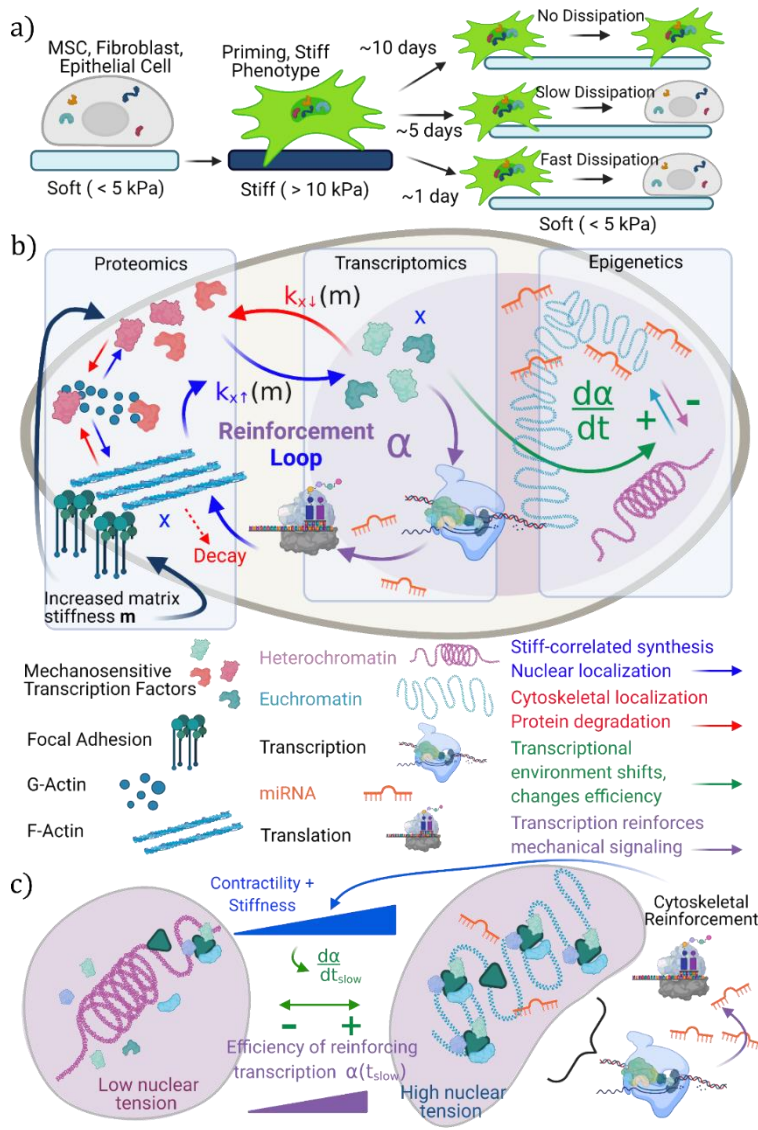
Figure 5.1 a) Cells alter their phenotype on stiff substrates (priming) within hours. The phenotype retention time when the cell moves back to soft substrates depends on the priming time length on the scale of days. **b)** Integrated cellular picture of mechanosensitive signaling and positive reinforcement enabled by transcription and translation. Stiff phenotype changes are associated with blue arrows, soft phenotype changes with red arrows. **c)** The chromatin state changes slowly in response to nuclear tension, epigenetic changes, and shifts in the post-transcriptional regulation environment, affecting the efficiency of reinforcement.

5.3.2 Transcription Creates Positive Reinforcement Loop for Mechanical Signaling

Next, we consider that the transcriptional activity of the many individual components of x creates a positive reinforcement loop by enhancing adaptations to

107

increased stiffness of the ECM. For example, YAP and MKL-1 activate transcription of genes which lead to increased stability of focal adhesions, F-actin, and contractility through Rho-Rock pathways and support of G-actin polymerization. [250–252] This stabilization releases additional bound cytoplasmic transcription factors to translocate to the nucleus, further increasing x. The transcriptional positive reinforcement is depicted in **Figure 5.1b** by the purple arrows; we incorporate this positive reinforcement mechanism into Eq. 5.1 by adding a nonlinear Hill relation:

$$\frac{dx}{dt} = k_{x\uparrow}(m)\big(x_{ref} - x\big) - k_{x\downarrow}(m)x + \alpha \frac{x^\beta}{x^\beta + 1} \qquad (5.2)$$

Here α is the sensitivity of the positive reinforcement and β determines the sharpness of the Hill function, which transitions from a low value to a high value like a smoothed step function. Positive reinforcement loops in cells have been extensively modeled using Hill relations and are a known source of bistability in dynamical systems. [253–255] Bistability indicates at least two steady-state solutions to a dynamical system and underpins hysteresis and memory in many physical systems. Biologically, the sensitivity parameter α contains all the information about the efficiency of the mechanosensitive self-reinforcement, which directly corresponds to the transcription landscape. Like x, we consider α to be an average measure over many components involved in regulating the transcription-translation pipeline, including proteins, mRNA, non-coding miRNA, and the fraction of heterochromatin to euchromatin in the nucleus. Implicitly, a subset of these α components

depend on mechanosensitive components of x and therefore m, coupling cytoskeletal mechanosensing to nuclear activity in our model. **Figure 5.1c** illustrates how changing α reflects changes in both 3D chromatin architecture and post-transcriptional regulation, altering the efficiency of mechanosensitive transcription. In the heterochromatic state, fewer chromatin sites are available for transcription. In the more active euchromatic state, a complex and modifiable regulatory environment (including miRNAs) exists in between the chromatin and downstream protein expression. These transcriptional machinery and regulatory components interact with significant complexity and co-dependency, and there is insufficient data to parametrize a full microscopic description of these interactions. A generalized derivation for α is given in the Appendix S5.1 which considers these nonlinear interactions by expanding α as a series expansion of terms weighted to account for cooperativity between regulatory components.

5.3.3 Fast and Slow Dynamics of Transcriptional Reinforcement Sensitivity

Since x and m have time dependence, we know that α must also have a dynamic evolution $\frac{d\alpha}{dt}$ which is bounded on the fast end by $\frac{dx}{dt}$ and $\frac{dm}{dt}$ because of the underlying dependence of α components on mechanosensitive x components. On the slow end, the dynamics of α can be severely limited by complex rate-limiting or anti-cooperative relationships between the transcription-translation regulatory components. Evidence of these time-dependent relationships between reinforcement and transcription has been collected on some individual mechanosensitive mechanisms. [256,257] Although we lack

109

the data and explicit mechanistic understanding to specify *all* the contributing mechanisms to α, we can capture the essential nature of this time dependence by rewriting α as the sum of a fast-changing component (on the scale of $\frac{dm}{dt}$ or $\frac{dx}{dt}$) and a slow changing component which is effectively constant on the timescale of x and m. Complete details of the derivation beginning from the series expansion of α are included in Appendix S5.2; the result for $\alpha(t)$ is:

$$\alpha(t) = \alpha(t_{slow}) + c\frac{m^{\zeta}}{m^{\zeta} + 1} \tag{5.3}$$

We use another Hill relation in stiffness m with degree ζ and sensitivity c to model the fast portion of α, which captures the fact that the positive reinforcement sensitivity is explicitly mechanosensitive and that stiff reinforcement requires the presence of mechanosensitive transcription factors such as YAP and MKL-1 to occur. [250,251,258–260] Recent evidence indicates that the nuclear structure and chromatin conformation physically responds to environmental stiffness *via* forces transmitted through the LINC complex and not merely through chemical signals, and these direct processes are captured by this fast component of $\alpha(t)$. [221,261,262] For the remaining term $\alpha(t_{slow})$, we choose a form which generally depends on x and m such that $\frac{\partial \alpha}{\partial t_{slow}}(x,m)$ represents a weighted average of the slow, nonlinear dynamics present in transcription-translation reinforcement.

110

Plugging Eq. 5.3 back into Eq. 5.2, our time-dependent equation for cellular mechanoactivation is now:

$$\frac{dx}{dt} = k_{x\uparrow}(m)(x_{ref} - x) - k_{x\downarrow}(m)x + (\alpha(t_{slow}, x, m) \tag{5.4}$$

$$+ c\frac{m^{\zeta}}{m^{\zeta} + 1})\frac{x^{\beta}}{x^{\beta} + 1}$$

In this ordinary differential equation (ODE), we established mechanosensitivity of synthesis and nuclear import of x (first term), mechanosensitivity of degradation and nuclear export of x (second term), and positive reinforcement of cellular mechanoactivation (third term) with a time-dependent sensitivity that evolves slowly with respect to changes in x. Eq. 5.4 is the key ODE which underpins the results. We can interpret this equation as the negative gradient of a "Waddington-like" energy landscape with respect to x; $\frac{dx}{dt} = -\frac{\partial U}{\partial x}$. Since $\alpha(t_{slow}, x, m)$ evolves on a much slower timescale than $\frac{dx}{dt}$, we treat α as a constant when finding the steady state solutions of x. Integrating Eq. 5.4 we arrive at

$$U(x, m, \alpha) = -k_{x\uparrow}(m)x_{ref}x + \frac{x^2}{2}(k_{x\uparrow}(m) + k_{x\downarrow}(m)) \tag{5.5}$$

$$+ x\left(\alpha + c\frac{m^{\zeta}}{m^{\zeta} + 1}\right)\left(\,_2F_1\left[1, \frac{1}{\beta}, 1 + \frac{1}{\beta}, -x^{\beta}\right] - 1\right)$$

where $\,_2F_1$ is the special hypergeometric function.

The model was implemented using a standard ODE solver (fsolve) in the open source SciPy package (Python). Parameter selection for numerical simulations was performed using latin hypercube sampling over the following parameter space: α_0 (initial value for positive reinforcement), m_0 (stiffness normalization constant), x_{ref} (reference level of mechanoactivation), τ_s (timescale for $\frac{d\alpha}{dt}$), $\tau_{x\downarrow}$ (timescale for x decrease), $\tau_{x\uparrow}$ (timescale for x increase), ζ, c (degree of Hill relations), σ (standard deviation of noise), and A (amplitude of noise). Each parameter combination was run for priming times of 3, 7, and 10 days, with 250 noisy trials run for each priming time. Parameter combinations were scored against the experimental data from Yang *et* al. [215] using a Kolmogorov-Smirnov test, a least-squares test, and manual inspection. We note that these parameter combinations do not represent global best-fits to the data but were sufficient to show qualitative agreement and differentiate the two different dynamics approaches.

5.4 Results

Figure 5.2 Example microscopic mechanosensitive positive reinforcement loop. Relationships assembled from the literature illustrate one example of a positive reinforcement loop in mechanotransduction mediated by transcription factors. In the model, the stiff mechanoresponse corresponds to larger x, while the soft mechanoresponse corresponds to smaller x. The degree of positive reinforcement is controlled by the intensity and magnitude of the activation, inhibition, and transcription arrows, which is captured by α in the model and exhibits both fast and slow dynamics.

By taking x and α as average quantities over many interacting mechanosensitive components, our implemented model framework sacrifices some mechanistic detail. However, we successfully identify that nonlinear dependence of the positive reinforcement strength on the level of mechanosensation can lead to all the features of mechanical memory observed in experiments. A mechanistic example of this type of positive

113

reinforcement is given in **Figure 5.2** with connections to the model components illustrated in **Figure 5.1**. Under a stiff mechanoresponse, focal adhesion, integrin, and stress fiber density all increase [263] from increased F-actin polymerization, freeing transcription factors such as MKL-1, YAP, and HDAC to translocate to the nucleus. [217,264] These processes correspond to the mechanosensitive linear dynamics introduced in Eq. 5.1. Significant crosstalk has been observed for these transcription factors, which can lead to nonlinear dynamics [265] such as those introduced in Eq. 5.3. MKL-1 acts as a transcription factor for the production of miR-21 [214], which was found to regulate mechanical memory. miR-21 has also been shown to affect YAP via RUNX1 and RUNX2, which are also mechanosensitive transcription factors. [266] Finally, YAP has been shown to regulate actin dynamics, stabilizing F-actin through the Rho pathway [267], closing the positive reinforcement loop. These processes are examples of fast-acting positive reinforcement; meanwhile, epigenetic modifiers can lead to slow dynamics of chromatin conformational change. [268,269] While this is not a complete account of mechanotransductive pathways by any means, this illustrates one example of mechanically initiated positive reinforcement which couples the cytoskeleton and nucleus and can lead to memory.

5.4.1 Phase Diagram of Cellular Mechanoactivation Shows Selective Bistability

We can visualize the steady-state solution space of x through the lens of the energy landscape defined by Eq. 5.5. **Figure 5.3a** gives a phase diagram with three distinct regions

of the solutions of x (identified as local minima in the free energy landscape) as a function of the dimensionless ECM stiffness $\frac{m}{m_0}$ (y-axis) and the reinforcement sensitivity α (x-axis). The insets on the phase diagram show representative slices of the energy landscape for a point (α, m) within each region of the landscape.

In orange region I (low reinforcement sensitivity and stiffness), the energy minimum and single corresponding steady state is found at small x. In this monostable region, there is low mechanical signal from the soft ECM, and low α corresponds to a small influence of the positive reinforcement process on x. In light blue region II, the system is still monostable, but the increased ECM stiffness induces mechanical signaling and shifts the steady-state value of x to a much higher value than in region I. Biologically, this corresponds to mechanotransductive responses which occur on a timescale of hours, such as polymerization of G-actin to F-actin and increased density of focal adhesions, stress fibers, and integrins. Compared to region I, a cell in region II exhibits greater nuclear localization of transcription factors such as YAP, RUNX2, and MKL-1, and increased focal adhesions, contractility, and areal spreading (**Figure 5.1b**). When $m \gg m_0$, this mechanically induced phenotype shift occurs for all values of reinforcement α. In dark blue region III (low stiffness and large reinforcement sensitivity), the system is bistable; there are two steady states for x, one corresponding to a soft phenotype (expected due to the ECM stiffness) and one corresponding to a stiff phenotype (stabilized by the positive

115
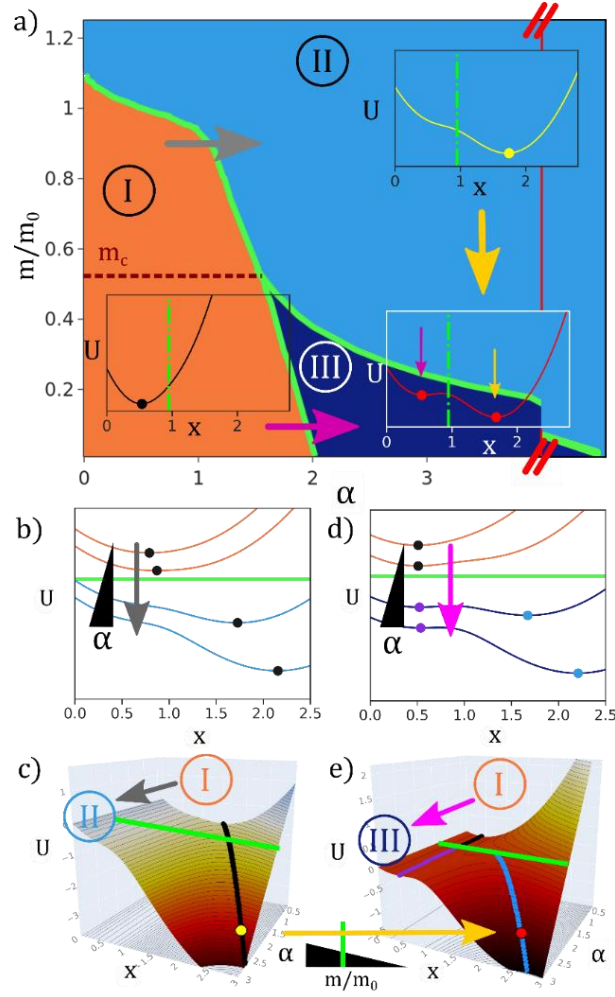
Figure 5.3 Phase diagram of the stiff-correlated phenotype. **a)** Phase diagram of steady-state stiff phenotype expression over ECM stiffness and transcriptional reinforcement sensitivity. Insets show a slice of the energy surface vs. x for a typical point in each region; the dots mark the minima and the steady state values of x. **b,c)** Transitioning from I to II (gray arrows) leads to a significant increase in the steady-state value of x. Green line indicates the phase boundary between regions. **d,e)** Transitioning from I to III (pink arrows) at constant stiffness traps the system in a low-x steady state. The transition from II to III by softening stiffness at large α (gold arrows) keeps the system in a high-x minima. reinforcement even without direct mechanical signal). For a given value of ECM stiffness

and reinforcement sensitivity in region III, the cell will exhibit either low or high mechanoactivation contingent on the prior mechanical history and the gene expression environment. This hysteresis forms the basis in this framework for cellular mechanical memory.

Dynamically, region boundaries (green lines) in the phase diagram can be crossed by altering either the ECM stiffness or the reinforcement feedback sensitivity, inducing transitions in the steady-state mechanoactivation. Considering the soft phenotype region I as the initial condition, there are two possible transition pathways. Traversing to region II by increasing α above a critical stiffness (gray arrow) leads to a continuous and reversible increase in the observed value of x (**Figure 5.3b,c**). If the mechanical signal is then removed (region II to region III, gold arrow), x will remain elevated as the minimum from region II smoothly transitions to the large x minima in region III (**Figure 5.3c,e**). Traversing from region I to region III below the critical stiffness value (pink arrow, **Figure 5.3d**) will not observably change x from the low region I value, since the region I minimum smoothly transitions to the small x local minimum in region III (**Figure 5.3e**). Further increasing the positive reinforcement sensitivity within region III eventually leads back to region II, with a single 'stiff' steady state at large x for all values of ECM stiffness. The hysteresis loop created by the path dependence in the stiffness-reinforcement phase diagram provides a mechanism for dynamic mechanosensitive memory. A key feature of the phase diagram which corresponds to experimental observations is that increasing

117

mechanical stiffness alone can increase x, allowing the cell to begin adapting to the environment on short timescales by expressing stiff-correlated proteins and localizing stiff-correlated transcription factors to the nucleus. [210] However, these changes are fully reversible (exhibit no memory) unless the sensitivity of the positive reinforcement is sufficiently large. In the next section, we explore how evolving α on a slow timescale can lead to different expressions of mechanical memory depending on the time program of external mechanical stimulus.

5.4.2 Nonlinear Dynamics of Positive Reinforcement Sensitivity Capture Full Range of Memory Retention Outcomes

Having shown that the trajectory of α can determine if memory is observed for a particular ECM mechanical history, we return to $\alpha(t_{slow})$ in Eq. 5.3 and consider an explicit form for the slow evolution of the reinforcement sensitivity. Given sufficient data on low-level biological dynamics, $\alpha(t_{slow})$ can be rigorously derived from Eq. S5.3 (Appendix S5.2), but in lieu of this data, we choose the following form to maximize simplicity while capturing key phenomenological features from experiment:

$$\frac{d\alpha}{dt_{slow}} = \begin{cases} -\dfrac{\alpha - \alpha_0}{\tau_f}, & I \\[2mm] \dfrac{\alpha}{\tau_s}\dfrac{m}{m_0}\exp-\dfrac{x}{x_{ref}}, & II \\[2mm] -\dfrac{\alpha}{\tau_s}\dfrac{m_0}{m}\exp-\dfrac{x}{x_{ref}}, & III \end{cases} \qquad (5.6)$$

118
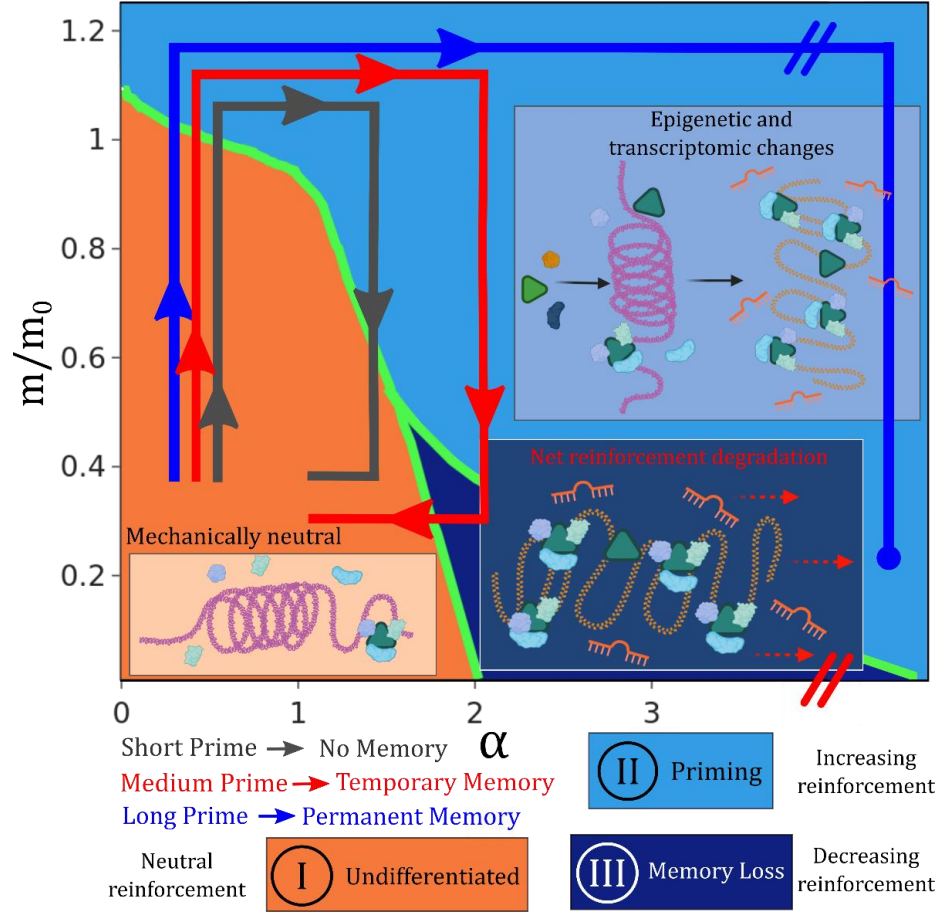
Figure 5.4 Dynamics of the transcriptional environment. In region I, the cell receives little mechanical signal and has limited positive reinforcement, so there is no driving force for the transcriptional environment to shift. In region II, signaling is sufficient to drive chromatin reorganization and changes to the post-transcriptional regulatory environment, such as miRNA synthesis. In region III, the mechanical signal is lost and there is net degradation / reversal of the stiff-correlated phenotype. As self-reinforcement α increases, less external mechanical signal is required to maintain the stiff phenotype cultivated in region II.

where τ_f and τ_s are time constants on the scale of hours and days, respectively, and can be directly related to $\frac{dy_i}{dt}$ and $\frac{dz}{dt}$ in Eq. S5.4. **Figure 5.4** overlays the biological interpretations

of the different piecewise components of Eq. 6 on top of the phase diagram from **Figure 5.3a**. The y-axis remains the rescaled ECM stiffness m/m_0 and the x-axis the strength of positive mechanosensitive reinforcement α.

In region I (low stiffness and cytoskeletal reinforcement) we simply set $\frac{d\alpha}{dt_{slow}}$ to quickly converge to a reference value α_0. At low levels of mechanical signaling and without prior mechanical activation, there is no driving force to spur phenotypic change. While soft ECMs promote cell differentiation and memory, in our example we are only considering stiff-correlated genes for x, and there is no evidence for undifferentiated cells to develop memory which *resists* stiff priming. In **Figure 5.4**, this corresponds to no change in the chromatin state or transcriptional activity over time. Memory develops at high stiffness and is lost at low stiffness unless the cell differentiates, so we choose α to increase in region II and decrease in region III to complete our piecewise description. By our definition, increasing $\alpha(t_{slow})$ in region II accounts for slow, nonlinear processes (shifts in the 3D chromatin and transcriptional regulation environment) which increase reinforcement of a stiff cellular phenotype (**Figure 5.4**). Decreasing $\alpha(t_{slow})$ in region III models net decay of these stiff phenotype features (which can have lifetimes on the scale of days to weeks [270]) and reversal of the transcriptional environment in the absence of sufficient mechanical signal.

Table 5.1 Parameters for simulations in **Figure 5.5a-d**.

Parameters (Fig. 5.5)	Values	Units
Phase Diagram		
m_0	6.5	kPa
x_{ref}	2.	Arb.
β	6	n/a
ζ	35	n/a
c	1.	Hours^{-1}
$\tau_{x\downarrow}$	1.5	Hours
$\tau_{x\uparrow}$	1.5	Hours
Dynamics		
τ_f	12.	Hours
τ_s	150.	Hours
α_0	1.	Arb.
Priming		
m_{stiff}	10	kPa
m_{soft}	2	kPa

In the priming region II, multiplying by $\frac{m}{m_0}$ ensures that the priming time required to achieve a given level of memory decreases when increasing the priming stiffness. Including a dependence on x ensures that the persistence time of mechanical memory increases nonlinearly with priming time for a specified priming stiffness. [215] Mechanistically, our definition of x includes mechanosensitive epigenetic modifiers such as HDAC and HAT [217,271,272], and while the activity of these enzymes to flip epigenetic marks occurs on shorter timescales relative to memory [271], chromatin structural organization and downstream effects on transcription can be much slower due to glassy dynamics of actual chromatin conformational change [269,273,274]. This couples the slow dynamics of the reinforcement sensitivity to the steady-state value of x, which changes depending on the specific location within each region of the phase diagram. This coupling of reinforcement sensitivity to the signal itself is a new feature of our model which has not been studied in other models of cellular positive reinforcement loops. For simplicity and to limit free parameters, we choose the α degradation dynamics in region III to be the reverse of the priming dynamics. Net degradation of the reinforcement and dissipation of

121

memory will be faster at smaller m and will smoothly change from the value of α in region II.

Each of the three arrows (grey, red, and blue) in **Figure 5.4** correspond to a different hypothetical stiff priming program which leads to a different class of memory outcome. The initial conditions, priming stiffness, and model parameters (Table 1) are fixed across the three programs. The corresponding time evolution of x and α for each mechanical
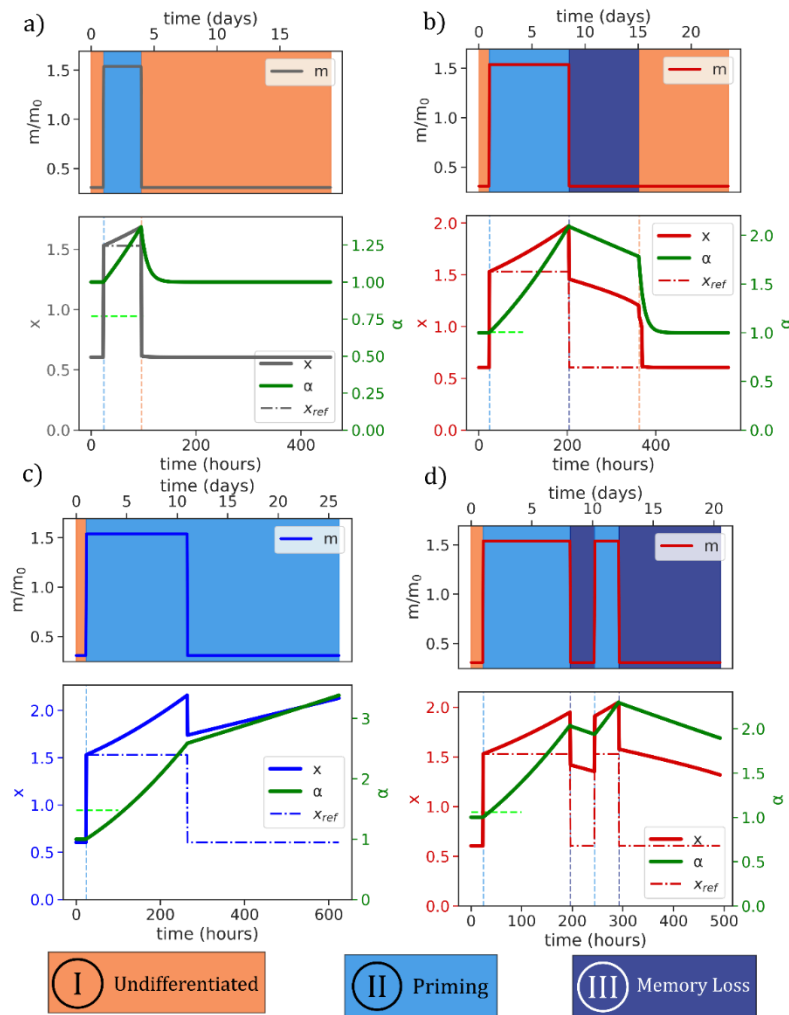
Figure 5.5 Applying different mechanical priming programs. Dot-dash lines x_{ref} indicate the value of x without α dynamics ($\alpha = \alpha_0$). Trajectory colors match those in **Figure 5.3**. **a)** Short priming time of a few days does not result in memory. **b)** Medium priming time results in memory on the timescale of priming; eventually this memory decays and the system resets. **c)** Longer priming time prevents the system from entering the memory dissipation region when the substrate stiffness is decreased, leading to permanent memory. All model parameters in **a)**, **b)**, and **c)** are fixed except for the length of priming time in the mechanical program (top plots). **d)** Two-phase mechanical priming program illustrates cumulative priming. The first priming phase is identical to **b)**, and the total priming is equivalent to **c)**. The second priming pulse generates significantly more memory than the first priming pulse, yet permanent memory is not established as in **c)** since some priming decays between the two pulses.

priming program is plotted in **Figure 5.5a-c**. Between each of the three priming program results shown in **Figure 5.5a-c**, only the length of time that the simulated cell is exposed to stiff substrate (10 kPa) is changed; the soft substrate is modeled at 2 kPa.

5.4.3 Priming Programs and Memory Formation

The grey program does not exhibit any memory – the time that the cell is exposed to the stiff environment is short, and when the cell is returned to a soft ECM, the system returns to region I. While the phenotype quickly shifts to respond to the stiffening substrate at the beginning of the priming program (crossing the dashed green line corresponding to the boundary between regions I and II), the mechanical signal is not maintained long enough to alter the transcriptional environment to the point where it can sustain memory. The stiff phenotype is lost just as rapidly as it was gained (timescale of hours) since the

dynamic trajectory returns directly to region I when the stiffness is relaxed. In the case of a stem cell, this corresponds to an insufficient mechanical signal to sustain differentiation.

The red program in **Figure 5.4** exhibits temporary memory – by holding the cell in priming region II for longer than the gray program, α increases sufficiently such that when the cell is returned to a soft environment, it enters the bistable region III. The positive reinforcement loop traps the system in a steady state of large x despite the absence of persisting stiff mechanical signaling (**Figure 5.5b**). The dot-dash line x_{ref} shows the phenotype expression of x in the absence of α dynamics (α is fixed at α_0) under the same priming program. The significant deviation of x from x_{ref} represents the 'phenotypic distance' of the cell from the low reinforcement case; the length of time that this difference is maintained (while the cell is in region III) gives the length of time of observed memory. Since the dynamic evolution of α fundamentally changes the energy surface, the persistence time of memory is decoupled from the relaxation rate of x, as is observed experimentally. Depending on the specific length of priming time and priming stiffness, the model predicts a continuous range of memory persistence times from much shorter than the priming time to much longer than the priming time using the same parameter set. Over time, α slowly decreases (driving x to decrease) due to the absence of continued signaling promoting epigenetic change and natural degradation of stiff phenotype proteins, dissipating memory and eventually returning the system to region I. The model also predicts that as substrate stiffness decreases after priming, the window of reversible

124

memory (range of α which corresponds to region III) grows significantly. This means that the phenotype of the cell is more likely to be reversible if the dissipative mechanical signal is stronger.

Finally, the blue program corresponds to permanent memory, which in the case of MSCs indicates lineage specification to a stiff phenotype (osteocyte). As the sensitivity of the positive reinforcement α continues to increase, it requires a stronger reversing signal (softer ECM) to enter the bistable, temporary memory regime. At a certain point (beyond the axis break in **Figure 5.4**), it becomes practically impossible to sufficiently reverse the mechanical signaling and the cell will permanently exhibit a phenotype correlated with large x and saturated large α. *In vitro* experiments confirm that differentiated osteocytes exhibit sustained higher nuclear activation of YAP/TAZ and other stiff-correlated proteins, qualitatively agreeing with our picture of a phenotype which retains features of high x. [259] **Figure 5.5c** shows how simply increasing the priming time using the same ECM stiffnesses of the mechanical programs in **Figure 5.5a** and **Figure 5.5b** prevents the system from leaving region II of the phase diagram after the priming phase. Physically, this means that the transcriptional and epigenetic state of the cell has absorbed enough mechanical signal during the priming phase to self-sustain the stiff phenotype once that signal is

removed. Even after reducing the ECM stiffness, α and x will continue to slowly increase until they reach a saturation value which corresponds to lineage specification. [275] The
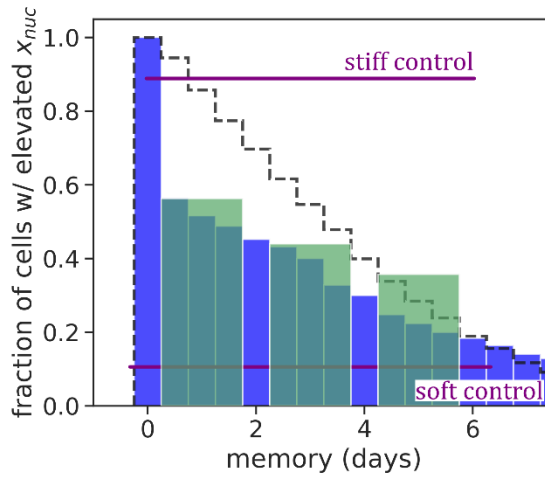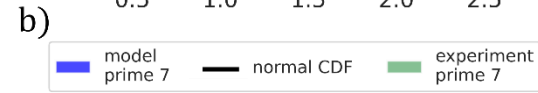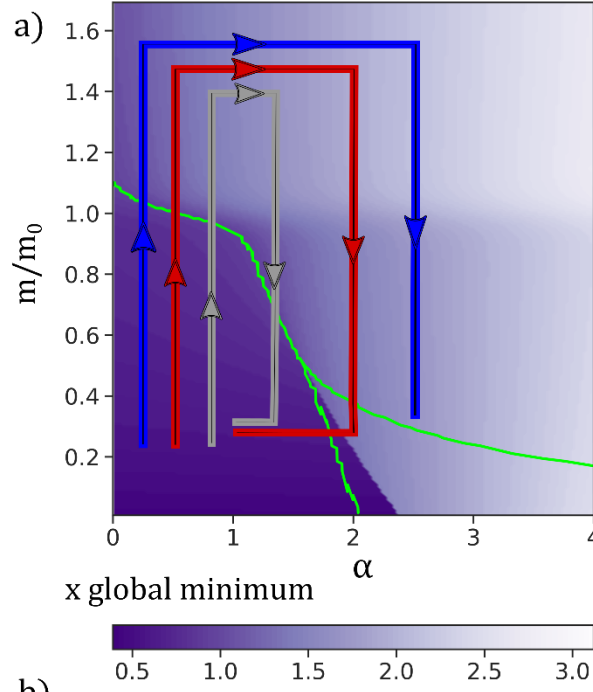
Figure 5.6 Adding noise to nonlinear α dynamics. **a)** Global energy minima of x vs. α and m overlaid with priming programs. **b,c)** Cumulative distribution (CDF) of memory times from simulations with slow, gaussian noise incorporated onto $\frac{d\alpha}{dt}$ for priming of 7 days (**b**) and 10 days **c)**), matching experimental conditions from Yang *et al*. Black dashed line shows the CDF of a normal distribution with the same mean and standard deviation as the model distribution for reference.

model predicts that this transition to a 'permanent' phenotype is a result of the net

126

cumulative mechanical signal absorbed by the cell; for example, consecutive short priming programs will have an additive effect due to the dynamics of α in regions II and III (**Figure 5.5d**). In this trajectory, the initial priming period is the same as that in **Figure 5.5b,** but the short second prime ends up building significantly longer memory than in **Figure 5.5b** due to the accumulated 'environmental knowledge' which is not dissipated in the short intermediate soft period. This agrees with experimental evidence that cyclical stretching and stress stiffening of cellular substrates induces stiff differentiation (a 'pumping' effect). [276–278] The model also predicts that if the epigenetic / transcriptional state labeled by α is manipulated by a drug or other mechanism, the cell can lose its permanent mechanical memory and be 'reprogrammed', which corresponds physically to reversible lineage specification enabled by so-called Yamanaka factors. [279]

5.4.4 Noisy α Dynamics Qualitatively Captures Experimental Memory Distributions

We have so far identified and predicted a wide range of phenomenological features of cellular mechanical memory with our simple, dynamic positive reinforcement model at the single cell level. However, biological systems are inherently noisy and experimental measurements of cellular phenotype and mechanical memory are most often taken over a population of cells. We categorize possible random fluctuations in our model into two categories – noise which affects mechanosensation and signaling ('fast' noise) and noise which affects the slower dynamics of reinforcement ('slow' noise). 'Fast' noise contains

all the fluctuations which might cause the phenotype of a cell to not occur at the local minimum of the energy landscape on fast timescales (deviations away from steady state). This is particularly relevant in the bistable region III, where fluctuations could cause cells to jump between different local minima, corresponding to changes in phenotype and changing observations of memory. In a bistable energy landscape, a normal distribution of fluctuations away from steady state values of x will bias a population towards the global minimum over the local minimum since the jump rate will be higher if the energy barrier height between wells is lower. [275] **Figure 5.6a** shows the global minimum steady state value of x over the stiffness-reinforcement phase diagram from **Figure 5.3a** (region boundaries in green). In the

Table 5.2 Parameters for simulations in **Figure 5.6b,c**

Parameters (Fig. 5.6)	Values	Units
Phase Diagram		
m_0	6.1	kPa
x_{ref}	1.2	Arb.
β	4.9	n/a
ζ	35	n/a
c	1	Hours^{-1}
$\tau_{x\downarrow}$	1.1	Hours
$\tau_{x\uparrow}$	1.5	Hours
Dynamics		
τ_f	12.	Hours
τ_s	160.	Hours
α_0	1.	Arb.
Noise		
σ	0.7	Arb.
A	0.01	Arb.
Priming		
m_{stiff}	10	kPa
m_{soft}	2	kPa

majority of region III, the high-x minimum is lower in energy. For our purposes of stiff

priming programs which enter region III from a single-minima, high-x state in region II, this means that fluctuations from steady state will tend to reinforce a noisy

population to remain in the high-x state, preserving memory and having little qualitative effect on the model results.

'Slow' noise captures fluctuations in the dynamic evolution of α, and this is more interesting to consider due to the nonlinearity of $\alpha(t)$. The fact that $\frac{d\alpha}{dt}$ depends on the current steady state of x (and therefore the prior history of $\frac{d\alpha}{dt}$) means that a normal distribution of noise in the dynamics of α could lead to a non-normal distribution of memory results. We investigated the impact of including noise on $\frac{d\alpha}{dt}$ by introducing a normal distribution of noise with 0 mean, unit standard deviation, and magnitude A=0.01 at each time step of the simulations conducted in **Figure 5.5a-c** and generating a distribution of results over N = 256 simulations. The distribution of memory times observed from the noisy simulations is shown in blue in **Figure 5.6b,c**. This data contains all simulation runs including those without memory, so the difference between the first bin and second bar shows the percentage of trials (cells) which did not exhibit any mechanical memory. The thin black line gives the cumulative distribution function of a normal distribution with the same mean and standard deviation as our generated dataset. This confirms that applying normally distributed noise to the dynamic evolution of α results in a non-normal distribution of observed memory persistence times due to the non-linearity of the α dynamics.

Experimental data on persistence time of YAP and RUNX2 nuclear localization as a function of priming time on stiff substrates (10 kPa) taken from [215] is overlaid on **Figure 5.6b,c**. We averaged their results from YAP and RUNX2 to get a general sense of how the mechanoactivated cell population changes over time (green bars) after the substrate is switched from stiff to soft (2 kPa). The purple control lines indicate the experimental baseline of mechanoactivation in nuclear localized YAP and RUNX2 without any substrate switching. With added noise, our model captures the qualitative changes in the phenotype distribution over time as priming time is changed, with longer-primed cells being more resistant to return to the soft control phenotype. As in **Figure 5.5**, all parameters aside from priming time are held constant between the **Figure 5.6b** and **Figure 5.6c** to best replicate the experimental conditions (**Table 5.2**). In both the experimental data and the model, 10 days of priming leads to significantly higher retention of the stiff phenotype in the cell population than 7 days of priming.

To isolate the effect of the nonlinear coupling between mechanical signaling (x) and transcriptional environment dynamics $\alpha(t)$ on the population statistics, we attempted the same noisy simulations using a linear form for $\frac{d\alpha}{dt_{slow}}$ without x or m dependence and did not find the same agreement. [275] This emphasizes that the nonlinear coupling between mechanical signaling and the dynamic evolution of the transcriptional environment is a fundamental conceptual ingredient which can explain both the disparate timescales of cellular adaptation and memory and captures non-normal population

130

statistics. The linear noise simulations can still result in zero, temporary, or permanent memory. However, the population statistics reflect the normal distribution of the noise applied, as seen by the agreement between the red model results and the black normal distribution CDF. While the available experimental data is limited, the same set of parameters using linear dynamics cannot qualitatively capture the experimental population distribution change with priming time nearly as well as the nonlinear dynamics, despite the same number of free parameters. The selection procedure for choosing the free parameters is discussed in Section 5.3.3.
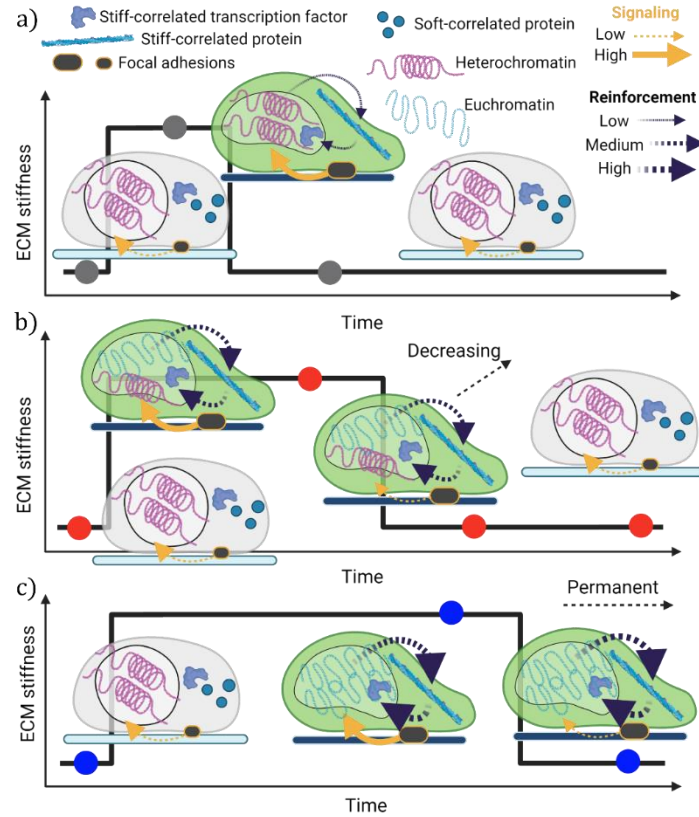
Figure 5.7 Summary of dynamic mechanical memory. **a)** At short priming times, mechanical signaling leads to cellular adaptation but does not persist for sufficient time to increase reinforcement, leading to no memory. **b)** At intermediate priming times, reinforcement increases with persisting mechanical signal. The transcriptional environment shifts enough to build temporary memory, but this reinforcement will slowly decay to erase memory once the mechanical signal is removed. **c)** At long priming times, reinforcement strength continues to grow with input mechanical signal and an adapting transcriptional environment. Reinforcement sustains without any mechanical signal, and the new phenotype persists if the substrate is changed (permanent memory).

We selected the data from the Yang et al. study on mesenchymal stem cells for direct comparison with our model since this is one of the few experimental studies to

explicitly track components of cellular mechanotransduction as a function of mechanical priming time. [215] While drawing quantitative comparisons across different experimental studies is difficult due to confounding variables such as cell lineage and growth media, we highlight several features of our model which appear in other studies (results summarized in **Table S1** in Ref. [275]). In our model, increasing ECM stiffness enough will always lead to cellular expression of a stiff phenotype on the scale of $\tau_{x\downarrow}$ and $\tau_{x\uparrow}$ irrespective of memory formation; our chosen values for these parameters are based on the adaptation time observed experimentally of ~1 hour. [226] The characteristic stiffness value m_0 which we use in **Figure 5.5** and **Figure 5.6** is consistent with the priming and memory stiffnesses used in other experiments in Ref. [275] **Table S1**. Short priming of ~1 day does not lead to appreciable memory in both our model and experiments [216], and temporary memory retention time is generally greater than or equal to the priming time across different experiments. In our phase diagram, reduction of α from region II to region III or region I erases permanent memory; experimentally, knockdown of miR-21 (a component of $\alpha(t_{slow})$) also erased permanent memory even after long priming. [214] Temporary memory development correlated with RUNX2 nuclear localization using stiff and soft substrates of 8 and 0.5 kPa after 7 days of priming was recently observed by Watson *et al.* in epithelial cells [218]; these values are similar to the data from Yang *et al.*, indicating that similar parameters in our model are translatable to a different cell type. Finally, in our model the reinforcement strength and acquired memory is cumulative; this agrees qualitatively with experiments which have investigated dynamic cyclical stretching as a

way to observe mechanical memory. [277,278] **Figure 5.7a-c** gives a schematic overview of the progression from external mechanical signal to self-sustaining mechanical memory with increased priming time by way of increased transcriptional reinforcement, spurred by mechanotransduction.

5.4.6 Simple Generalization for Analogous Soft-ECM Correlated Mechanical Memory

In this work, we focused on stiff-priming and stiff-correlated mechanical memory since these conditions are the most widely studied due to applicability in stem cell therapies for fibrosis and osteogenesis. However, cells can also develop analogous soft-correlated mechanical memory which can eventually lead to soft tissue generation such as neurogenesis with sufficient priming. [210] Our model is instantly generalizable to this case by reconstructing x as an averaged quantity of soft-activated phenotype components $(\vec{x} \rightarrow \vec{x}_{stiff}, \vec{x}_{soft})$ and inverting the scaled stiffness from $\frac{m}{m_0}$ to $\frac{m_0}{m}$ (**Figure 5.7a-c**). The phase diagram for soft-correlated memory and phenotypic activation is shown in **Figure 5.8** in and retains the three distinct regions which allow for no memory, temporary memory, and permanent memory depending on priming time. Recent experiments which primed adipose stem cells on 1 kPa substrates for two weeks found that temporary soft memory develops with similar persistence times (between one and two weeks) to stiff memory. [219] In contrast with stiff priming, nuclear YAP localization was not found to be a marker of soft-priming. This observation agrees well with our definition of the

134

mechanically correlated phenotype fingerprint vector $\vec{x}$; nuclear YAP is an element of the stiff-correlated $\vec{x}$ but not the soft-correlated $\vec{x}$. Using this simple, modular model
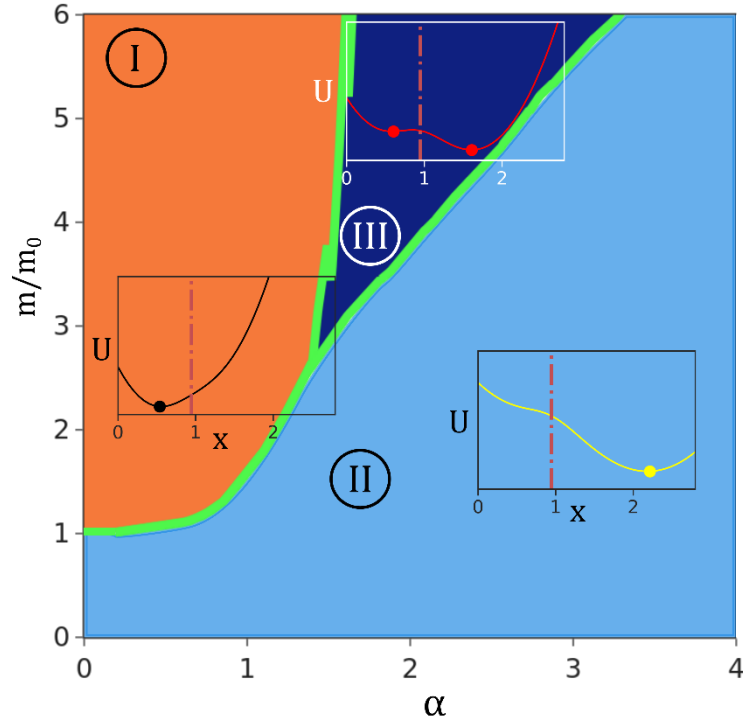
Figure 5.8 Analogous phase diagram of the model for soft-activated genes. In the model, the mechanoactivation profile / mechanical signaling is reversed by flipping $\frac{m}{m_0}$ to $\frac{m_0}{m}$, so that $\frac{dx}{dt}$ increases when stiffness is reduce. In this case, high x corresponds to activity of soft-correlated phenotypic genes and transcription factors. α now represents positive reinforcement for gene expression correlating with a soft phenotype.

framework, more complex models can be assembled which simultaneously consider soft and stiff memory and downstream consequences for differentiation.

5.5 Conclusion

The acquisition and maintenance of mechanical memory is a general phenomenon across different cell types and culture environments. [213–219,280] Balestrini et. al. cultured lung fibroblasts for two weeks on stiff (100 kPa, priming phase) substrates and found that they continued to express elevated fibrotic activity after being transferred to soft substrates (5 kPa, dissipative phase) for at least two weeks. A follow-up study by Li et al. under similar conditions identified miR-21 as a necessary molecule for long-time memory maintenance, indicating the role of transcriptional efficiency in memory regulation186. Some miRNAs can have half-lives on the scale of multiple days, which motivated our formulation of $\alpha(t_{slow})$ to conceptually include these non-coding RNA molecules. More recent experiments have focused on detailed changes of chromatin organization within the nucleus, confirming that epigenetic changes occur in response to mechanical signaling [217] and highlighting the role of the LINC complex as a direct, physical mechanosensory. [221,261,281] Additionally, we have recently shown that *epithelial* cell sheets primed on a stiff matrix for 3 days also store mechanical memory through nuclear YAP localization, which continues to enhance cell migration through enhanced pMLC expression and focal adhesion formation on soft matrix for 2-3 days. [216]

In developing our model, we sought to synthesize and distill the phenomenological observations from these experiments and related studies covering the impact of mechanics on lineage specification, which has not been accomplished by existing models to our

136

knowledge. Li et. al. proposed a reservoir model along with their identification of miR-21 as a memory regulator, where priming leads to production of memory keepers which slowly dissipate after priming halts. This model alone does not explain the timescale disparity between mechanical adaptation and development of memory. Mousavi et al. and Peng et al. proposed two different mechanically activated differentiation models based on population dynamics and gene regulatory networks, but these models do not capture the variable rates of memory dissipation observed in experiments. These models rely on ~20 and ~40 free kinetic parameters, respectively, yet do not account for key qualitative features of the memory phenomena. Our model uses 8 unique free parameters, which sacrifices resolution on specific biological mechanisms but allows us to identify that a simple nonlinear coupling between signaling and transcriptional evolution is sufficient to capture the phenomenological features of cellular plasticity.

The continuous range of cellular plasticity persistence time from zero (no memory, **Figure 5.7a**) to permanent (lineage specification, **Figure 5.7c**) is unique when compared to other physical memory systems, which often either exhibit permanent memory or no memory. Although early studies of lineage specification viewed this process as unidirectional (such as the traditional Waddington landscape), the targeted reversibility of plasticity under the right conditions is also a unique physical feature. The traditional Waddington landscape identifies specific branch points which split cells into separate wells representing stable phenotypes. [233] Our model generalizes this picture by showing that

both the Waddington landscape surface and the rate at which the cell progresses down each well can be altered by external stimuli such as stiffness. This 'graduated reversibility' may function biologically to make the cell more resilient to local short-term fluctuations in environment, while still allowing for long term, correlated population shifts in response to persistent environmental cues.

Predicting the memory response of cells to their mechanical environment has significant implications for designing cell-based therapy and studying other cellular mechanisms *in vitro*. Based on our model, we predict that small changes in priming stiffness or priming time can have large consequences on the retention time of developed phenotypes due to the nonlinearity of slow-evolving components. Our phase diagram indicates that recovery of stem-like, soft phenotypes can be enhanced after priming by reducing the stiffness of the recovery substrate, extending the range of region III which allows for memory dissipation. However, beyond a certain point, mechanical signal alone will not lead to phenotype reversal due to formation of permanent memory. Measuring the extent of priming may require nuclear information and not just data on signal activity, since the timescale of signaling is independent of the timescale of memory development. External methods to change α, such as Yamanaka factors or changes in growth media, can overwrite the natural permanent persistence of the stiff phenotype in these situations. In future work, we anticipate that this model framework for mechanical memory can be extended to include a chemical axis, which can be used to consider more general cases of

138

cell differentiation and coupling between chemical and mechanical contributions to memory acquisition and retention.

Chapter 6 Conclusions and Future Directions

6.1 Summary

In this thesis, our main goal was to develop new multiscale frameworks to predict physical phenomena spanning multiple length and time scales. This goal was achieved across a wide range of materials systems using physics-based, first-principles theoretical frameworks to inform custom continuum and machine learning models, which were derived and solved on geometries relevant to the largest length or time scale. We validated each model approach by recovering results from multiple sets of experimental data or *ab initio* calculations, which demonstrate the predictive capability of our approach.

In **Chapter 2**, we explore how lattice-matched interfaces can lead to localized quantum states in a 2D host material with different scaling behavior than conventional quantum dots. The linear scaling of the confinement energy with the dot size arises from the planar hexagonal symmetry and corresponding band structure of the monolayer materials, which contain significant linear contributions to the direct-gap low energy dispersion around the K point. The existence of confined quantum bound states is not guaranteed as it would be in conventional semiconductor quantum dot which does not contain these linear dispersion contributions, and we analytically develop a phase diagram

relating calculable band structure quantities and the existence of bound states. For more complex but realistic dot geometries such as triangles and hexagons, our numerical approach provides experimental guidance for synthesis to realize observable bound states across a range of materials. These bound states can theoretically emit single photons with a precise energy and phase for applications in quantum computing and photonics.

Moving to non-lattice-matched crystal-molecule interfaces in **Chapter 3,** we investigate how surface strain and interfacial dipole moments can give rise to an energetic competition that affects the stability of ordered phases at different compositions. At large scales, interfacial dipole layers arising in devices such as p-n junctions are often modeled as uniform charge sheets, since this is how they appear electrostatically at large distances. However, for modern applications such as quantum wells and nanoscale semiconductor devices, the corrugations of the interfacial dipole layer can give rise to non-zero electric fields away from the interface which depend on the length scale of the dipole lattice. This can affect the stability of nanoscale composite structures as we illustrate *via* a competition with interfacial strain, and it can also couple to electrically sensitive properties at the interface. The continuum model that we propose can also be used to investigate the intercalation limits of ions in layered materials under mechanical strain, since these ions often pack into lattices with significant charge transfer.

In **Chapter 4**, we expand to considering many surface-adsorbate complexes with machine learning models to predict the impact of strain on the interaction between the

140

surface and the adsorbate. Surface-adsorbate complexes are difficult to study using conventional atomistic methods due to abrupt symmetry breaking, but these structures contain the fundamental interactions underpinning the synthesis of industrially valuable chemicals. Machine learning can help accelerate evaluation of these complexes, but requires a sufficiently expressive representation to distinguish subtle structural differences such as surface facet, adsorption site, and surface composition. Our graph neural network approach can simultaneously distinguish the strain response for two different adsorbates on the same surface and the same adsorbate on two different surfaces. We identify Cu_xS_{1-x} alloy catalysts as a promising strain engineerable platform in the context of ammonia synthesis. With community-based efforts to extend these datasets and model sizes, our approach can be used repeatedly to enable catalyst discovery considering both desired and undesired reaction pathways together.

Finally in **Chapter 5**, we develop a continuum model that covers multiple time scales to explain unique features of the long-term memory that stem cells can acquire about the substrates that they interface with. Predicting the impact of culture conditions on acquired cellular memory is critical to developing stem cell therapies, which require cells to plastically change at the therapeutic destination. Successful stem cell therapies will circumvent many challenges of integrating foreign materials as therapeutics, since a person's own cells can be engineered to address a specific problem. Using our minimal model with one set of parameters corresponding to real experimental conditions, we are

able to capture two distinct trajectories of mechanical memory retention in a cell population; one temporary and one permanent. The model framework allows for improved accuracy through incorporation of molecular detail using mechanosensitive kinetic relationships, which require additional data to inform but are an area of recent intense research focus.

We believe that these studies have introduced new concepts, predictions, and software to the scientific community, assisting in bridging the gap between traditional simulations and experiments.

6.2 Outlook

There is plenty of untapped potential for multiscale modeling to have increasing impact on innovation and optimization of materials platforms going forward. While individual simulation methods have been exhaustively pursued over all but the most exotic materials, in multiscale modeling the synthesis of methods and physical concepts can lead to emergent phenomena that extend our observations and understanding of low energy physics. This is especially true for bridging the gap between the idealities *in silico* world and the complexities *in vita*, where interfaces between different materials plays a major role (**Figure 6.1**). As the demand for new materials with high performance criteria accelerates to solve dire technological challenges such as climate change, multiscale
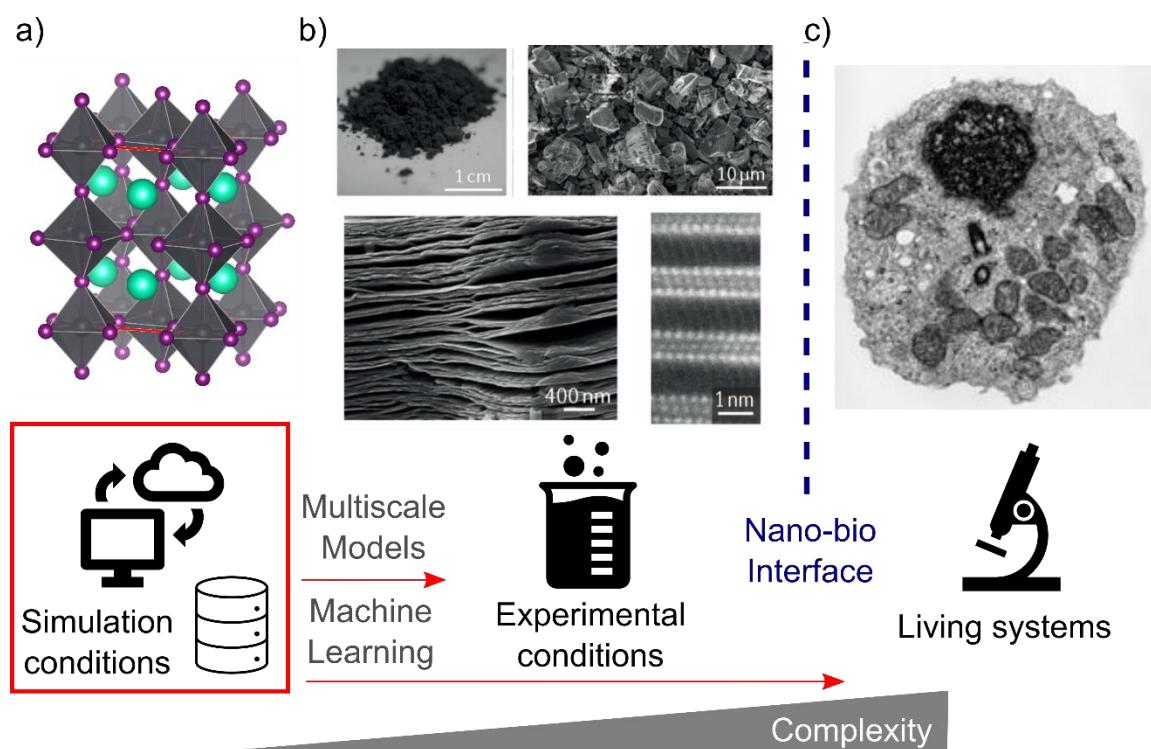
Figure 6.1 a) Simulation representations of materials and conditions are idealized compared to experiments. Looking forward, multiscale modeling and machine learning can synthesize many different simulation results to bridge simulation-experimental gaps. **b)** Images of MXene structure at multiple length scales highlight complexity introduced by hierarchical changes in structure at each scale. Reproduced from [295]. **c)** Transmission electron microscope of a white blood cell; the complexity of living cells and their interfaces with the environment requires inherently multiscale models. Reproduced from BBC.

models will become increasingly important to navigate the high dimensional spaces of materials design many orders of magnitude faster and cheaper than experimental trial and error.

Despite the theoretical potential of computational materials science, these predictions mean little if they cannot be realized experimentally. We anticipate that

143

upcoming work will demonstrate the realization of Dirac fermion bound states in transition metal dichalcogenides as predicted in **Chapter 2**, and we believe that this offers a great opportunity to analyze the differences between the model predictions and experimental measurements. This model made several simplifying assumptions (perfectly sharp interfaces and neglecting excitonic effects) that are likely to break down in a real system; building on these results moving forward could be a major step towards controlling individual quantum states in 2D materials.

Translating computational predictions to experimental conditions is challenging especially when considering heterostructure materials, as making physics-derived models more accurate often incurs exponentially larger computational cost. We are optimistic about the application of machine learning to address this problem, as data driven models can take advantage of the rapidly growing repository of computed materials data to form a mapping function between the simulation and experiment worlds (**Figure 6.1**). While significant hype exists around developing autonomous black-box artificial intelligence systems, we find it more likely that models built on top of curated first-principles and other physically generated data can succeed by internalizing correlations from physical priors and attempting to fill in the missing gaps. Incorporating these physical constraints can reduce the data requirements for successful models as we showed in **Chapter 4**. Accomplishing this requires a field-wide effort to generate, document, and collate datasets in transferable formats, and significant progress is being made on this front for both

computational and experimental data. [282,283] Although not presented here, we also studied materials growth using similar multiscale models to those in this thesis, and we believe that this a promising area for machine learning assisted translation between computational predictions and experimental observations. [284–287]

Finally, we see the nano-bio interface as a major frontier for multiscale modeling and materials interface engineering (**Figure 6.1**). Tremendous progress has been made in rapid, efficient data collection characterizing cellular genomes and phenotypes at both single-cell and population levels. However, the causal relationships between the cellular nano-/micro- environment and cellular behavior/outcomes are very poorly understood. These relationships are complicated by noisy processes over multiple length and time scales, as we demonstrate in **Chapter 5**. There is strong evidence that cell function significantly depends on the mechanical and electrical properties of the solid or gel phase cell surroundings, whereas previous work has focused heavily only on the chemistry of cellular media. Developing predictive models and phase diagrams of cell phenotype based on engineerable external parameters would accelerate therapeutic design and bioengineering for synthetic biology applications. Given the physical complexity of these systems, multiscale modeling at the nano-bio interface is sure to play a vital role in achieving these goals.

APPENDIX

S2.1: Derivation of Equation 2.4

Following the derivations for massless [71] and massive [288] Dirac fermions in graphene for a radially symmetric potential, $V(r)$, in two dimensions, we start with the massive Dirac equation given by

$$H\Psi = \big(E - V(r)\big)\Psi \tag{S2.1}$$

where $H = -i\hbar v_D\big(\sigma_x\partial_x + \sigma_y\partial_y\big) + \sigma_z m v_D^2$, Ψ is a bispinor, σ_x and σ_y are 2 x 2 Pauli matrices, v_D is the Dirac velocity, and m is the effective mass. The band gap, Δ, the lattice parameter, a, and the hopping parameter, t, are related to the quantities in H *via* $\Delta = 2mv_D^2$ and $at = \hbar v_D$. It is important to note that for the transition metal dichalcogenide systems we are describing, $\Delta > 0$ and therefore $m > 0$, in contrast to graphene.

Rewriting H in polar coordinates and representing it as a 2 x 2 matrix gives the massive Dirac Hamiltonian

$$H = \begin{bmatrix} \dfrac{\Delta}{2} & -iate^{-i\theta}\left(\partial_r - \dfrac{i}{r}\partial_\theta\right) \\ -iate^{i\theta}\left(\partial_r + \dfrac{i}{r}\partial_\theta\right) & -\dfrac{\Delta}{2} \end{bmatrix} \tag{S2.2}$$

Assuming a separable solution to (1), we write the bispinor as

$$\Psi = \frac{1}{\sqrt{r}}\begin{pmatrix} f_{l-1}(r)e^{i\left(l-\frac{1}{2}\right)\theta} \\ g_{l-1}(r)e^{i\left(l+\frac{1}{2}\right)\theta} \end{pmatrix} \tag{S2.3}$$

for the angular quantum number $l = 0, \pm 1, \pm 2, \dots$ and two radial components, $f_{l-1}(r)$ and $g_{l-1}(r)$.

Evaluating the radial parts of (S2.1) and (S2.2) gives the coupled differential equations

$$\frac{df_{l-1}(r)}{dr} - \frac{l}{r}f_{l-1}(r) - \frac{i}{at}\left(E - V(r) + \frac{\Delta}{2}\right)g_{l-1}(r) = 0 , \qquad \text{(S2.4)}$$

$$\frac{dg_{l-1}(r)}{dr} + \frac{l}{r}g_{l-1}(r) - \frac{i}{at}\left(E - V(r) - \frac{\Delta}{2}\right)f_{l-1}(r) \qquad \text{(S2.5)}$$

$$= 0$$

Solving (S2.4) for $g_{l-1}(r)$ gives

$$g_{l-1}(r) = -\frac{iat}{E - V(r) + \frac{\Delta}{2}}\left(\frac{df_{l-1}(r)}{dr} - \frac{l}{r}f_{l-1}(r)\right) \qquad \text{(S2.6)}$$

We define the finite potential well

$$V(r) = \begin{cases} V_0, & r > r_0 \\ 0, & r \le r_0 , \end{cases} \qquad \text{(S2.7)}$$

such that inside the well, we obtain a second-order differential equation for $f_l(r)$ from plugging (S2.6) into (S2.5):

147

$$\frac{d^2 f_l(r)}{dr^2} + \left(\frac{\left(E - \frac{\Delta}{2}\right)\left(E + \frac{\Delta}{2}\right)}{(at)^2} - \frac{l(l+1)}{r^2} \right) f_l(r)$$

$$= 0 \tag{S2.8}$$

This is simply the Bessel differential equation, which for the region containing the point $r = 0$ has the solution

$$f_l(r) = A\big(J_l(\alpha_W r)\big) \tag{S2.9}$$

for an arbitrary constant, A, the Bessel function of the first kind, J_l, and

$$\alpha_W = \frac{\sqrt{E^2 - \left(\frac{\Delta}{2}\right)^2}}{at} \tag{S2.10}$$

Likewise $g_l(r)$ inside the well is given by

$$g_l(r) = -\frac{at\alpha_W}{E + \frac{\Delta}{2}} \big(f_{l+1}(r)\big) \, . \tag{S2.11}$$

Outside the well, where $V(r) = V_0$, (S2.8) is modified so that $E \rightarrow E - V_0$ and the physical solutions (where the wave function is normalizable at infinity) are

$$f_l(r) = B\big(Y_l(\alpha_V r)\big) \, , \tag{S2.12}$$

$$g_l(r) = \frac{at\alpha_V}{V_0 - E - \frac{\Delta}{2}} \left(f_{l+1}(-r) \right), \tag{S2.13}$$

where B is a constant, Y_l is the Bessel function of the second kind, and $\alpha_V = \frac{\sqrt{E^2 - \left(\frac{\Delta}{2}\right)^2 - 2EV_0 + V_0^2}}{at}$.

We consider $l = 0$ states because we are interested in only the ground state. Imposing the boundary condition that Ψ is continuous at $r = r_0$ then gives the transcendental equation

$$\frac{Re[Y_0(-r_0\alpha_V)]}{J_0(r_0\alpha_W)} = \frac{i\alpha_V}{\alpha_W} \frac{E + \frac{\Delta}{2}}{V_0 - E - \frac{\Delta}{2}} \frac{Im[Y_1(-r_0\alpha_V)]}{J_1(r_0\alpha_W)}, \tag{S2.14}$$

which is Equation (2.4) in the manuscript. Solutions of E to this equation correspond to the minimum angular momentum states which are localized in the well. The real part of Y_1 and imaginary part of Y_0 are neglected because they do not decay to 0 as $r \to \infty$; these correspond to the Klein tunneling solutions.

If Δ is finite, as V_0 goes to infinity for a fixed r_0, the expected solutions for the infinite potential well are recovered. If Δ is taken to zero at small V_0, the massless Dirac fermion solution in graphene is recovered and there are no bound states; [71] taking V_0 to infinity at $\Delta = 0$ corresponds to the infinite mass boundary condition. [41] Finally, as r_0 goes to infinity at fixed V_0 and Δ, the bound state energy asymptotically approaches the bottom of the potential well, in agreement with the traditional Schrodinger behavior.

We can simplify Eq. S2.14 by setting $E = 0$ and recasting the transcendental in terms of the dimensionless variables $x = \frac{\Delta r_0}{at}$ and $y = \frac{V_0}{\Delta}$. We further define $y' = -\sqrt{y^2 - \left(\frac{1}{2}\right)^2}$ for convenience. Making the substitution and doing some simple algebra leads to the dimensionless form

$$\frac{Re[Y_0(xy')]}{J_0\left(\frac{ix}{2}\right)} = \frac{-y'}{y - \frac{1}{2}} \frac{Im[Y_1(xy')]}{J_1\left(\frac{ix}{2}\right)} \tag{S2.15}$$

S2.2: Tight-binding model and expanded $k \cdot p$ model for comparison.
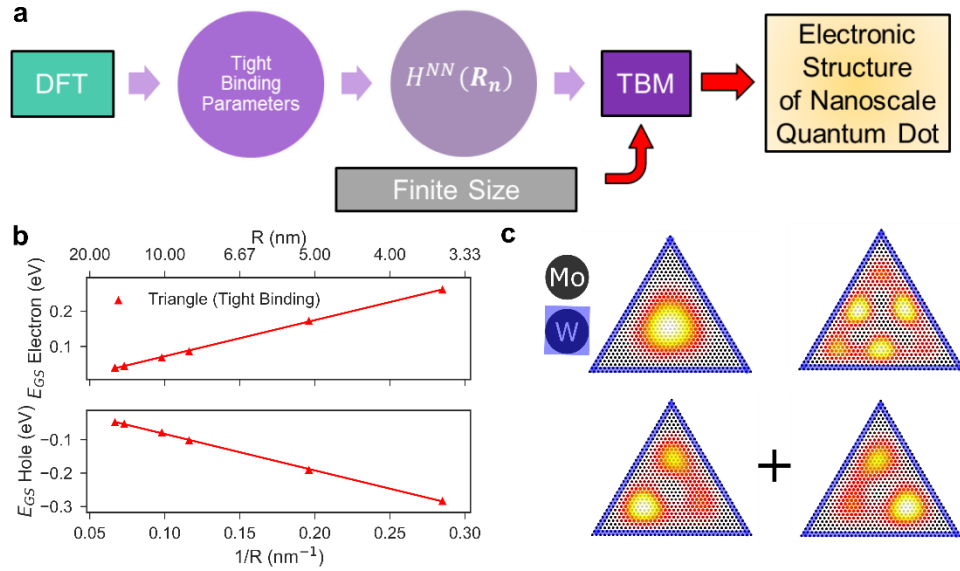
Figure S2.1. Tight-binding model results for finite size scaling of electron and hole ground state energies in a triangular quantum dot. **a)** Schematic of workflow for obtaining electronic structure of quantum dot from tight-binding. **b)** Electron (top) and hole (bottom)

ground state energy in a triangular quantum dot as a function of side length. **c)** Ground and excited state wave functions from tight-binding model.

We repeat the analysis in Chapter 2.4.2 using a three-band tight-bonding model [62] of a triangular MoS_2 quantum dot [67] with an outer edge of WS_2 atoms that forms the finite electron confining well. We recover the same characteristic ground state energy scaling described by Eq. 2.5 in the tight binding model results (Figure S2.1b). The computed wavefunctions (Figure S2.1c) agree with those from the continuum model, although the inclusion of an additional d band and spin-orbit coupling in the tight-binding model leads to degeneracy breaking in the excited states. Importantly, while $\boldsymbol{k} \cdot \boldsymbol{p}$ is a long wavelength theory that is expected to break down at small length scales, the tight-binding approach describes the quantum dot system at these length scales. The continuum approach is well-suited for device-relevant length scales, so there are no apparent gaps in our multiscale approach. Independently, we verify the validity of the truncation of the $\boldsymbol{k}$ expansion to second order by measuring the magnitude of the correction introduced by $H_{kp}^2(\boldsymbol{k})$ as a function of dot size (Figure S2.2). As expected, the higher order terms are more important for smaller dot sizes, and for a 4 nm MoS_2/WS_2 triangular dot, the second order correction reaches a maximum of 8.5 meV, which is well within the perturbative regime. At small dot sizes in the tight-binding regime, the higher order terms in the continuum model will affect the quantitative energy values, but overall trends such as the geometry-critical size relationships are minimally impacted.
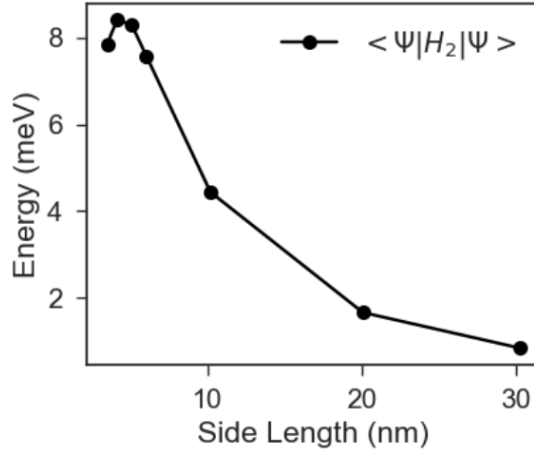
Figure S2.2. Magnitude of $H_{kp}^2(\boldsymbol{k})$ corrections to the ground state energy as a function of dot size for triangular geometries. The perturbative regime of $H_{kp}^2(\boldsymbol{k})$ overlaps with the accessible length scales for the tight-binding description.

S3.1: Derivation of the Electrostatic Energy Term
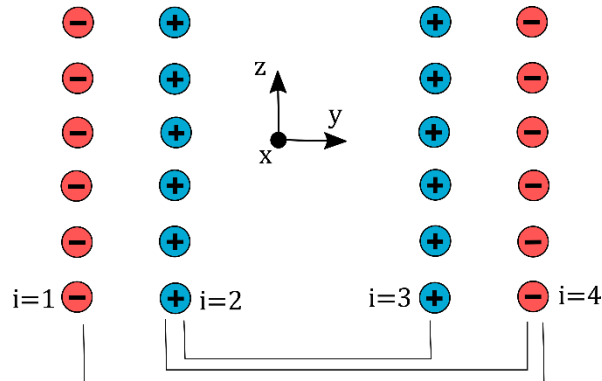
Figure S3.1. Schematic opposing lattices of point charges arranged to simulate interacting interfacial dipoles. The interactions counted in the model are shown using the black connectors; the $i = 2 : i = 4$ interaction is multiplied by 2 by symmetry.

Following previous works, we show the calculation of the electrostatic energy of two opposing dipole lattices. [289,290] The electrostatic energy between two parallel uniformly charged sheets which are infinitely periodic in their parallel dimensions is zero, while the energetic interactions between two individual dipoles at long distances falls off

as $\sim \frac{1}{r^3}$, where r is the distance between the dipoles. For two infinite, parallel, and oppositely oriented point-charge dipole lattices, we expect that the electrostatic energy will fall between these limits. We start by solving the Poisson equation

$$\nabla^2 \phi(x,y,z) = -\frac{\rho(x,y,z)}{\varepsilon_r} \tag{S3.1}$$

where ϕ is the electric potential, ρ is the charge density, and ε_r is the static permittivity of the medium. Focusing on the N-dependent interaction, we break the dipole arrays into 4 parallel sheets of point charge square lattices with periodicity a_{dip}, 2 with positive charges and 2 with negative charges, such that the total system is charge neutral. We set the y dimension to be perpendicular to the sheet, consistent with the atomistic convention, so that the total charge density $\rho(x,y,z) = \sum_{i=1}^{4} \sigma_i(x,z)\delta(y - y_i)$, where the index i enumerates each individual sheet at position y_i and $\sigma(x,z)$ is the in-plane charge density. Due to the principle of superposition, we can add the sum over sheets back in later and focus on a single sheet for now.

$\sigma(x,z)$ is composed of a charge motif which is periodic on the 2D lattice; to account for the periodicity, we will express the in-plane charge density as a Fourier series over the reciprocal lattice vectors $\vec{k}$ and solve the Poisson equation in Fourier space:

$$\sigma(x,z) = \sum_{k_{xz}} \tilde{\sigma}(k_x, k_z) \exp(i k_{xz} \cdot r_{xz}) \tag{S3.2}$$

$$\tilde{\sigma}(k_x, k_z) = \frac{1}{A} \iint_{-\frac{a_{dip}}{2}}^{\frac{a_{dip}}{2}} dx\, dz\, \sigma(x,z) \exp(-i k_{xz} \cdot r_{xz}) \tag{S3.3}$$

$$\tilde{\phi}(k_x, k_y, k_z) = \frac{\tilde{\rho}(k_x, k_y, k_z)}{(k_x^2 + k_y^2 + k_z^2)\varepsilon_0} = \frac{\tilde{\sigma}(k_x, k_z) \exp(-i k_y y_i)}{(k_x^2 + k_y^2 + k_z^2)\varepsilon_0} \tag{S3.4}$$

153

Since we want to know the potential in terms of the inter-sheet distance, we transform k_y back to y using the Cauchy integral formula for a Lorentzian to get the mixed expression

$$\tilde{\phi}(k_x, y, k_z) = \frac{\tilde{\sigma}(k_x, k_z) \exp(-|y||\vec{k}|)}{2|\vec{k}|\varepsilon_0} \tag{S3.5}$$

This equation diverges at $k = 0$, *i.e.* the long wavelength contribution which corresponds to the average charge density of the sheet σ_0. Since we know that the potential due to a uniform charge sheet is linear with distance and proportional to the average charge, we can separate the $k = 0$ component when substituting for $\tilde{\sigma}(k_x, k_z)$. Adding back in the sum over 4 parallel sheets:

$$\phi(x, y, z) = \phi_0 - \frac{1}{2\varepsilon_0} \sum_{i=1}^{4} \sigma_0 |y - y_i|$$
$$+ \sum_{k_{xz} \neq 0} \frac{\exp(ik_{xz} \cdot r_{xz})}{2|\vec{k}|\varepsilon_0} \sum_{i=1}^{4} \tilde{\sigma}_i(k_x, k_z) \exp(-|y \tag{S3.6}$$
$$- y_i||\vec{k}|)$$

With an expression for the potential, we can then calculate the electrostatic potential energy per unit cell of the infinite sheets using the relation $U_E = \frac{1}{2} \int_V \rho\phi dV = \frac{1}{2} \int\int_{-\frac{a}{2}}^{\frac{a}{2}} dx \, dz \int dy \, \rho\phi$. Writing out each term from (6) in this integral:

$$\frac{1}{2}\phi_0 \int\int dA \, dy \, \sigma(x, z)\delta(y - y_i) = \frac{A}{2}\phi_0 \sum_i \sigma_{0(i)}$$

$$\frac{-1}{4\varepsilon_0} \sum_{i,j} \int\int dA \, dy \, \sigma_i(x, z) \, \delta(y - y_i) \, \sigma_{0(j)} |y - y_j| = -\frac{A}{4\varepsilon_0} \sum_{i,j} \sigma_{0(i)} \sigma_{0(j)} |y_i - y_j|$$

$$\frac{1}{2}\int\int dA \, dy \sum_i \sigma_i(x, z)\delta(y - y_i) \left[\sum_{k_{xz} \neq 0} \frac{\exp(ik_{xz} \cdot r_{xz})}{2|\vec{k}|\varepsilon_0} \sum_j \tilde{\sigma}_j(k_x, k_z) \exp(-|y - y_j||\vec{k}|) \right]$$

154

$$= \frac{1}{4\varepsilon_0} \iint dA \, dy \sum_{k_{xz}\neq 0} \sum_i \frac{\sigma_i(x,z)\exp(ik_{xz}\cdot r_{xz})}{|\vec{k}|} \sum_j \sigma(k_x,k_z)\delta(y-y_i)\exp(-|y$$

$$- y_j||\vec{k}|)$$

$$= \frac{1}{4\varepsilon_0} \iint dA \, dy \sum_{k_{xz}\neq 0} \sum_{i,j} \tilde{\sigma}_\iota(k_x,k_z)^*\tilde{\sigma}_j(k_x,k_z) \; \delta(y-y_i)\frac{\exp(-|y-y_j||\vec{k}|)}{|\vec{k}|}$$

$$= \frac{A}{4\varepsilon_0} \sum_{k_{xz}\neq 0} \sum_{i,j} \tilde{\sigma}_\iota(k_x,k_z)^*\tilde{\sigma}_j(k_x,k_z)\frac{\exp(-|y_i-y_j||\vec{k}|)}{|\vec{k}|}$$

Adding the final right hand side terms together gives the total electrostatic energy expression:

$$U_E = \frac{A}{2}[\phi_0 \sum_i \sigma_{0(i)} - \frac{1}{2\varepsilon_0}\sum_{i,j} \sigma_{0(i)}\,\sigma_{0(j)}\left|y_i - y_j\right|$$

$$+ \frac{1}{2\varepsilon_0}\sum_{k_{xz}\neq 0}\sum_{i,j} \tilde{\sigma}_i(k_x,k_z)^*\tilde{\sigma}_j(k_x,k_z)\frac{\exp\left(-\left|y_i - y_j\right||\vec{k}|\right)}{|\vec{k}|}]$$

(S3.7)

  This expression rapidly simplifies for the desired case of opposing dipole sheets. The first term related to the potential integration is zero since the system is overall charge neutral (sum of the sheet averages = 0). The second term (linear term due to the average density) also drops out because the dipole sheets are oriented opposite and parallel to each other, with equal charge – this is the same result of zero potential for uniform and equally charged sheets. In the last term, we select only some of the summations over sheet indexes i and j. When $i = j$, the energetic contribution corresponds to the self-energy of assembling that charge sheet; in our model, this is captured by the surface energy. Since we are only interested in cross-surface interactions, we neglect terms with $i = j$. We also neglect terms with neighboring i,j, since the formation of the surface dipole is also accounted for by the surface energy. We neglect other periodic interactions in the y direction because these are accounted for in the interdigitation energy. Next, since the sum is symmetric about

155

interchange of i, j, we can extract a factor of 2 such that the total interacting sheet energy is:

$$U_E = \frac{A}{2\varepsilon_r} \sum_{k_{xz} \neq 0} \sum_{i<j} \frac{\widetilde{\sigma}_i(k_x, k_z)^* \widetilde{\sigma}_j(k_x, k_z)}{|\vec{k}|} \exp\left(-\left|y_i - y_j\right| |\vec{k}|\right) \qquad \text{(S3.8)}$$

In order to evaluate $\widetilde{\sigma}$, we must choose a charge motif for the sheet. To avoid divergences associated with infinitesimal point charges and ensure the periodic component is separable from the perpendicular dimension, we choose a normalized 2D Gaussian disk $\sigma(x, z) = \frac{Q}{2\pi d^2} \exp\left(-\frac{x^2 + z^2}{2\rho_0^2}\right)$ containing total charge Q and extent ρ_0, $\rho_0 \ll a_{dip}$. Then,

$$\widetilde{\sigma}(k_x, k_z) = \frac{Q}{A} \exp\left(-\frac{(k_x^2 + k_z^2)\rho_0^2}{2}\right)$$

Finally, the energy U_E is converted from the fictitious dipole unit cell to eV/atom by dividing by the volume of the dipole unit cell $A|y_i - y_j|$ and then the atomic density of the atomic unit cell corresponding to one dipole unit cell. In practice, the expressions for $\widetilde{\sigma}$ and U_E are evaluated numerically using the discrete fast fourier transform (FFT) functions available in SciPy and converged to appropriate grid resolutions.

a)

b)
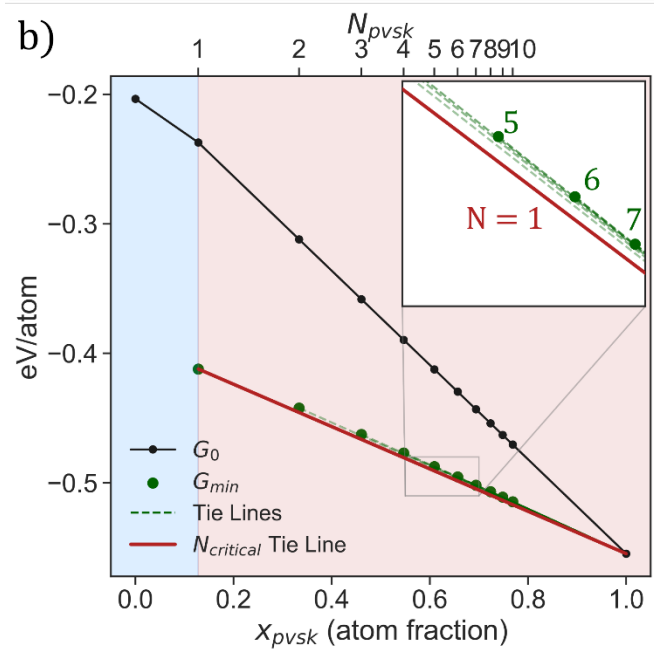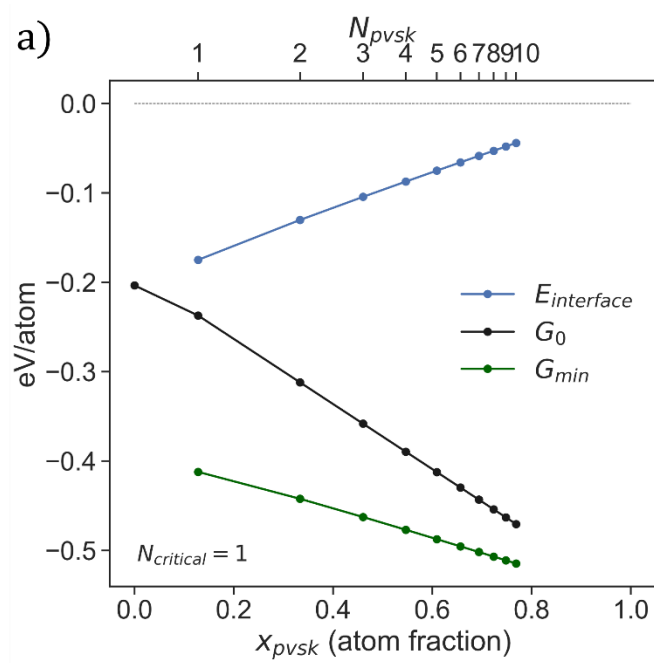
Figure S3.2 a) Component curves for G_{min} without U_E included in ΔH_{mix}. The independent bulk formation energy (black) and interfacial energy (blue) combine to give the energy of the ordered phases (green). **b)** Determination of N_{crit} without interfacial electrostatic interactions. The $N = 1 + N = \infty$ two-phase mixture is preferred across all compositions. This is determined by drawing tie lines between the bulk perovskite phase and all ordered phases, finding the two-phase mixture thermodynamically favored over other single-phase compounds.

S4.1: Dataset Characterization and Model Metrics

Table S4.1: List of M elements for Cu_xM_{1-x} alloys and all adsorbates in the strain-generated

training set.

Adsorbate (* indicates adsorbing atom)	Alloy Elements
*H	Al
*O	S
*C	Y
*N	Hf
*OH	Pd
*CH	Si
*NH	Zr
*NO	Sc
*NH$_2$	Au
*CHOH	Cl
*N$_2$	Ru
*CN	Zn
*OH$_2$	Sb
*NHNH	Ca
*ONNH$_2$	Ag
*NONH	Te
*ONH	Ge
*N*NH	Cu
*CH$_2$	

*OCH$_3$	
*NO$_2$	
*NH$_3$	
*CH$_2$*O	
*CH$_2$OH	
*NO$_3$	
*CH$_3$	
*CH$_4$	

Table S4.2: Dataset splits for classification task.

Class	Dataset %
$-\Delta$ ($\Delta E_{ads} < -25$ meV)	24.5
Z ($|\Delta E_{ads}| < 25$ meV)	54.1
$+\Delta$ ($\Delta E_{ads} > 25$ meV)	21.4

Table S4.3: Model metrics on test data. All models are trained on the same dataset; for the ensemble linear model, the training set is grouped by adsorbate and alloy composition (for example, Cu$_3$Al and CuAl catalysts with *NH adsorbate are grouped together) and a linear regression is fit for the target ΔE_{ads} vs. the area strain $\frac{A-A_0}{A_0}$ within the group.

Model	Task	Metric	Value
Ensemble linear	Regression	Mean absolute error	0.17 eV
Ensemble linear	Regression	Mean R^2	-45.03
GNN	Regression	Mean absolute error	0.08 eV
GNN	Regression	R^2	0.31
Ensemble linear	Classification	F1 score	0.58
Ensemble linear	Classification	Accuracy	0.58
GNN	Classification	F1 score	0.86
GNN	Classification	Accuracy	0.85

Table S4.4: GNN hyperparameters.

159

Parameter Name	Value	Notes
Hidden_channels	24	DimeNet++
Out_emb_channels	12	DimeNet++
Num_blocks	3	DimeNet++
Num_radial	5	DimeNet++
Num_spherical	4	DimeNet++
Num_before_skip	1	DimeNet++
Num_after_skip	2	DimeNet++
Num_output_layers	3	DimeNet++
Strain_projection_channels	16	StrainBlock
Num_strain_layers	2	StrainBlock
Strain_final_dimension	16	StrainBlock
Batch_size	8	Training parameter
Lr_initial	0.001	Training parameter
Lr_gamma	0.1	Training parameter
Lr_milestones	60,000; 120,000	Training parameter
Warmup_steps	1,000	Training parameter
Warmup_factor	0.2	Training parameter
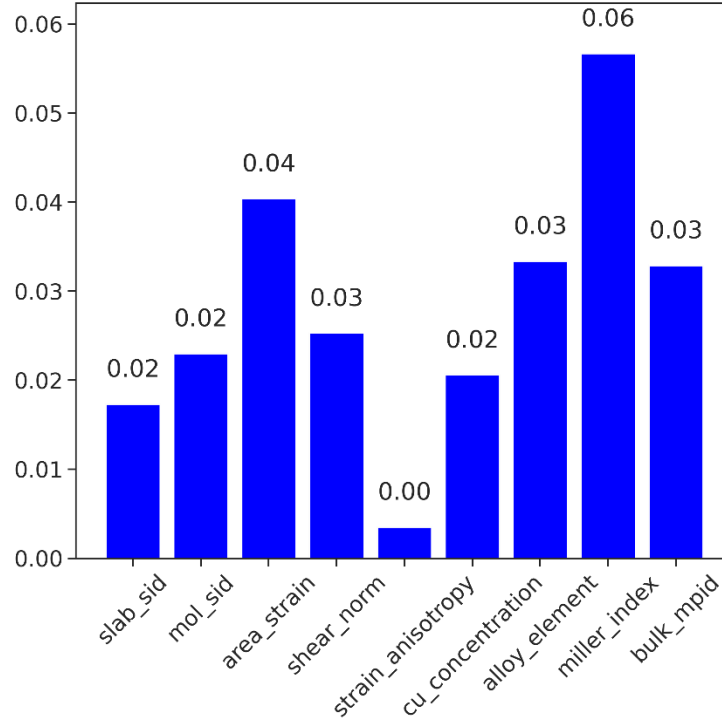
Figure S4.1. Pairwise Pearson correlation coefficients of different manually generated features across strain and composition with the change in adsorption energy for a particular strain ΔE_{ads}.

S5.1 Generalized Model for Dynamic Self-Reinforcing Mechanosensitivity

Consider a vector variable $\vec{x}$ where elements $x_{i=1..n}$ represent functionally active concentrations of stiff-activated proteins and transcription factors. For a cytoskeletal protein, x_i corresponds to the steady-state concentration which emerges from synthesis and degradation. Examples of stiff-correlated cytoskeletal proteins include F-actin (or α-SMA), vinculin, and integrins. For transcription factors, x_i refers to a transcriptionally eligible concentration, which includes the steady-state level of nuclear localization. Examples of transcription factors with well-known stiff-correlated nuclear localization include

YAP [244,245], MKL-1 [229,246], and RUNX2 [247,248]; nuclear localization is necessary for transcription factor activity due to the possibility of co-activation requirements. Enzymes which modify the epigenome such as HDAC and HAT are also included as elements of $\vec{x}$, as epigenetic changes demonstrate mechanosensitive activity patterns and alter chromatin organization [217]. $\vec{x}$ is a fingerprint state vector for the mechanical phenotype of the cell. For each element of $\vec{x}$, we can write a linear steady-state rate equation

$$\dot{x_\iota} = k_{\uparrow i}(m)\left(x_i^{ref} - x_i\right) - k_{\downarrow i}(m)x_i + \sum_j c_{ij}(m)x_i x_j \qquad \text{(S5.1)}$$

where $\dot{x_\iota} = \frac{dx_i}{dt}$, m is the ECM stiffness, $k_{\uparrow i}(m)$ is the stiffness-dependent rate of nuclear import or protein synthesis for component i, and $k_{\downarrow i}(m)$ is the stiffness-dependent rate of nuclear export or protein degradation for component i. $\overrightarrow{x^{ref}}$ with elements $x_{i=1..n}^{ref}$ is a vector of arbitrary reference concentrations such that the steady-state concentration $x_i = x_i^{ref}$ when stiffness $m = m_0$. c_{ij} are elements of the cooperativity matrix C which we define to be the matrix of activity coefficients which describe the degree of cooperation or anti-cooperation between different elements of $\vec{x}$. Additional cooperativity matrices corresponding to more complex interactions between elements of $\vec{x}$ can be defined and added to Eq. S5.1. This defines a coupled set of rate equations for each mechanosensitive phenotype marker of the cell which has a unique steady state depending on the value of m.

Next, we consider contributions from positive feedback loops to the dynamics of each element of $\vec{x}$. Positive feedback loops arise from active transcription which assists phenotypic shifts that promote further transcription. We add a Hill relation with coefficient β to each equation for $\dot{x}_i$

$$\dot{x}_i = k_{\uparrow i}(m)\left(x_i^{ref} - x_i\right) - k_{\downarrow i}(m)x_i + \sum_j c_{ij}(m)x_i x_j \tag{S5.2}$$

$$+ \alpha_i(\overrightarrow{y_k}, z)\frac{x_i^\beta}{x_i^\beta + 1}$$

scaled by sensitivity $\alpha_i(\overrightarrow{y_k}, z)$, which are components of the sensitivity vector $\vec{\alpha}$. $\overrightarrow{y_k}$ is a vector of concentrations of global transcriptional participants, which may or may not all be explicitly mechanosensitive; $\overrightarrow{y_k}$ contains all the components of $\vec{x}$, and therefore has dependence on ECM stiffness m. z is a label of the chromatin conformational state, which can be thought of as the single-cell Hi-C map of chromatin contacts; z also depends on m *via* physical changes to the nucleus initiated by the LINC complex [262,291]. Altogether, the chromatin state z and the global transcriptional cofactors $\overrightarrow{y_k}$ determine how effectively the mechanosensitive components of $\vec{x}$ can self-reinforce.

S5.2 Derivation of Nonlinearly Dynamic Reinforcement Sensitivity

Each element $\alpha_i(\overrightarrow{y_k}, z)$ can be written as a sum expansion of reinforcement matrices $A^{(n)}$ multiplying $\overrightarrow{y_k}$ and z:

$$\alpha_i = \sum_k a_{ik}^{(1)} y_k + a_{iz}^{(1)} z + \sum_k a_{ikz}^{(2)} y_k z + \sum_{k,l} a_{ikl}^{(2)} y_k y_l \tag{S5.3}$$

$$+ \sum_{k,l} a_{iklz}^{(3)} y_k y_l z \dots$$

where a^n are elements of reinforcement matrices A^n with dimension $n + 1$. These matrix elements are weights which represent the degree to which each component of the global transcriptional environment or the global chromatin conformational state influences the self-reinforcing capability of mechanosensitive component x_i. The weights are analogous to activity coefficients in regular solution theory, where cooperativity between different species in solution can cause nonlinear thermodynamics of mixing far from the dilute limit. This cooperativity arises from favorable binding interactions between solute species and long-range forces in polar media. These same features are prominent in the nucleoplasm, particularly the catalysis of transcription by formation of multi-component binding complexes [292,293].

We are interested in how this self-reinforcing capability evolves over time, and using the chain rule we can write the time derivative of α_i as

$$\frac{d\alpha_i}{dt} = \sum_k \frac{\partial \alpha_i}{\partial y_k} \frac{\partial y_k}{dt} + \frac{\partial \alpha_i}{\partial z} \frac{\partial z}{dt} \tag{S5.4}$$

Plugging Eq. S5.3 into Eq. S5.4, we arrive at

$$\frac{d\alpha_i}{dt} = \sum_{k,l\ldots} (a_{ik}^{(1)} + a_{ikz}^{(2)}z + a_{ikl}^{(2)}y_l + a_{iklz}^{(3)}y_l z + \ldots)\frac{\partial y_k}{\partial t} + (a_{iz}^{(1)} \quad \text{(S5.5)}$$

$$+ a_{ikz}^{(2)}y_k + \ldots)\frac{\partial z}{dt}$$

Here, we see that the dynamics of self-reinforcement sensitivity depend on dynamics of the transcription regulatory environment and the chromatin conformation, weighted by the matrix elements of the reinforcement matrices $A_i^{(n)}$. $\frac{dy_k}{dt}$ and $\frac{dz}{dt}$ are equivalent to timescales τ for each transcriptionally active component and the chromatin conformation, respectively, and generally can depend on x_i and m. The coefficients a_{ik}^n are generally non-linear functions of y_k, analogously for $a_{zk}^{(n)}$ depending on z. Given sufficient data to populate the partial derivative relations and reinforcement matrices in Eq. S5.5, the steady-state dynamics of cellular plasticity can be completely specified through this framework. However, this relies on highly detailed, time-dependent mechanistic knowledge which is far beyond the scope of current experimental or simulation techniques. Rather than estimate all these individual relationships with placeholder coefficients or linear rate equations, we separate the components of Eq. S5.5 into two timescales and perform an averaging to distill out complexity while preserving phenomenological features. Since the vector y_k contains transcriptionally active components of x and therefore depends on the mechanical priming program $m(t)$, we know that some terms in Eq. S5.5 will change on the same timescale as x_i and that this timescale is an upper bound for $\frac{d\alpha_i}{dt}$. We make an arbitrary but

165

phenomenologically justified choice of $\vec{c_i}\frac{m^\zeta}{m^\zeta+1}$ to represent these fast non-linear processes, where the time dependence originates from $m(t)$, and gather the slower terms into a separate term $\alpha_i(t_{slow})$. This term still retains x_i dependence and m dependence from components of $\frac{dy_k}{dt}$ and $\frac{dz}{dt}$ but contains all the slower processes in these vectors (introduced as $\tau_s \frac{m}{m_0}$ and τ_f) as well as the nonlinear scaling originating from the coefficients of $A_i^{(n)}$ (introduced as $\alpha \exp(-\frac{x}{x_{ref}})$). Splitting $\alpha_i(t_{slow})$ into a piecewise function by region is a phenomenological choice but reflects the fact that different terms favoring an increase, decrease, or equilibration of the sensitivity will dominate depending on the magnitude of the external mechanical signal. Finally, when we perform an averaging over the components x_i in the main text, the system of equations described in Eq. S5.5 collapse into a single equation below with two terms in each region describing both fast and slow dynamics of mechanosensitive self-reinforcement.

$$\frac{d\alpha}{dt} = \begin{cases} -\dfrac{\alpha-\alpha_0}{\tau_f} + c\,\dfrac{m^\zeta}{m^\zeta+1}, & I \\[2mm] \dfrac{\alpha}{\tau_s}\dfrac{m}{m_0}\exp-\dfrac{x}{x_{ref}} + c\,\dfrac{m^\zeta}{m^\zeta+1}, & II \\[2mm] -\dfrac{\alpha}{\tau_s}\dfrac{m}{m_0}\exp-\dfrac{x}{x_{ref}} + c\,\dfrac{m^\zeta}{m^\zeta+1}, & III \end{cases} \qquad (S5.6)$$

166

Bibliography

[1]   Y. Li, J. Zhang, Q. Chen, X. Xia, M. Chen, Y. Li, J. W. Zhang, Q. G. Chen, M. H. Chen, and X. H. Xia, *Emerging of Heterostructure Materials in Energy Storage: A Review*, Advanced Materials **33**, 2100855 (2021).

[2]   D. Deng, K. S. Novoselov, Q. Fu, N. Zheng, Z. Tian, and X. Bao, *Catalysis with Two-Dimensional Materials and Their Heterostructures*, Nature Nanotechnology **11**, 218 (2016).

[3]   K. S. Novoselov, A. Mishchenko, A. Carvalho, and A. H. Castro Neto, *2D Materials and van Der Waals Heterostructures.*, Science **353**, aac9439 (2016).

[4]   X. Liu and S. Wang, *Three-Dimensional Nano-Biointerface as a New Platform for Guiding Cell Fate*, Chemical Society Reviews **43**, 2385 (2014).

[5]   K. Saha, Y. Mei, C. M. Reisterer, N. K. Pyzocha, J. Yang, J. Muffat, M. C. Davies, M. R. Alexander, R. Langer, D. G. Anderson, and R. Jaenisch, *Surface-Engineered Substrates for Improved Human Pluripotent Stem Cell Culture under Fully Defined Conditions*, Proceedings of the National Academy of Sciences of the United States of America **108**, 18714 (2011).

[6]   H. Kumar, D. Er, L. Dong, J. Li, and V. B. Shenoy, *Elastic Deformations in 2D van Der Waals Heterostructures and Their Impact on Optoelectronic*

Properties: Predictions from a Multiscale Computational Approach, Scientific Reports **5**, 10872 (2015).

[7]   D. Edelberg, H. Kumar, V. Shenoy, H. Ochoa, and A. N. Pasupathy, *Tunable Strain Soliton Networks Confine Electrons in Van Der Waals Materials*, Nature Physics **16**, 1097 (2019).

[8]   J. A. Elliott, *Novel Approaches to Multiscale Modelling in Materials Science*, International Materials Reviews **56**, 207 (2011).

[9]   K. Matouš, M. G. D. Geers, V. G. Kouznetsova, and A. Gillman, *A Review of Predictive Nonlinear Theories for Multiscale Modeling of Heterogeneous Materials*, Journal of Computational Physics **330**, 192 (2017).

[10]   T. E. Karakasidis and C. A. Charitidis, *Multiscale Modeling in Nanomaterials Science*, Materials Science and Engineering: C **27**, 1082 (2007).

[11]   W. Kohn, *Nobel Lecture: Electronic Structure of Matter—Wave Functions and Density Functionals*, Reviews of Modern Physics **71**, 1253 (1999).

[12]   W. Kohn and L. J. Sham, *Self-Consistent Equations Including Exchange and Correlation Effects*, Physical Review **140**, A1133 (1965).

[13]   P. Hohenberg and W. Kohn, *Inhomogeneous Electron Gas*, Physical Review **136**, B864 (1964).

[14] R. O. Jones, *Density Functional Theory: Its Origins, Rise to Prominence, and Future*, Reviews of Modern Physics **87**, 897 (2015).

[15] J. P. Perdew and Y. Wang, *Accurate and Simple Analytic Representation of the Electron-Gas Correlation Energy*, Physical Review B **45**, 13244 (1992).

[16] J. P. Perdew, K. Burke, and M. Ernzerhof, *Generalized Gradient Approximation Made Simple*, Physical Review Letters **77**, 3865 (1996).

[17] J. P. Perdew, J. A. Chevary, S. H. Vosko, K. A. Jackson, M. R. Pederson, D. J. Singh, and C. Fiolhais, *Atoms, Molecules, Solids, and Surfaces: Applications of the Generalized Gradient Approximation for Exchange and Correlation*, Physical Review B **46**, 6671 (1992).

[18] D. Sholl and J. Steckel, *Density Functional Theory: A Practical Introduction* (2009).

[19] R. N. Barnett and U. Landman, *Born-Oppenheimer Molecular-Dynamics Simulations of Finite Systems: Structure and Dynamics of H2O2*, Physical Review B **48**, 2081 (1993).

[20] G. Kresse and J. Furthmüller, *Efficiency of Ab-Initio Total Energy Calculations for Metals and Semiconductors Using a Plane-Wave Basis Set*, Computational Materials Science **6**, 15 (1996).

169

[21] G. Kresse and J. Hafner, Ab Initio *Molecular-Dynamics Simulation of the Liquid-Metal–Amorphous-Semiconductor Transition in Germanium*, Physical Review B **49**, 14251 (1994).

[22] A. Hjorth Larsen, J. JØrgen Mortensen, J. Blomqvist, I. E. Castelli, R. Christensen, M. Dułak, J. Friis, M. N. Groves, B. Hammer, C. Hargus, E. D. Hermes, P. C. Jennings, P. Bjerre Jensen, J. Kermode, J. R. Kitchin, E. Leonhard Kolsbjerg, J. Kubal, K. Kaasbjerg, S. Lysgaard, J. Bergmann Maronsson, T. Maxson, T. Olsen, L. Pastewka, A. Peterson, C. Rostgaard, J. SchiØtz, O. Schütt, M. Strange, K. S. Thygesen, T. Vegge, L. Vilhelmsen, M. Walter, Z. Zeng, and K. W. Jacobsen, *The Atomic Simulation Environment—a Python Library for Working with Atoms*, Journal of Physics: Condensed Matter **29**, 273002 (2017).

[23] S. P. Ong, W. D. Richards, A. Jain, G. Hautier, M. Kocher, S. Cholia, D. Gunter, V. L. Chevrier, K. A. Persson, and G. Ceder, *Python Materials Genomics (Pymatgen): A Robust, Open-Source Python Library for Materials Analysis*, Computational Materials Science **68**, 314 (2013).

[24] K. T. Butler, D. W. Davies, H. Cartwright, O. Isayev, and A. Walsh, *Machine Learning for Molecular and Materials Science*, Nature 2018 **559**, 547 (2018).

[25] J. Schmidt, M. R. G. Marques, S. Botti, and M. A. L. Marques, *Recent Advances and Applications of Machine Learning in Solid-State Materials Science*, Npj Computational Materials **5**, 1 (2019).

[26] W. Gong and Q. Yan, *Graph-Based Deep Learning Frameworks for Molecules and Solid-State Materials*, Computational Materials Science **195**, 110332 (2021).

[27] A. A. Hagberg, D. A. Schult, and P. J. Swart, *Exploring Network Structure, Dynamics, and Function Using NetworkX*, http://conference.scipy.org/proceedings/SciPy2008/paper_2/.

[28] A. Paszke, S. Gross, F. Massa, A. Lerer, J. Bradbury Google, G. Chanan, T. Killeen, Z. Lin, N. Gimelshein, L. Antiga, A. Desmaison, A. K. Xamla, E. Yang, Z. Devito, M. Raison Nabla, A. Tejani, S. Chilamkurthy, Q. Ai, B. Steiner, L. F. Facebook, J. B. Facebook, and S. Chintala, *PyTorch: An Imperative Style, High-Performance Deep Learning Library*, (2019).

[29] N. Ramakrishnan and V. S. Arunachalam, *Finite Element Methods for Materials Modelling*, Progress in Materials Science **42**, 253 (1997).

[30] L. Chanussot, A. Das, S. Goyal, T. Lavril, M. Shuaibi, M. Riviere, K. Tran, J. Heras-Domingo, C. Ho, W. Hu, A. Palizhati, A. Sriram, B. Wood, J. Yoon,

D. Parikh, C. L. Zitnick, and Z. Ulissi, *Open Catalyst 2020 (OC20) Dataset and Community Challenges*, ACS Catalysis **11**, 6059 (2021).

[31] K. Hennessy, A. Badolato, M. Winger, D. Gerace, M. Atatüre, S. Gulde, S. Fält, E. L. Hu, and A. Imamoğlu, *Quantum Nature of a Strongly Coupled Single Quantum Dot–Cavity System*, Nature **445**, 896 (2007).

[32] A. P. Alivisatos, *Semiconductor Clusters, Nanocrystals, and Quantum Dots*, Science **271**, 933 (1996).

[33] J. Jasieniak, L. Smith, J. Van Embden, P. Mulvaney, and M. Califano, *Re-Examination of the Size-Dependent Absorption Properties of CdSe Quantum Dots*, J. Phys. Chem. C **113**, 119468 (2009).

[34] C. Kurtsiefer, S. Mayer, P. Zarda, and H. Weinfurter, *Stable Solid-State Source of Single Photons*, Physical Review Letters **85**, 290 (2000).

[35] P. Senellart, G. Solomon, and A. White, *High-Performance Semiconductor Quantum-Dot Single-Photon Sources*, Nature Nanotechnology **12**, 1026 (2017).

[36] A. Gupta, T. Sakthivel, and S. Seal, *Recent Development in 2D Materials beyond Graphene*, Progress in Materials Science **73**, 44 (2015).

172

[37]   K. S. Novoselov, A. Bostwick, T. Seyller, K. Horn, and E. Rotenberg, *Electric Field Effect in Atomically Thin Carbon Films*, Science **306**, 666 (2004).

[38]   M. I. Katsnelson, K. S. Novoselov, and A. K. Geim, *Chiral Tunnelling and the Klein Paradox in Graphene*, Nature Physics **2**, 620 (2006).

[39]   J. Lee, D. Wong, J. Velasco Jr, J. F. Rodriguez-Nieva, S. Kahn, H.-Z. Tsai, T. Taniguchi, K. Watanabe, A. Zettl, F. Wang, L. S. Levitov, and M. F. Crommie, *Imaging Electrostatically Confined Dirac Fermions in Graphene Quantum Dots*, Nature Physics **12**, 1032 (2016).

[40]   C. Gutiérrez, L. Brown, C.-J. Kim, J. Park, and A. N. Pasupathy, *Klein Tunnelling and Electron Trapping in Nanometre-Scale Graphene Quantum Dots*, Nature Physics **12**, 1069 (2016).

[41]   M. Zarenia, A. Chaves, G. A. Farias, and F. M. Peeters, *Energy Levels of Triangular and Hexagonal Graphene Quantum Dots: A Comparative Study between the Tight-Binding and Dirac Equation Approach*, Physical Review B **84**, 245403 (2011).

[42]   J. Milton Pereira, P. Vasilopoulos, and F. M. Peeters, *Tunable Quantum Dots in Bilayer Graphene*, Nano Letters **7**, 946 (2007).

[43] J. M. Pereira, V. Mlinar, F. M. Peeters, and P. Vasilopoulos, *Confined States and Direction-Dependent Transmission in Graphene Quantum Wells*, Physical Review B **74**, 045424 (2006).

[44] K. S. Kim, A. L. Walter, L. Moreschini, T. Seyller, K. Horn, E. Rotenberg, and A. Bostwick, *Coexisting Massive and Massless Dirac Fermions in Symmetry-Broken Bilayer Graphene*, Nature Materials **12**, 887 (2013).

[45] S. Y. Zhou, G.-H. Gweon, A. V. Fedorov, P. N. First, W. A. de Heer, D.-H. Lee, F. Guinea, A. H. Castro Neto, and A. Lanzara, *Substrate-Induced Bandgap Opening in Epitaxial Graphene*, Nature Materials **6**, 770 (2007).

[46] P. Recher, J. Nilsson, G. Burkard, and B. Trauzettel, *Bound States and Magnetic Field Induced Valley Splitting in Gate-Tunable Graphene Quantum Dots*, Physical Review B **79**, 085407 (2009).

[47] A. Matulis and F. M. Peeters, *Quasibound States of Quantum Dots in Single and Bilayer Graphene*, Physical Review B **77**, 115423 (2008).

[48] T. G. Pedersen, A.-P. Jauho, and K. Pedersen, *Optical Response and Excitons in Gapped Graphene*, Phys. Rev. B **79**, 113406 (2009).

[49] C. Zhang, C. Gong, Y. Nie, K.-A. Min, C. Liang, Y. J. Oh, H. Zhang, W. Wang, S. Hong, L. Colombo, R. M. Wallace, and K. Cho, *Systematic Study of Electronic Structure and Band Alignment of Monolayer Transition Metal*

Dichalcogenides in Van Der Waals Heterostructures, 2D Materials **4**, 015026 (2017).

[50] M. Bieniek, M. Korkusiński, L. Szulakowska, P. Potasz, I. Ozfidan, and P. Hawrylak, *Band Nesting, Massive Dirac Fermions, and Valley Landé and Zeeman Effects in Transition Metal Dichalcogenides: A Tight-Binding Model*, Physical Review B **97**, 85153 (2018).

[51] D. Xiao, G.-B. Liu, W. Feng, X. Xu, and W. Yao, *Coupled Spin and Valley Physics in Monolayers of MoS$_2$ and Other Group-VI Dichalcogenides*, Physical Review Letters **108**, 196802 (2012).

[52] G.-B. Liu, W.-Y. Shan, Y. Yao, W. Yao, and D. Xiao, *Three-Band Tight-Binding Model for Monolayers of Group-VIB Transition Metal Dichalcogenides*, PHYSICAL REVIEW B **88**, 85433 (2013).

[53] A. Kormányos, V. Zólyomi, N. D. Drummond, P. Rakyta, G. Burkard, and V. I. Fal'ko, *Monolayer MoS$_2$: Trigonal Warping, the Valley, and Spin-Orbit Coupling Effects*, Phyiscal Review B **88**, 45416 (2013).

[54] D. Jariwala, V. K. Sangwan, L. J. Lauhon, T. J. Marks, and M. C. Hersam, *Emerging Device Applications for Semiconducting Two-Dimensional Transition Metal Dichalcogenides*, ACS Nano **8**, 1102 (2014).

175

[55] S. Xie, L. Tu, Y. Han, L. Huang, K. Kang, K. U. Lao, P. Poddar, C. Park, D. A. Muller, R. A. DiStasio, and J. Park, *Coherent, Atomically Thin Transition-Metal Dichalcogenide Superlattices with Engineered Strain.*, Science **359**, 1131 (2018).

[56] Z. Zhang, P. Chen, X. Duan, K. Zang, J. Luo, and X. Duan, *Robust Epitaxial Growth of Two-Dimensional Heterostructures, Multiheterostructures, and Superlattices*, Science **357**, 788 (2017).

[57] Y. Gong, J. Lin, X. Wang, G. Shi, S. Lei, Z. Lin, X. Zou, G. Ye, R. Vajtai, B. I. Yakobson, H. Terrones, M. Terrones, B. K. Tay, J. Lou, S. T. Pantelides, Z. Liu, W. Zhou, and P. M. Ajayan, *Vertical and In-Plane Heterostructures from WS$_2$/MoS$_2$ Monolayers*, Nature Materials **13**, 1135 (2014).

[58] L.-W. Wang and A. Zunger, *High-Energy Excitonic Transitions in CdSe Quantum Dots*, Journal of Physical Chemistry B **102**, 6449 (1998).

[59] J. Mei, Y. Wu, C. T. Chan, and Z.-Q. Zhang, *First-Principles Study of Dirac and Dirac-like Cones in Phononic and Photonic Crystals*, Physical Review B **86**, 035141 (2012).

[60] H. Peelaers and C. G. Van De Walle, *Effects of Strain on Band Structure and Effective Masses in MoS$_2$*, Physical Review B **86**, 241401 (2012).

[61] W. S. Yun, S. W. Han, S. C. Hong, I. G. Kim, and J. D. Lee, *Thickness and Strain Effects on Electronic Structures of Transition Metal Dichalcogenides: 2H- M X 2 Semiconductors (M = Mo, W; X = S, Se, Te)*, Physical Review B **85**, 033305 (2012).

[62] G. Bin Liu, W. Y. Shan, Y. Yao, W. Yao, and D. Xiao, *Three-Band Tight-Binding Model for Monolayers of Group-VIB Transition Metal Dichalcogenides*, Physical Review B **88**, 85433 (2013).

[63] K. Keyshar, M. Berg, X. Zhang, R. Vajtai, G. Gupta, C. K. Chan, T. E. Beechem, P. M. Ajayan, A. D. Mohite, and T. Ohta, *Experimental Determination of the Ionization Energies of MoSe$_2$, WS$_2$, and MoS$_2$ on SiO$_2$ Using Photoemission Electron Microscopy*, ACS Nano **11**, 8223 (2017).

[64] H. Ye, J. Zhou, D. Er, C. C. Price, Z. Yu, Y. Liu, J. Lowengrub, J. Lou, Z. Liu, and V. B. Shenoy, *Toward a Mechanistic Understanding of Vertical Growth of van Der Waals Stacked 2D Materials: A Multiscale Model and Experiments*, ACS Nano **11**, 12780 (2017).

[65] H. Rostami, A. G. Moghaddam, and R. Asgari, *Effective Lattice Hamiltonian for Monolayer MoS$_2$: Tailoring Electronic Structure with Perpendicular Electric and Magnetic Fields*, Physical Review B **88**, 85440 (2013).

177

[66] W. Hu and J. Yang, *Two-Dimensional van Der Waals Heterojunctions for Functional Materials and Devices*, J. Mater. Chem. C **5**, 12289 (2017).

[67] S. Pavlović and F. M. Peeters, *Electronic Properties of Triangular and Hexagonal MoS2 Quantum Dots*, Physical Review B **91**, 155410 (2015).

[68] K. Yang and M. de Llano, *Simple Variational Proof That Any Two-dimensional Potential Well Supports at Least One Bound State*, American Journal of Physics **57**, 85 (1989).

[69] H. Huang, X.-Q. Fu, and R.-S. Han, *Klein Paradox of Two-Dimensional Dirac Electrons in Circular Well Potential*, Communications in Theoretical Physics **58**, 205 (2012).

[70] R. D. Benguria, H. Castillo, R. D. Benguria, and M. Loewe, *The Dirac Equation with a δ-Potential*, Journal of Physics A: Mathematical and General **33**, 5315 (2000).

[71] D. P. Divincenzo and E. J. Mele, *Self-Consistent Effective-Mass Theory for Intralayer Screening in Graphite Intercalation Compounds*, Physical Review B **29**, 1685 (1984).

[72] H. Schmidt, S. Wang, L. Chu, M. Toh, R. Kumar, W. Zhao, A. H. Castro Neto, J. Martin, S. Adam, B. Özyilmaz, and G. Eda, *Transport Properties of*

Monolayer MoS$_2$ Grown by Chemical Vapor Deposition, Nano Letters **14**, 1909 (2014).

[73]   Y. Shi, W. Zhou, A.-Y. Lu, W. Fang, Y.-H. Lee, A. L. Hsu, S. M. Kim, K. K. Kim, H. Y. Yang, L.-J. Li, J.-C. Idrobo, and J. Kong, *Van Der Waals Epitaxy of MoS$_2$ Layers Using Graphene as Growth Templates*, Nano Letters **12**, 2784 (2012).

[74]   B. Messias De Resende, F. Crasto De Lima, R. H. Miwa, E. Vernek, and G. J. Ferreira, *Confinement and Fermion Doubling Problem in Dirac-like Hamiltonians*, Physical Review B: Rapid Communications **96**, 161113 (2017).

[75]   S. Helveg, J. V Lauritsen, E. Laegsgaard, I. Stensgaard, J. K. Nørskov, B. S. Clausen, H. Topsøe, and F. Besenbacher, *Atomic-Scale Structure of Single-Layer MoS$_2$ Nanoclusters*, Physical Review Letters **84**, 951 (2000).

[76]   J. V Lauritsen, M. V Bollinger, E. Laegsgaard, K. W. Jacobsen, J. K. Nørskov, B. S. Clausen, H. Topsøe, and F. Besenbacher, *Atomic-Scale Insight into Structure and Morphology Changes of MoS$_2$ Nanoclusters in Hydrotreating Catalysts*, Journal of Catalysis **221**, 510 (2004).

179

[77] K. Chen, X. Wan, J. Wen, W. Xie, Z. Kang, X. Zeng, H. Chen, and J.-B. Xu, *Electronic Properties of MoS$_2$–WS$_2$ Heterostructures Synthesized with Two-Step Lateral Epitaxial Strategy*, ACS Nano **9**, 9868 (2015).

[78] M. Hafeez, L. Gan, H. Li, Y. Ma, and T. Zhai, *Chemical Vapor Deposition Synthesis of Ultrathin Hexagonal ReSe$_2$ Flakes for Anisotropic Raman Property and Optoelectronic Application*, Advanced Materials **28**, 8296 (2016).

[79] V. M. Hong Ng, H. Huang, K. Zhou, P. S. Lee, W. Que, J. Z. Xu, and L. B. Kong, *Recent Progress in Layered Transition Metal Carbides and/or Nitrides (MXenes) and Their Composites: Synthesis and Applications*, Journal of Materials Chemistry A **5**, 3039 (2017).

[80] W. Choi, N. Choudhary, G. H. Han, J. Park, D. Akinwande, and Y. H. Lee, *Recent Development of Two-Dimensional Transition Metal Dichalcogenides and Their Applications*, Materials Today **20**, 116 (2017).

[81] W. Zhou, Y.-Y. Zhang, J. Chen, D. Li, J. Zhou, Z. Liu, M. F. Chisholm, S. T. Pantelides, and K. P. Loh, *Dislocation-Driven Growth of Two-Dimensional Lateral Quantum-Well Superlattices*, Science Advances **4**, eaap9096 (2018).

[82] M. G. Stanford, P. R. Pudasaini, N. Cross, K. Mahady, A. N. Hoffman, D. G. Mandrus, G. Duscher, M. F. Chisholm, and P. D. Rack, *Tungsten Diselenide*

Patterning and Nanoribbon Formation by Gas-Assisted Focused-Helium-Ion-Beam-Induced Etching, Small Methods **1**, 1600060 (2017).

[83] Y. Kobayashi, S. Yoshida, M. Maruyama, H. Mogi, K. Murase, Y. Maniwa, O. Takeuchi, S. Okada, H. Shigekawa, and Y. Miyata, *Continuous Heteroepitaxy of Two-Dimensional Heterostructures Based on Layered Chalcogenides*, ACS Nano **13**, 7527 (2019).

[84] L. K. Ono, E. J. Juarez-Perez, and Y. Qi, *Progress on Perovskite Materials and Solar Cells with Mixed Cations and Halide Anions*, ACS Applied Materials & Interfaces **9**, 30197 (2017).

[85] L. Qiu, L. K. Ono, and Y. Qi, *Advances and Challenges to the Commercialization of Organic–Inorganic Halide Perovskite Solar Cell Technology*, Materials Today Energy **7**, 169 (2018).

[86] Q. Fu, X. Tang, B. Huang, T. Hu, L. Tan, L. Chen, and Y. Chen, *Recent Progress on the Long-Term Stability of Perovskite Solar Cells*, Advanced Science **5**, 1700387 (2018).

[87] J. Yang, B. D. Siempelkamp, D. Liu, and T. L. Kelly, *Investigation of $CH_3NH_3PbI_3$ Degradation Rates and Mechanisms in Controlled Humidity Environments Using In Situ Techniques*, ACS Nano **9**, 1955 (2015).

[88] J. M. Frost, K. T. Butler, F. Brivio, C. H. Hendon, M. van Schilfgaarde, and A. Walsh, *Atomistic Origins of High-Performance in Hybrid Halide Perovskite Solar Cells*, Nano Letters **14**, 2584 (2014).

[89] C. C. Stoumpos, D. H. Cao, D. J. Clark, J. Young, J. M. Rondinelli, J. I. Jang, J. T. Hupp, and M. G. Kanatzidis, *Ruddlesden–Popper Hybrid Lead Iodide Perovskite 2D Homologous Semiconductors*, Chemistry of Materials **28**, 2852 (2016).

[90] D. B. Mitzi, *Synthesis, Crystal Structure, and Optical and Thermal Properties of ($C_4H_9NH_3$)$_2$MI$_4$ (M = Ge, Sn, Pb)*, Chemistry of Materials **8**, 791 (1996).

[91] H. Tsai, W. Nie, J.-C. Blancon, C. C. Stoumpos, R. Asadpour, B. Harutyunyan, A. J. Neukirch, R. Verduzco, J. J. Crochet, S. Tretiak, L. Pedesseau, J. Even, M. A. Alam, G. Gupta, J. Lou, P. M. Ajayan, M. J. Bedzyk, M. G. Kanatzidis, and A. D. Mohite, *High-Efficiency Two-Dimensional Ruddlesden–Popper Perovskite Solar Cells*, Nature **536**, 312 (2016).

[92] J. Calabrese, N. L. Jones, R. L. Harlow, N. Herron, D. L. Thron, and Y. Wang, *Preparation and Characterization of Layered Lead Halide Compounds*, J. Am. Chem. Soc **113**, 2328 (1991).

182

[93] I. C. Smith, E. T. Hoke, D. Solis-Ibarra, M. D. McGehee, and H. I. Karunadasa, *A Layered Hybrid Perovskite Solar-Cell Absorber with Enhanced Moisture Stability*, Angewandte Chemie International Edition **53**, 11232 (2014).

[94] M. L. Kepenekian, B. Traore, J.-C. Blancon, L. Pedesseau, H. Tsai, W. Nie, C. C. Stoumpos, M. G. Kanatzidis, J. Even, A. D. Mohite, S. Tretiak, and C. Katan, *Concept of Lattice Mismatch and Emergence of Surface States in Two-Dimensional Hybrid Perovskite Quantum Wells*, Nano Lett. **18**, 5603 (2018).

[95] A. Z. Chen, M. Shiu, J. H. Ma, M. R. Alpert, D. Zhang, B. J. Foley, D.-M. Smilgies, S.-H. Lee, and J. J. Choi, *Origin of Vertical Orientation in Two-Dimensional Metal Halide Perovskites and Its Effect on Photovoltaic Performance*, Nature Communications **9**, 1336 (2018).

[96] X. Zhang, R. Munir, Z. Xu, Y. Liu, H. Tsai, W. Nie, J. Li, T. Niu, D.-M. Smilgies, M. G. Kanatzidis, A. D. Mohite, K. Zhao, A. Amassian, and S. Liu, *Phase Transition Control for High Performance Ruddlesden–Popper Perovskite Solar Cells*, Advanced Materials **10**, 1707166 (2018).

[97] J. Hu, I. W. H. Oswald, S. J. Stuard, M. M. Nahid, N. Zhou, O. F. Williams, Z. Guo, L. Yan, H. Hu, Z. Chen, X. Xiao, Y. Lin, Z. Yang, J. Huang, A. M. Moran, H. Ade, J. R. Neilson, and W. You, *Synthetic Control over*

Orientational Degeneracy of Spacer Cations Enhances Solar Cell Efficiency in Two-Dimensional Perovskites, Nature Communications **10**, 1276 (2019).

[98]   R. Quintero-Bermudez, A. Gold-Parker, A. H. Proppe, R. Munir, Z. Yang, S. O. Kelley, A. Amassian, M. F. Toney, and E. H. Sargent, *Compositional and Orientational Control in Metal Halide Perovskites of Reduced Dimensionality*, Nature Materials **17**, 900 (2018).

[99]   X. He, Y. Wang, K. Li, X. Wang, P. Liu, Y. Yang, Q. Liao, T. Zhai, J. Yao, and H. Fu, *Oriented Growth of Ultrathin Single Crystals of 2D Ruddlesden–Popper Hybrid Lead Iodide Perovskites for High-Performance Photodetectors*, ACS Applied Materials & Interfaces **11**, 15905 (2019).

[100] G. C. Papavassiliou and I. B. Koutselas, *Structural, Optical and Related Properties of Some Natural Three- and Lower-Dimensional Semiconductor Systems*, Synthetic Metals **71**, 1713 (1995).

[101] K. Tanaka and T. Kondo, *Bandgap and Exciton Binding Energies in Lead-Iodide-Based Natural Quantum-Well Crystals*, Science and Technology of Advanced Materials **4**, 599 (2003).

[102] C. Katan, N. Mercier, and J. Even, *Quantum and Dielectric Confinement Effects in Lower-Dimensional Hybrid Perovskite Semiconductors*, Chemical Reviews **119**, 3140 (2019).

184

[103] T. Ishihara, J. Takahashi, and T. Goto, *Optical Properties Due to Electronic Transitions in Two-Dimensional Semiconductors($C_nH_{2n+1}NH_3)_2PbI_4$*, Physical Review B **42**, 11099 (1990).

[104] B. Traore, L. Pedesseau, L. Assam, X. Che, J.-C. Blancon, H. Tsai, W. Nie, C. C. Stoumpos, M. G. Kanatzidis, S. Tretiak, A. D. Mohite, J. Even, M. L. Kepenekian, and C. Katan, *Composite Nature of Layered Hybrid Perovskites: Assessment on Quantum and Dielectric Confinements and Band Alignment*, ACS Nano **12**, 3321 (2018).

[105] J.-C. Blancon, A. V. Stier, H. Tsai, W. Nie, C. C. Stoumpos, B. Traoré, L. Pedesseau, M. Kepenekian, F. Katsutani, G. T. Noe, J. Kono, S. Tretiak, S. A. Crooker, C. Katan, M. G. Kanatzidis, J. J. Crochet, J. Even, and A. D. Mohite, *Scaling Law for Excitons in 2D Perovskite Quantum Wells*, Nature Communications **9**, 2254 (2018).

[106] J. Even, L. Pedesseau, and C. Katan, *Understanding Quantum Confinement of Charge Carriers in Layered 2D Hybrid Perovskites*, ChemPhysChem **15**, 3733 (2014).

[107] L. Pedesseau, D. Sapori, B. Traore, R. Robles, H.-H. Fang, M. A. Loi, H. Tsai, W. Nie, J.-C. Blancon, A. Neukirch, S. Tretiak, A. D. Mohite, C. Katan,

J. Even, and M. Kepenekian, *Advances and Promises of Layered Halide Hybrid Perovskite Semiconductors*, ACS Nano **10**, 9776 (2016).

[108] Q. Tu, I. Spanopoulos, P. Yasaei, C. C. Stoumpos, M. G. Kanatzidis, G. S. Shekhawat, and V. P. Dravid, *Stretching and Breaking of Ultrathin 2D Hybrid Organic–Inorganic Perovskites*, ACS Nano **12**, 10347 (2018).

[109] C. M. Raghavan, T.-P. Chen, S.-S. Li, W.-L. Chen, C.-Y. Lo, Y.-M. Liao, G. Haider, C.-C. Lin, C.-C. Chen, R. Sankar, Y.-M. Chang, F.-C. Chou, and C.-W. Chen, *Low-Threshold Lasing from 2D Homologous Organic–Inorganic Hybrid Ruddlesden–Popper Perovskite Single Crystals*, Nano Letters **18**, 3221 (2018).

[110] Y. Lin, Y. Bai, Y. Fang, Z. Chen, S. Yang, X. Zheng, S. Tang, Y. Liu, J. Zhao, and J. Huang, *Enhanced Thermal Stability in Perovskite Solar Cells by Assembling 2D/3D Stacking Structures*, J. Phys. Chem. Lett **9**, 654 (2018).

[111] K. Leng, I. Abdelwahab, I. Verzhbitskiy, M. Telychko, L. Chu, W. Fu, X. Chi, N. Guo, Z. Chen, Z. Chen, C. Zhang, Q.-H. Xu, J. Lu, M. Chhowalla, G. Eda, and K. P. Loh, *Molecularly Thin Two-Dimensional Hybrid Perovskites with Tunable Optoelectronic Properties Due to Reversible Surface Relaxation*, Nature Materials **17**, 908 (2018).

186

[112] D. H. Cao, C. C. Stoumpos, O. K. Farha, J. T. Hupp, and M. G. Kanatzidis, *2D Homologous Perovskites as Light-Absorbing Materials for Solar Cell Applications*, Journal of the American Chemical Society **137**, 7843 (2015).

[113] M. C. Gélvez-Rueda, E. M. Hutter, D. H. Cao, N. Renaud, C. C. Stoumpos, J. T. Hupp, T. J. Savenije, M. G. Kanatzidis, and F. C. Grozema, *Interconversion between Free Charges and Bound Excitons in 2D Hybrid Lead Halide Perovskites*, The Journal of Physical Chemistry C **121**, 26566 (2017).

[114] S. Silver, J. Yin, H. Li, J.-L. Brédas, and A. Kahn, *Characterization of the Valence and Conduction Band Levels of* n = *1 2D Perovskites: A Combined Experimental and Theoretical Investigation*, Advanced Energy Materials **8**, 1703468 (2018).

[115] J. Liu, J. Leng, K. Wu, J. Zhang, and S. Jin, *Observation of Internal Photoinduced Electron and Hole Separation in Hybrid Two-Dimentional Perovskite Films*, Journal of the American Chemical Society **139**, 1432 (2017).

[116] C. M. M. Soe, G. P. Nagabhushana, R. Shivaramaiah, H. Tsai, W. Nie, J.-C. Blancon, F. Melkonyan, D. H. Cao, B. Traoré, L. Pedesseau, M. Kepenekian, C. Katan, J. Even, T. J. Marks, A. Navrotsky, A. D. Mohite, C. C. Stoumpos,

and M. G. Kanatzidis, *Structural and Thermodynamic Limits of Layer Thickness in 2D Halide Perovskites*, Proceedings of the National Academy of Sciences of the United States of America **116**, 58 (2019).

[117] L. Mao, R. M. Kennard, B. Traore, W. Ke, C. Katan, J. Even, M. L. Chabinyc, C. C. Stoumpos, and M. G. Kanatzidis, *Seven-Layered 2D Hybrid Lead Iodide Perovskites*, Chem **5**, 2593 (2019).

[118] C. M. M. Soe, C. C. Stoumpos, M. Kepenekian, B. Traoré, H. Tsai, W. Nie, B. Wang, C. Katan, R. Seshadri, A. D. Mohite, J. Even, T. J. Marks, and M. G. Kanatzidis, *New Type of 2D Perovskites with Alternating Cations in the Interlayer Space, $(C(NH_2)_3)(CH_3NH_3)_nPb_nI_{3n+1}$: Structure, Properties, and Photovoltaic Performance*, Journal of the American Chemical Society **139**, 16297 (2017).

[119] N. Li, Z. Zhu, C.-C. Chueh, H. Liu, B. Peng, A. Petrone, X. Li, L. Wang, and A. K.-Y. Jen, *Mixed Cation $FA_xPEA_{1-x}PbI_3$ with Enhanced Phase and Ambient Stability toward High-Performance Perovskite Solar Cells*, Advanced Energy Materials **7**, 1601307 (2017).

[120] L. N. Quan, M. Yuan, R. Comin, O. Voznyy, E. M. Beauregard, S. Hoogland, A. Buin, A. R. Kirmani, K. Zhao, A. Amassian, D. H. Kim, and E. H. Sargent,

Ligand-Stabilized Reduced-Dimensionality Perovskites, Journal of the American Chemical Society **138**, 2649 (2016).

[121] D. Giovanni, J. W. M. Lim, Z. Yuan, S. S. Lim, M. Righetto, J. Qing, Q. Zhang, H. A. Dewi, F. Gao, S. G. Mhaisalkar, N. Mathews, and T. C. Sum, *Ultrafast Long-Range Spin-Funneling in Solution-Processed Ruddlesden–Popper Halide Perovskites*, Nature Communications **10**, 3456 (2019).

[122] M. Yuan, L. N. Quan, R. Comin, G. Walters, R. Sabatini, O. Voznyy, S. Hoogland, Y. Zhao, E. M. Beauregard, P. Kanjanaboos, Z. Lu, D. H. Kim, and E. H. Sargent, *Perovskite Energy Funnels for Efficient Light-Emitting Diodes*, Nature Nanotechnology **11**, 872 (2016).

[123] J. Shi, Y. Gao, X. Gao, Y. Zhang, J. Zhang, X. Jing, and M. Shao, *Fluorinated Low-Dimensional Ruddlesden–Popper Perovskite Solar Cells with over 17% Power Conversion Efficiency and Improved Stability*, Advanced Materials **31**, 1901673 (2019).

[124] M. P. Hautzinger, J. Dai, Y. Ji, Y. Fu, J. Chen, I. A. Guzei, J. C. Wright, Y. Li, and S. Jin, *Two-Dimensional Lead Halide Perovskites Templated by a Conjugated Asymmetric Diammonium*, Inorganic Chemistry **56**, 14991 (2017).

189

[125] P. Cheng, Z. Xu, J. Li, Y. Liu, Y. Fan, L. Yu, D.-M. Smilgies, C. Müller, K. Zhao, and S. F. Liu, *Highly Efficient Ruddlesden–Popper Halide Perovskite PA$_2$MA$_4$Pb$_5$I$_{16}$ Solar Cells*, ACS Energy Letters **3**, 1975 (2018).

[126] I. Spanopoulos, I. Hadar, W. Ke, Q. Tu, M. Chen, H. Tsai, Y. He, G. Shekhawat, V. P. Dravid, M. R. Wasielewski, A. D. Mohite, C. C. Stoumpos, and M. G. Kanatzidis, *Uniaxial Expansion of the 2D Ruddlesden–Popper Perovskite Family for Improved Environmental Stability*, Journal of the American Chemical Society **141**, 5518 (2019).

[127] L. Mao, W. Ke, L. Pedesseau, Y. Wu, C. Katan, J. Even, M. R. Wasielewski, C. C. Stoumpos, and M. G. Kanatzidis, *Hybrid Dion–Jacobson 2D Lead Iodide Perovskites*, Journal of the American Chemical Society **140**, 3775 (2018).

[128] C. Price, J.-C. Blancon, A. Mohite, and V. Shenoy, *Interfacial Electromechanics Predicts Phase Behavior of 2D Hybrid Halide Perovskites*, ACS Nano **14**, 3353 (n.d.).

[129] P. S. Whitfield, N. Herron, W. E. Guise, K. Page, Y. Q. Cheng, I. Milas, and M. K. Crawford, *Structures, Phase Transitions and Tricritical Behavior of the Hybrid Perovskite Methyl Ammonium Lead Iodide*, Scientific Reports **6**, 35685 (2016).

[130] A. Fraccarollo, V. Cantatore, G. Boschetto, L. Marchese, and M. Cossi, Ab Initio *Modeling of 2D Layered Organohalide Lead Perovskites*, The Journal of Chemical Physics **144**, 164701 (2016).

[131] L. Glasser, *Systematic Thermodynamics of Layered Perovskites: Ruddlesden–Popper Phases*, Inorganic Chemistry **56**, 8920 (2017).

[132] P. E. Blöchl, *Projector Augmented-Wave Method*, Physical Review B **50**, 17953 (1994).

[133] S. Grimme, J. Antony, S. Ehrlich, and H. Krieg, *A Consistent and Accurate* Ab Initio *Parametrization of Density Functional Dispersion Correction (DFT-D) for the 94 Elements H-Pu*, The Journal of Chemical Physics **132**, 154104 (2010).

[134] S. Grimme, S. Ehrlich, and L. Goerigk, *Effect of the Damping Function in Dispersion Corrected Density Functional Theory*, Journal of Computational Chemistry **32**, 1456 (2011).

[135] N. N. Smirnova, L. Ya. Tsvetkova, T. A. Bykova, V. A. Ruchenin, and Y. Marcus, *Thermodynamic Properties of Tetrabutylammonium Iodide and Tetrabutylammonium Tetraphenylborate*, Thermochimica Acta **483**, 15 (2009).

191

[136] P. Müller, A. Saùl, and F. Leroy, *Simple Views on Surface Stress and Surface Energy Concepts*, Advances in Natural Sciences: Nanoscience and Nanotechnology **5**, 013002 (2014).

[137] R. C. Cammarata, *Surface and Interface Stress Effects in Thin Films*, Progress in Surface Science **46**, 1 (1994).

[138] A. C. Ferreira, A. Létoublon, S. Paofai, S. Raymond, C. Ecolivet, B. Rufflé, S. Cordier, C. Katan, M. I. Saidaminov, A. A. Zhumekenov, O. M. Bakr, J. Even, and P. Bourges, *Elastic Softness of Hybrid Lead Halide Perovskites*, Physical Review Letters **121**, 085502 (2018).

[139] M. Faghihnasiri, M. Izadifard, and M. E. Ghazi, *DFT Study of Mechanical Properties and Stability of Cubic Methylammonium Lead Halide Perovskites ($CH_3NH_3PbX_3$, X = I, Br, Cl)*, The Journal of Physical Chemistry C **121**, 27059 (2017).

[140] L. She, M. Liu, and D. Zhong, *Atomic Structures of $CH_3NH_3PbI_3$ (001) Surfaces*, ACS Nano **10**, 1126 (2016).

[141] A. Walsh, *Principles of Chemical Bonding and Band Gap Engineering in Hybrid Organic–Inorganic Halide Perovskites*, The Journal of Physical Chemistry C **119**, 5755 (2015).

[142] S. Piskunov, E. A. Kotomin, E. Heifets, J. Maier, R. I. Eglitis, and G. Borstel, *Hybrid DFT Calculations of the Atomic and Electronic Structure for ABO₃ Perovskite (001) Surfaces*, Surface Science **575**, 75 (2005).

[143] M. Fechner, S. Ostanin, and I. Mertig, *Effect of the Surface Polarization in Polar Perovskites Studied from First Principles*, Physical Review B **77**, 094112 (2008).

[144] D. Wang, J. Liu, J. Zhang, S. Raza, X. Chen, and C.-L. Jia, *Ewald Summation for Ferroelectric Perovskites with Charges and Dipoles*, Computational Materials Science **162**, 314 (2019).

[145] E. F. Bertaut, *The Equivalent Charge Concept and Its Application to the Electrostatic Energy of Charges and Multipoles*, Journal De Physique **12**, 1331 (1978).

[146] D. Sapori, M. Kepenekian, L. Pedesseau, C. Katan, and J. Even, *Quantum Confinement and Dielectric Profiles of Colloidal Nanoplatelets of Halide Inorganic and Hybrid Organic–Inorganic Perovskites*, Nanoscale **8**, 6369 (2016).

[147] C. C. Stoumpos, C. M. M. Soe, H. Tsai, W. Nie, J.-C. Blancon, D. H. Cao, F. Liu, B. Traoré, C. Katan, J. Even, A. D. Mohite, and M. G. Kanatzidis, *High Members of the 2D Ruddlesden-Popper Halide Perovskites: Synthesis,*

193

Optical Properties, and Solar Cells of (CH$_3$(CH$_2$)$_3$NH$_3$)$_2$(CH$_3$NH$_3$)$_4$Pb$_5$I$_{16}$, Chem **2**, 427 (2017).

[148] V. B. Shenoy, C. D. Reddy, A. Ramasubramaniam, and Y. W. Zhang, *Edge-Stress-Induced Warping of Graphene Sheets and Nanoribbons*, Physical Review L **101**, 245501 (2008).

[149] C. Zhu, X. Niu, Y. Fu, N. Li, C. Hu, Y. Chen, X. He, G. Na, P. Liu, H. Zai, Y. Ge, Y. Lu, X. Ke, Y. Bai, S. Yang, P. Chen, Y. Li, M. Sui, L. Zhang, H. Zhou, and Q. Chen, *Strain Engineering in Perovskite Solar Cells and Its Impacts on Carrier Dynamics*, Nature Communications **10**, 815 (2019).

[150] R. D. King-Smith and D. Vanderbilt, *Theory of Polarization of Crystalline Solids*, Physical Review B **47**, 1651 (1993).

[151] A. Natan, L. Kronik, and Y. Shapira, *Computing Surface Dipoles and Potentials of Self-Assembled Monolayers from First Principles*, Journal of Applied Surface Science **252**, 7608 (2006).

[152] M. T. Weller, O. J. Weber, J. M. Frost, and A. Walsh, *Cubic Perovskite Structure of Black Formamidinium Lead Iodide, α-[HC(NH$_2$)$_2$]PbI$_3$, at 298 K*, The Journal of Physical Chemistry Letters **6**, 3209 (2015).

[153] T. Le, V. C. Epa, F. R. Burden, and D. A. Winkler, *Quantitative Structure-Property Relationship Modeling of Diverse Materials Properties*, Chemical Reviews **112**, 2889 (2012).

[154] G. B. Olson, *Computational Design of Hierarchically Structured Materials*, Science **277**, 1237 (1997).

[155] H. Ibach, *The Role of Surface Stress in Reconstruction, Epitaxial Growth and Stabilization of Mesoscopic Structures*, Surface Science Reports **29**, 195 (1997).

[156] A. Banerjee, D. Bernoulli, H. Zhang, M. F. Yuen, J. Liu, J. Dong, F. Ding, J. Lu, M. Dao, W. Zhang, Y. Lu, and S. Suresh, *Ultralarge Elastic Deformation of Nanoscale Diamond*, Science **360**, 300 (2018).

[157] R. H. Baughman, C. Cui, A. A. Zakhidov, Z. Iqbal, J. N. Barisci, G. M. Spinks, G. G. Wallace, A. Mazzoldi, D. de Rossi, A. G. Rinzler, O. Jaschinski, S. Roth, and M. Kertesz, *Carbon Nanotube Actuators*, Science **284**, 1340 (1999).

[158] B. W. Dodson, *Many-Body Surface Strain and Surface Reconstructions in Fcc Transition Metals*, Physical Review Letters **60**, 2288 (1988).

[159] J. Kang, Q. Zhang, Y. Wang, Z. Xia, and S. Guo, *Strain Engineering of Metal-Based Nanomaterials for Energy Electrocatalysis*, Chemical Society Reviews **48**, 3265 (2019).

[160] L. Wang, Z. Zeng, W. Gao, T. Maxson, D. Raciti, M. Giroux, X. Pan, C. Wang, and J. Greeley, *Tunable Intrinsic Strain in Two-Dimensional Transition Metal Electrocatalysts*, Science **363**, 870 (2019).

[161] T. He, W. Wang, F. Shi, X. Yang, X. Li, J. Wu, Y. Yin, and M. Jin, *Mastering the Surface Strain of Platinum Catalysts for Efficient Electrocatalysis*, Nature **598**, 76 (2021).

[162] M. Mavrikakis, B. Hammer, and J. K. Nørskov, *Effect of Strain on the Reactivity of Metal Surfaces*, Physical Review Letters **81**, 2819 (1998).

[163] C. M. Friend and B. Xu, *Heterogeneous Catalysis: A Central Science for a Sustainable Future*, Accounts of Chemical Research **50**, 517 (2017).

[164] A. J. Medford, A. Vojvodic, J. S. Hummelshøj, J. Voss, F. Abild-Pedersen, F. Studt, T. Bligaard, A. Nilsson, and J. K. Nørskov, *From the Sabatier Principle to a Predictive Theory of Transition-Metal Heterogeneous Catalysis*, Journal of Catalysis **328**, 36 (2015).

[165] Z. J. Zhao, S. Liu, S. Zha, D. Cheng, F. Studt, G. Henkelman, and J. Gong, *Theory-Guided Design of Catalytic Materials Using Scaling Relationships and Reactivity Descriptors*, Nature Reviews Materials **4**, 792 (2019).

[166] S. Wang, V. Petzold, V. Tripkovic, J. Kleis, J. G. Howalt, E. Skúlason, E. M. Fernández, B. Hvolbæk, G. Jones, A. Toftelund, H. Falsig, M. Björketun, F. Studt, F. Abild-Pedersen, J. Rossmeisl, J. K. Nørskov, and T. Bligaard, *Universal Transition State Scaling Relations for (de)Hydrogenation over Transition Metals*, Physical Chemistry Chemical Physics **13**, 20760 (2011).

[167] J. Greeley, *Theoretical Heterogeneous Catalysis: Scaling Relationships and Computational Catalyst Design*, Annual Review of Chemical and Biomolecular Engineering **7**, 605 (2016).

[168] M. M. Montemore and J. W. Medlin, *Scaling Relations between Adsorption Energies for Computational Screening and Design of Catalysts*, Catalysis Science & Technology **4**, 3748 (2014).

[169] A. Khorshidi, J. Violet, J. Hashemi, and A. A. Peterson, *How Strain Can Break the Scaling Relations of Catalysis*, Nature Catalysis **1**, 263 (2018).

[170] J. Pérez-Ramírez and N. López, *Strategies to Break Linear Scaling Relationships*, Nature Catalysis 2019 2:11 **2**, 971 (2019).

197

[171] S. Zhang, X. Zhang, G. Jiang, H. Zhu, S. Guo, D. Su, G. Lu, and S. Sun, *Tuning Nanoparticle Structure and Surface Strain for Catalysis Optimization*, Journal of the American Chemical Society **136**, 7734 (2014).

[172] G. Collins, J. D. Holmes, G. Collins, and J. D. Holmes, *Engineering Metallic Nanoparticles for Enhancing and Probing Catalytic Reactions*, Advanced Materials **28**, 5689 (2016).

[173] L. A. Kibler, A. M. El-Aziz, R. Hoyer, and D. M. Kolb, *Tuning Reaction Rates by Lateral Strain in a Palladium Monolayer*, Angewandte Chemie International Edition **44**, 2080 (2005).

[174] M. Luo and S. Guo, *Strain-Controlled Electrocatalysis on Multimetallic Nanomaterials*, Nature Reviews Materials **2**, 1 (2017).

[175] K. Jiang, M. Luo, Z. Liu, M. Peng, D. Chen, Y. R. Lu, T. S. Chan, F. M. F. de Groot, and Y. Tan, *Rational Strain Engineering of Single-Atom Ruthenium on Nanoporous MoS2 for Highly Efficient Hydrogen Evolution*, Nature Communications **12**, 1 (2021).

[176] H. Huang, H. Jia, Z. Liu, P. Gao, J. Zhao, Z. Luo, J. Yang, and J. Zeng, *Understanding of Strain Effects in the Electrochemical Reduction of CO2: Using Pd Nanostructures as an Ideal Platform*, Angewandte Chemie - International Edition **56**, 3594 (2017).

[177] B. T. Sneed, A. P. Young, and C. K. Tsung, *Building up Strain in Colloidal Metal Nanoparticle Catalysts*, Nanoscale **7**, 12248 (2015).

[178] D. Vollath, F. D. Fischer, and D. Holec, *Surface Energy of Nanoparticles – Influence of Particle Size and Structure*, Beilstein Journal of Nanotechnology **9**, 2265 (2018).

[179] J. Wu, L. Qi, H. You, A. Gross, J. Li, and H. Yang, *Icosahedral Platinum Alloy Nanocrystals with Enhanced Electrocatalytic Activities*, Journal of the American Chemical Society **134**, 11880 (2012).

[180] L. Gan, M. Heggen, S. Rudi, and P. Strasser, *Core-Shell Compositional Fine Structures of Dealloyed Pt XNi 1-x Nanoparticles and Their Impact on Oxygen Reduction Catalysis*, Nano Letters **12**, 5423 (2012).

[181] T. Wu, M. Sun, B. Huang, T. Wu, M. Sun, and B. Huang, *Atomic-Strain Mapping of High-Index Facets in Late-Transition-Metal Nanoparticles for Electrocatalysis*, Angewandte Chemie International Edition **60**, 22996 (2021).

[182] Z. Shi, E. Tsymbalov, M. Dao, S. Suresh, A. Shapeev, and J. Li, *Deep Elastic Strain Engineering of Bandgap through Machine Learning*, Proceedings of the National Academy of Sciences **116**, 4117 (2019).

199

[183] E. Tsymbalov, Z. Shi, M. Dao, S. Suresh, J. Li, and A. Shapeev, *Machine Learning for Deep Elastic Strain Engineering of Semiconductor Electronic Band Structure and Effective Mass*, Npj Computational Materials **7**, 1 (2021).

[184] O. Mamun, K. T. Winther, J. R. Boes, and T. Bligaard, *High-Throughput Calculations of Catalytic Properties of Bimetallic Alloy Surfaces*, Scientific Data **6**, 1 (2019).

[185] C. Chen, W. Ye, Y. Zuo, C. Zheng, and S. P. Ong, *Graph Networks as a Universal Machine Learning Framework for Molecules and Crystals*, Chemistry of Materials **31**, 3564 (2019).

[186] T. Xie and J. C. Grossman, *Crystal Graph Convolutional Neural Networks for an Accurate and Interpretable Prediction of Material Properties*, Physical Review Letters **120**, 145301 (2018).

[187] J. Klicpera, J. Groß, and S. Günnemann, *Directional Message Passing for Molecular Graphs*, (2020).

[188] J. Klicpera, S. Giri, J. T. Margraf, and S. Günnemann, *Fast and Uncertainty-Aware Directional Message Passing for Non-Equilibrium Molecules*, (2020).

[189] Z. Qiao, M. Welborn, A. Anandkumar, F. R. Manby, and T. F. Miller, *OrbNet: Deep Learning for Quantum Chemistry Using Symmetry-Adapted*

Atomic-Orbital Features, The Journal of Chemical Physics **153**, 124111 (2020).

[190] V. Fung, J. Zhang, E. Juarez, and B. G. Sumpter, *Benchmarking Graph Neural Networks for Materials Chemistry*, Npj Computational Materials **7**, 1 (2021).

[191] M. Zhong, K. Tran, Y. Min, C. Wang, Z. Wang, C.-T. Dinh, P. de Luna, Z. Yu, A. S. Rasouli, P. Brodersen, S. Sun, O. Voznyy, C.-S. Tan, M. Askerka, F. Che, M. Liu, A. Seifitokaldani, Y. Pang, S.-C. Lo, A. Ip, Z. Ulissi, and E. H. Sargent, *Accelerated Discovery of CO 2 Electrocatalysts Using Active Machine Learning*, Nature **581**, 178 (2020).

[192] R. G. S. Pala and F. Liu, *Determining the Adsorptive and Catalytic Properties of Strained Metal Surfaces Using Adsorption-Induced Stress*, The Journal of Chemical Physics **120**, 7720 (2004).

[193] S. Zeng, S. Shan, A. Lu, S. Wang, D. T. Caracciolo, R. J. Robinson, G. Shang, L. Xue, Y. Zhao, A. Zhang, Y. Liu, S. Liu, Z. Liu, F. Bai, J. Wu, H. Wang, and C. J. Zhong, *Copper-Alloy Catalysts: Structural Characterization and Catalytic Synergies*, Catalysis Science & Technology **11**, 5712 (2021).

[194] L. Perez and J. Wang, *The Effectiveness of Data Augmentation in Image Classification Using Deep Learning*, (2017).

[195] N. C. Frey, D. Akinwande, D. Jariwala, and V. B. Shenoy, *Machine Learning-Enabled Design of Point Defects in 2d Materials for Quantum and Neuromorphic Information Processing*, ACS Nano **14**, 13406 (2020).

[196] J. Karaguesian, J. R. Lunger, Y. Shao-Horn, and R. Gomez-Bombarelli, *Crystal Graph Convolutional Neural Networks for Per-Site Property Prediction*, Fourth Workshop on Machine Learning and the Physical Sciences (NeurIPS 2021) (2021).

[197] J. Humphreys, R. Lan, and S. Tao, *Development and Recent Progress on Ammonia Synthesis Catalysts for Haber–Bosch Process*, Advanced Energy and Sustainability Research **2**, 2000043 (2021).

[198] M. Hattori, S. Iijima, T. Nakao, H. Hosono, and M. Hara, *Solid Solution for Catalytic Ammonia Synthesis from Nitrogen and Hydrogen Gases at 50 °C*, Nature Communications **11**, 1 (2020).

[199] L. R. Johnson, S. Sridhar, L. Zhang, K. D. Fredrickson, A. S. Raman, J. Jang, C. Leach, A. Padmanabhan, C. C. Price, N. C. Frey, A. Raizada, V. Rajaraman, S. A. Saiprasad, X. Tang, and A. Vojvodic, *MXene Materials for the Electrochemical Nitrogen Reduction-Functionalized or Not?*, ACS Catalysis **10**, 253 (2020).

[200] Y. Kobayashi, M. Kitano, S. Kawamura, T. Yokoyama, and H. Hosono, *Kinetic Evidence: The Rate-Determining Step for Ammonia Synthesis over Electride-Supported Ru Catalysts Is No Longer the Nitrogen Dissociation Step*, Catalysis Science & Technology **7**, 47 (2017).

[201] B. H. R. Suryanto, H. L. Du, D. Wang, J. Chen, A. N. Simonov, and D. R. MacFarlane, *Challenges and Prospects in the Catalysis of Electroreduction of Nitrogen to Ammonia*, Nature Catalysis **2**, 290 (2019).

[202] Y. Wang, A. Xu, Z. Wang, L. Huang, J. Li, F. Li, J. Wicks, M. Luo, D. H. Nam, C. S. Tan, Y. Ding, J. Wu, Y. Lum, C. T. Dinh, D. Sinton, G. Zheng, and E. H. Sargent, *Enhanced Nitrate-to-Ammonia Activity on Copper-Nickel Alloys via Tuning of Intermediate Adsorption*, Journal of the American Chemical Society **142**, 5702 (2020).

[203] J. Li, J. Gao, T. Feng, H. H. Zhang, D. Liu, C. Zhang, S. Huang, C. Wang, F. Du, C. Li, and C. Guo, *Effect of Supporting Matrixes on Performance of Copper Catalysts in Electrochemical Nitrate Reduction to Ammonia*, Journal of Power Sources **511**, 230463 (2021).

[204] H. Zhou, B. Xiong, L. Chen, and J. Shi, *Modulation Strategies of Cu-Based Electrocatalysts for Efficient Nitrogen Reduction*, Journal of Materials Chemistry A **8**, 20286 (2020).

[205] K. Honkala, A. Hellman, I. N. Remediakis, A. Logadottir, A. Carlsson, S. Dahl, C. H. Christensen, and J. K. Nørskov, *Ammonia Synthesis from First-Principles Calculations*, Science **307**, 555 (2005).

[206] H. S. Kim, J. Choi, J. Kong, H. Kim, S. J. Yoo, and H. S. Park, *Regenerative Electrocatalytic Redox Cycle of Copper Sulfide for Sustainable NH_3 Production under Ambient Conditions*, ACS Catalysis **11**, 435 (2021).

[207] J. Kong, M. S. Kim, R. Akbar, H. Y. Park, J. H. Jang, H. Kim, K. Hur, and H. S. Park, *Electrochemical Nitrogen Reduction Kinetics on a Copper Sulfide Catalyst for NH_3 Synthesis at Low Temperature and Atmospheric Pressure*, ACS Applied Materials and Interfaces **13**, 24593 (2021).

[208] D. Er, H. Ye, N. C. Frey, H. Kumar, J. Lou, and V. B. Shenoy, *Prediction of Enhanced Catalytic Activity for Hydrogen Evolution Reaction in Janus Transition Metal Dichalcogenides*, Nano Letters **18**, 3943 (2018).

[209] X. Yang, Y. Wang, X. Tong, N. Yang, X. Yang, Y. Wang, X. Tong, and N. Yang, *Strain Engineering in Electrocatalysts: Fundamentals, Progress, and Perspectives*, Advanced Energy Materials 2102261 (2021).

[210] A. J. Engler, S. Sen, H. L. Sweeney, and D. E. Discher, *Matrix Elasticity Directs Stem Cell Lineage Specification*, Cell **126**, 677 (2006).

[211] H. B. Schiller and R. Fässler, *Mechanosensitivity and Compositional Dynamics of Cell–Matrix Adhesions*, EMBO Reports **14**, 509 (2013).

[212] R. O. Hynes, *The Extracellular Matrix: Not Just Pretty Fibrils*, Science **326**, 1216 (2009).

[213] J. L. Balestrini, S. Chaudhry, V. Sarrazy, A. Koehler, and B. Hinz, *The Mechanical Memory of Lung Myofibroblasts*, Integrative Biology **4**, 410 (2012).

[214] C. X. Li, N. P. Talele, S. Boo, A. Koehler, E. Knee-Walden, J. L. Balestrini, P. Speight, A. Kapus, and B. Hinz, *MicroRNA-21 Preserves the Fibrotic Mechanical Memory of Mesenchymal Stem Cells*, Nature Materials **16**, 379 (2017).

[215] C. Yang, M. W. Tibbitt, L. Basta, and K. S. Anseth, *Mechanical Memory and Dosing Influence Stem Cell Fate*, Nature Materials **13**, 645 (2014).

[216] S. Nasrollahi, C. Walter, A. J. Loza, G. V. Schimizzi, G. D. Longmore, and A. Pathak, *Past Matrix Stiffness Primes Epithelial Cells and Regulates Their Future Collective Migration through a Mechanical Memory*, Biomaterials **146**, 146 (2017).

[217] A. R. Killaars, J. C. Grim, C. J. Walker, E. A. Hushka, T. E. Brown, and K. S. Anseth, *Extended Exposure to Stiff Microenvironments Leads to Persistent*

Chromatin Remodeling in Human Mesenchymal Stem Cells, Advanced Science **6**, 1801483 (2019).

[218] A. W. Watson, A. D. Grant, S. S. Parker, M. W. Harman, M. R. Roman, B. L. Uhlorn, C. Gowan, R. Castro-Portuguez, L. K. Stolze, C. Franck, D. A. Cusanovich, M. Padi, C. E. Romanoski, and G. Mouneimne, *Breast Tumor Stiffness Instructs Bone Metastasis Via Mechanical Memory*, Cell Reports **35**, 109293 (2021).

[219] C. Dunham, N. Havlioglu, A. Chamberlain, S. Lake, and G. Meyer, *Adipose Stem Cells Exhibit Mechanical Memory and Reduce Fibrotic Contracture in a Rat Elbow Injury Model*, The FASEB Journal **34**, 12976 (2020).

[220] C. Uhler and G. V. Shivashankar, *Regulation of Genome Organization and Gene Expression by Nuclear Mechanotransduction*, Nature Reviews Molecular Cell Biology **18**, 717 (2017).

[221] S. Nemec and K. A. Kilian, *Materials Control of the Epigenetics Underlying Cell Plasticity*, Nature Reviews Materials **6**, 69 (2021).

[222] D. A. Hammer and D. A. Lauffenburger, *A Dynamical Model for Receptor-Mediated Cell Adhesion to Surfaces*, Biophysical Journal **52**, 475 (1987).

[223] D. Choquet, D. P. Felsenfeld, and M. P. Sheetz, *Extracellular Matrix Rigidity Causes Strengthening of Integrin- Cytoskeleton Linkages*, Cell **88**, 39 (1997).

[224] M. Chrzanowska-Wodnicka and K. Burridge, *Rho-Stimulated Contractility Drives the Formation of Stress Fibers and Focal Adhesions*, Journal of Cell Biology **133**, 1403 (1996).

[225] E. N. Olson and A. Nordheim, *Linking Actin Dynamics and Gene Transcription to Drive Cellular Motile Functions*, Nature Reviews Molecular Cell Biology **11**, 353 (2010).

[226] B. L. Doss, M. Pan, M. Gupta, G. Grenci, R. M. Mège, C. T. Lim, M. P. Sheetz, R. Voituriez, and B. Ladoux, *Cell Response to Substrate Rigidity Is Regulated by Active and Passive Cytoskeletal Stress*, Proceedings of the National Academy of Sciences of the United States of America **117**, 12817 (2020).

[227] D. E. Discher, P. Janmey, and Y. L. Wang, *Tissue Cells Feel and Respond to the Stiffness of Their Substrate*, Science **310**, 1139 (2005).

[228] S. Dupont, L. Morsut, M. Aragona, E. Enzo, S. Giulitti, M. Cordenonsi, F. Zanconato, J. Le Digabel, M. Forcato, S. Bicciato, N. Elvassore, and S. Piccolo, *Role of YAP/TAZ in Mechanotransduction*, Nature **474**, 179 (2011).

[229] B. v. Fearing, L. Jing, M. N. Barcellona, S. E. Witte, J. M. Buchowski, L. P. Zebala, M. P. Kelly, S. Luhmann, M. C. Gupta, A. Pathak, and L. A. Setton, *Mechanosensitive Transcriptional Coactivators MRTF-A and YAP/TAZ*

Regulate Nucleus Pulposus Cell Phenotype through Cell Shape, The FASEB Journal **33**, 14022 (2019).

[230] E. Makhija, D. S. Jokhun, and G. V. Shivashankar, *Nuclear Deformability and Telomere Dynamics Are Regulated by Cell Geometric Constraints*, Proceedings of the National Academy of Sciences of the United States of America **113**, E32 (2016).

[231] N. Jain, K. V. Iyer, A. Kumar, and G. V Shivashankar, *Cell Geometric Constraints Induce Modular Gene-Expression Patterns via Redistribution of HDAC3 Regulated by Actomyosin Contractility.*, Proceedings of the National Academy of Sciences of the United States of America **110**, 11349 (2013).

[232] S. J. Heo, S. D. Thorpe, T. P. Driscoll, R. L. Duncan, D. A. Lee, and R. L. Mauck, *Biophysical Regulation of Chromatin Architecture Instills a Mechanical Memory in Mesenchymal Stem Cells*, Scientific Reports **5**, 16895 (2015).

[233] J. E. Ferrell, *Bistability, Bifurcations, and Waddington's Epigenetic Landscape*, Current Biology **22**, R458 (2012).

[234] S. Huang, *The Molecular and Mathematical Basis of Waddington's Epigenetic Landscape: A Framework for Post-Darwinian Biology?*, BioEssays **34**, 149 (2012).

[235] T. Peng, L. Liu, A. L. MacLean, C. W. Wong, W. Zhao, and Q. Nie, *A Mathematical Model of Mechanotransduction Reveals How Mechanical Memory Regulates Mesenchymal Stem Cell Fate Decisions*, BMC Systems Biology **11**, 55 (2017).

[236] G. Ascolani, T. M. Skerry, D. Lacroix, E. Dall'ara, and A. Shuaib, *Revealing Hidden Information in Osteoblast's Mechanotransduction through Analysis of Time Patterns of Critical Events*, BMC Bioinformatics **21**, 114 (2020).

[237] S. J. Mousavi and M. Hamdy Doweidar, *Role of Mechanical Cues in Cell Differentiation and Proliferation: A 3D Numerical Model*, PLOS ONE **10**, e0124529 (2015).

[238] Y.-K. Kwon and K.-H. Cho, *Coherent Coupling of Feedback Loops: A Design Principle of Cell Signaling Networks*, Bioinformatics **24**, 1926 (2008).

[239] T. Y. C. Tsai, S. C. Yoon, W. Ma, J. R. Pomerening, C. Tang, and J. E. Ferrell, *Robust, Tunable Biological Oscillations from Interlinked Positive and Negative Feedback Loops*, Science **321**, 126 (2008).

[240] N. Mitarai, M. H. Jensen, and S. Semsey, *Coupled Positive and Negative Feedbacks Produce Diverse Gene Expression Patterns in Colonies*, MBio **6**, (2015).

[241] Y.-K. Kwon and K.-H. Cho, *Quantitative Analysis of Robustness and Fragility in Biological Networks Based on Feedback Dynamics*, Bioinformatics **24**, 987 (2008).

[242] T. Mitra, S. N. Menon, and S. Sinha, *Emergent Memory in Cell Signaling: Persistent Adaptive Dynamics in Cascades Can Arise from the Diversity of Relaxation Time-Scales*, Scientific Reports **8**, 13230 (2018).

[243] A. Shuaib, D. Motan, P. Bhattacharya, A. McNabb, T. M. Skerry, and D. Lacroix, *Heterogeneity in The Mechanical Properties of Integrins Determines Mechanotransduction Dynamics in Bone Osteoblasts*, Scientific Reports **9**, 1 (2019).

[244] G. Halder, S. Dupont, and S. Piccolo, *Transduction of Mechanical and Cytoskeletal Cues by YAP and TAZ*, Nature Reviews Molecular Cell Biology **13**, 591 (2012).

[245] A. Elosegui-Artola, I. Andreu, A. E. M. Beedle, A. Lezamiz, M. Uroz, A. J. Kosmalska, R. Oria, J. Z. Kechagia, P. Rico-Lastres, A. L. Le Roux, C. M. Shanahan, X. Trepat, D. Navajas, S. Garcia-Manyes, and P. Roca-Cusachs, *Force Triggers YAP Nuclear Entry by Regulating Transport across Nuclear Pores*, Cell **171**, 1397 (2017).

[246] J. Zonderland, S. Rezzola, and L. Moroni, *Actomyosin and the MRTF-SRF Pathway Downregulate FGFR1 in Mesenchymal Stromal Cells*, Communications Biology **3**, 1 (2020).

[247] T. Kanno, T. Takahashi, T. Tsujisawa, W. Ariyoshi, and T. Nishihara, *Mechanical Stress-Mediated Runx2 Activation Is Dependent on Ras/ERK1/2 MAPK Signaling in Osteoblasts*, Journal of Cellular Biochemistry **101**, 1266 (2007).

[248] K. V. Iyer, S. Pulford, A. Mogilner, and G. V. Shivashankar, *Mechanical Activation of Cells Induces Chromatin Remodeling Preceding MKL Nuclear Transport*, Biophysical Journal **103**, 1416 (2012).

[249] C. A. Mullen, T. J. Vaughan, K. L. Billiar, and L. M. McNamara, *The Effect of Substrate Stiffness, Thickness, and Cross-Linking Density on Osteogenic Cell Behavior*, Biophysical Journal **108**, 1604 (2015).

[250] G. Nardone, J. Oliver-De La Cruz, J. Vrbsky, C. Martini, J. Pribyl, P. Skládal, M. Pešl, G. Caluori, S. Pagliari, F. Martino, Z. Maceckova, M. Hajduch, A. Sanz-Garcia, N. M. Pugno, G. B. Stokin, and G. Forte, *YAP Regulates Cell Mechanics by Controlling Focal Adhesion Assembly*, Nature Communications **8**, 1 (2017).

[251] O. M. Yu, J. A. Benitez, S. W. Plouffe, D. Ryback, A. Klein, J. Smith, J. Greenbaum, B. Delatte, A. Rao, K. L. Guan, F. B. Furnari, O. M. Chaim, S. Miyamoto, and J. H. Brown, *YAP and MRTF-A, Transcriptional Co-Activators of RhoA-Mediated Gene Expression, Are Critical for Glioblastoma Tumorigenicity*, Oncogene **37**, 5492 (2018).

[252] N. Ege, A. M. Dowbaj, M. Jiang, M. Howell, S. Hooper, C. Foster, R. P. Jenkins, and E. Sahai, *Quantitative Analysis Reveals That Actin and Src-Family Kinases Regulate Nuclear YAP1 and Its Export*, Cell Systems **6**, 692 (2018).

[253] W. Xiong and J. E. Ferrell, *A Positive-Feedback-Based Bistable "memory Module" That Governs a Cell Fate Decision*, Nature **426**, 460 (2003).

[254] A. Y. Mitrophanov and E. A. Groisman, *Positive Feedback in Cellular Control Systems*, BioEssays **30**, 542 (2008).

[255] L. Wang, B. L. Walker, S. Iannaccone, D. Bhatt, P. J. Kennedy, and W. T. Tse, *Bistable Switches Control Memory and Plasticity in Cellular Differentiation*, Proceedings of the National Academy of Sciences of the United States of America **106**, 6638 (2009).

[256] D. W. Young, M. Q. Hassan, X. Q. Yang, M. Galindo, A. Javed, S. K. Zaidi, P. Furcinitti, D. Lapointe, M. Montecino, J. B. Lian, J. L. Stein, A. J. Van

Wijnen, and G. S. Stein, *Mitotic Retention of Gene Expression Patterns by the Cell Fate-Determining Transcription Factor Runx2*, Proceedings of the National Academy of Sciences of the United States of America **104**, 3189 (2007).

[257] T. M. Schroeder, E. D. Jensen, and J. J. Westendorf, *Runx2: A Master Organizer of Gene Transcription in Developing and Maturing Osteoblasts*, Birth Defects Research Part C - Embryo Today: Reviews **75**, 213 (2005).

[258] F. Calvo, N. Ege, A. Grande-Garcia, S. Hooper, R. P. Jenkins, S. I. Chaudhry, K. Harrington, P. Williamson, E. Moeendarbary, G. Charras, and E. Sahai, *Mechanotransduction and YAP-Dependent Matrix Remodelling Is Required for the Generation and Maintenance of Cancer-Associated Fibroblasts*, Nature Cell Biology **15**, 637 (2013).

[259] C. D. Kegelman, J. M. Collins, M. P. Nijsure, E. A. Eastburn, and J. D. Boerckel, *Gone Caving: Roles of the Transcriptional Regulators YAP and TAZ in Skeletal Development*, Current Osteoporosis Reports **18**, 526 (2020).

[260] S. J. Heo, W. M. Han, S. E. Szczesny, B. D. Cosgrove, D. M. Elliott, D. A. Lee, R. L. Duncan, and R. L. Mauck, *Mechanically Induced Chromatin Condensation Requires Cellular Contractility in Mesenchymal Stem Cells*, Biophysical Journal **111**, 864 (2016).

[261] C. J. Walker, C. Crocini, D. Ramirez, A. R. Killaars, J. C. Grim, B. A. Aguado, K. Clark, M. A. Allen, R. D. Dowell, L. A. Leinwand, and K. S. Anseth, *Nuclear Mechanosensing Drives Chromatin Remodelling in Persistently Activated Fibroblasts*, Nature Biomedical Engineering 1 (2021).

[262] T. Bouzid, E. Kim, B. D. Riehl, A. M. Esfahani, J. Rosenbohm, R. Yang, B. Duan, and J. Y. Lim, *The LINC Complex, Mechanotransduction, and Mesenchymal Stem Cell Function and Fate*, Journal of Biological Engineering **13**, 68 (2019).

[263] J. Swift, I. L. Ivanovska, A. Buxboim, T. Harada, P. C. D. P. Dingal, J. Pinter, J. D. Pajerowski, K. R. Spinler, J. W. Shin, M. Tewari, F. Rehfeldt, D. W. Speicher, and D. E. Discher, *Nuclear Lamin-A Scales with Tissue Stiffness and Enhances Matrix-Directed Differentiation*, Science **341**, (2013).

[264] C. T. Foster, F. Gualdrini, and R. Treisman, *Mutual Dependence of the MRTF-SRF and YAP-TEAD Pathways in Cancer-Associated Fibroblasts Is Indirect and Mediated by Cytoskeletal Dynamics*, Genes and Development **31**, 2361 (2017).

[265] T. Kim, D. Hwang, D. Lee, J. Kim, S. Kim, and D. Lim, *MRTF Potentiates TEAD - YAP Transcriptional Activity Causing Metastasis*, The EMBO Journal **36**, 520 (2017).

214

[266] G. Meng, J. Wei, Y. Wang, D. Qu, and J. Zhang, *MicroRNA-21 Upregulates YAP by Inhibiting Transcription Factor RUNX1 to Regulate Immunosuppressive Ability of Myeloid-Derived Suppressor Cells in Lung Cancer*, Cancer Cell International **20**, 1 (2020).

[267] Y. Qiao, J. Chen, Y. B. Lim, M. L. Finch-Edmondson, V. P. Seshachalam, L. Qin, T. Jiang, B. C. Low, H. Singh, C. T. Lim, and M. Sudol, *YAP Regulates Actin Dynamics through ARHGAP29 and Promotes Metastasis*, Cell Reports **19**, 1495 (2017).

[268] G. Shi, L. Liu, C. Hyeon, and D. Thirumalai, *Interphase Human Chromosome Exhibits out of Equilibrium Glassy Dynamics*, Nature Communications **9**, 1 (2018).

[269] L. Sardo, A. Lin, S. Khakhina, L. Beckman, L. Ricon, W. Elbezanti, T. Jaison, H. Vishwasrao, H. Shroff, C. Janetopoulos, and Z. A. Klase, *Real-Time Visualization of Chromatin Modification in Isolated Nuclei*, Journal of Cell Science **130**, 2926 (2017).

[270] M. P. Gantier, C. E. McCoy, I. Rusinova, D. Saulep, D. Wang, D. Xu, A. T. Irving, M. A. Behlke, P. J. Hertzog, F. MacKay, and B. R. G. Williams, *Analysis of MicroRNA Turnover in Mammalian Cells Following Dicer1 Ablation*, Nucleic Acids Research **39**, 5692 (2011).

215

[271] A. R. Killaars, C. J. Walker, and K. S. Anseth, *Nuclear Mechanosensing Controls MSC Osteogenic Potential through HDAC Epigenetic Remodeling*, Proceedings of the National Academy of Sciences of the United States of America **117**, 21258 (2020).

[272] M. Rabineau, F. Flick, C. Ehlinger, E. Mathieu, I. Duluc, M. Jung, B. Senger, L. Kocgozlu, P. Schaaf, P. Lavalle, J. N. Freund, Y. Haikel, and D. Vautier, *Chromatin De-Condensation by Switching Substrate Elasticity*, Scientific Reports **8**, 12655 (2018).

[273] G. Shi, L. Liu, C. Hyeon, and D. Thirumalai, *Interphase Human Chromosome Exhibits out of Equilibrium Glassy Dynamics*, Nature Communications **9**, 1 (2018).

[274] F. Passaro, I. De Martino, F. Zambelli, G. Di Benedetto, M. Barbato, A. M. D'Erchia, C. Manzari, G. Pesole, M. Mutarelli, D. Cacchiarelli, D. Antonini, S. Parisi, and T. Russo, *YAP Contributes to DNA Methylation Remodeling upon Mouse Embryonic Stem Cell Differentiation*, Journal of Biological Chemistry **296**, 100138 (2021).

[275] C. C. Price, J. Mathur, J. D. Boerckel, A. Pathak, and V. B. Shenoy, *Dynamic Self-Reinforcement of Gene Expression Determines Acquisition of Cellular Mechanical Memory*, Biophysical Journal **120**, 5074 (2021).

[276] R. K. Das, V. Gocheva, R. Hammink, O. F. Zouani, and A. E. Rowan, *Stress-Stiffening-Mediated Stem-Cell Commitment Switch in Soft Responsive Hydrogels*, Nature Materials **15**, 318 (2016).

[277] Y. Cui, F. M. Hameed, B. Yang, K. Lee, C. Q. Pan, S. Park, and M. Sheetz, *Cyclic Stretching of Soft Substrates Induces Spreading and Growth*, Nature Communications **6**, 1 (2015).

[278] S. J. Heo, S. D. Thorpe, T. P. Driscoll, R. L. Duncan, D. A. Lee, and R. L. Mauck, *Biophysical Regulation of Chromatin Architecture Instills a Mechanical Memory in Mesenchymal Stem Cells*, Scientific Reports **5**, 16895 (2015).

[279] K. Takahashi and S. Yamanaka, *Induction of Pluripotent Stem Cells from Mouse Embryonic and Adult Fibroblast Cultures by Defined Factors*, Cell **126**, 663 (2006).

[280] C. Yang, F. W. DelRio, H. Ma, A. R. Killaars, L. P. Basta, K. A. Kyburz, and K. S. Anseth, *Spatially Patterned Matrix Elasticity Directs Stem Cell Fate*, Proceedings of the National Academy of Sciences of the United States of America **113**, E4439 (2016).

[281] A. R. Killaars, C. J. Walker, and K. S. Anseth, *Nuclear Mechanosensing Controls MSC Osteogenic Potential through HDAC Epigenetic Remodeling*,

217

Proceedings of the National Academy of Sciences of the United States of America **117**, 21258 (2020).

[282] A. Jain, S. P. Ong, G. Hautier, W. Chen, W. D. Richards, S. Dacek, S. Cholia, D. Gunter, D. Skinner, G. Ceder, and K. A. Persson, *Commentary: The Materials Project: A Materials Genome Approach to Accelerating Materials Innovation*, APL Materials **1**, 011002 (2013).

[283] B. Blaiszik, K. Chard, J. Pruyne, R. Ananthakrishnan, S. Tuecke, and I. Foster, *The Materials Data Facility: Data Services to Advance Materials Science Research*, JOM **68**, 2045 (2016).

[284] Z. Guo, C. Price, V. B. Shenoy, and J. Lowengrub, *Modeling the Vertical Growth of van Der Waals Stacked 2D Materials Using the Diffuse Domain Method*, Modelling and Simulation in Materials Science and Engineering **28**, 025002 (2020).

[285] H. Ye, J. Zhou, D. Er, C. C. Price, Z. Yu, Y. Liu, J. Lowengrub, J. Lou, Z. Liu, and V. B. Shenoy, *Toward a Mechanistic Understanding of Vertical Growth of van Der Waals Stacked 2D Materials: A Multiscale Model and Experiments*, ACS Nano **11**, 12780 (2017).

[286] S. v. Mandyam, M.-Q. Zhao, P. Masih Das, Q. Zhang, C. C. Price, Z. Gao, V. B. Shenoy, M. Drndić, and A. T. C. Johnson, *Controlled Growth of Large-*

Area Bilayer Tungsten Diselenides with Lateral P–N Junctions, ACS Nano **13**, 10490 (2019).

[287] P. Kumar, J. P. Horwath, A. C. Foucher, C. C. Price, N. Acero, V. B. Shenoy, E. A. Stach, and D. Jariwala, *Direct Visualization of Out-of-Equilibrium Structural Transformations in Atomically Thin Chalcogenides*, Npj 2D Materials and Applications **4**, 1 (2020).

[288] H. Huang, X.-Q. Fu, and R.-S. Han, *Klein Paradox of Two-Dimensional Dirac Electrons in Circular Well Potential*, Communications in Theoretical Physics **58**, 205 (2012).

[289] E. F. Bertaut, *Electric Field and Energy in Dipole Lattices*, Physical Review **91**, 415 (1953).

[290] S. Ismail-Beigi, *2D Periodic Charge Sheets: Electrostatics*, https://volga.eng.yale.edu/sites/default/files/files/2dsheets-electrostatics.pdf.

[291] B. D. Cosgrove, C. Loebel, T. P. Driscoll, T. K. Tsinman, E. N. Dai, S. J. Heo, N. A. Dyment, J. A. Burdick, and R. L. Mauck, *Nuclear Envelope Wrinkling Predicts Mesenchymal Progenitor Cell Mechano-Response in 2D and 3D Microenvironments*, Biomaterials **270**, 120662 (2021).

[292] F. Jacob and J. Monod, *Genetic Regulatory Mechanisms in the Synthesis of Proteins*, Journal of Molecular Biology **3**, 318 (1961).

[293] T. Maniatis and R. Reed, *An Extensive Network of Coupling among Gene Expression Machines*, Nature **416**, 499 (2002).

[294] F. Lin, I. M. Markus, D. Nordlund, T.-C. Weng, M. D. Asta, H. L. Xin, and M. M. Doeff, *Surface Reconstruction and Chemical Evolution of Stoichiometric Layered Cathode Materials for Lithium-Ion Batteries*, Nature Communications **5**, 3529 (2014).

[295] B. Anasori, M. R. Lukatskaya, and Y. Gogotsi, *2D Metal Carbides and Nitrides (MXenes) for Energy Storage*, Nature Reviews Materials **2**, 16098 (2017).